ELECTROMECHANICAL IMPEDANCE-BASED DAMAGE DETECTION AND LOCALIZATION EMPLOYING DATA FUSION TECHNIQUES

Shishir Kumar Singh, M. Tech. Eng

Supervisor: Paweł H. Malinowaski
D.Sc. Ph.D.

Auxiliary supervisor: Rohan Soman, Ph.D. Eng

A dissertation submitted to the Scientific Board of the Szewalski Institute of Fluid-Flow Machinery, Polish Academy of Sciences in partial fulfillment of the requirements for the Degree of Doctor of Philosophy

May 2023

I would like to dedicate this thesis to my loving parents ...

Declaration

I hereby declare that except where specific reference is made to the work of others, the contents of this dissertation are original and have not been submitted in whole or in part for consideration for any other degree or qualification at Institute of Fluid Flow Machinery, Polish Academy of Sciences, or any other university.

This dissertation is my own work and contains nothing which is the outcome of work done in collaboration with others, except as specified in the text and Acknowledgements.

Shishir Kumar Singh, M. Tech. Eng
May 2023

Acknowledgements

The completion of this thesis is attributed to the support and encouragement of many people. First and foremost, I would like to extend my sincere thanks and gratitude towards my supervisor, Professor Malinowski for his continuous guidance, encouragement and strong support during my research work. It has been an honour to be associated with Pawel whose suggestions and critical views have greatly helped me in this work. His conscientious academic spirit and modest, open-minded personality inspire me both in academic study and my professional growth as well. In addition, I need to extend my heartfelt appreciation to my colleague, Dr. Rohan Soman, whose patient guidance, valuable suggestions and constant encouragement allowed me to successfully complete this thesis.

Additionally, I would like to express my sincere gratitude to all the colleagues at Institute of Fluid Flow Machinery, Polish Academy of Sciences who have helped me. I also acknowledge the funding support provided by the National Science Center, Poland under grant no 2016/22/E/ST8/00068 and 2019/35/B/ST8/00691. I am also grateful to TASK-CI for allowing the use of their computational resources.

Last but not least, I would like to express my special thanks to my wife and my parents, whose care and support motivate me to move on and make me a better person.

Abstract

There is much active research in the area of structural health monitoring (SHM) of lightweight structures to detect small levels of damage. The SHM system should be ideally low-cost, suitable for continuous monitoring, and able to detect minute damage in varying ambient conditions. The ability of the electromechanical impedance method (EMI) to detect damage in potentially dangerous situations has been demonstrated. Additionally, it is inexpensive due to the use of a bonded lightweight piezoelectric transducer (PZT). Furthermore, due to their high operational frequency, they are immune to ambient noise. The EMI technique is employed for damage detection and classification in lightweight structures due to its sensitivity to the low scale of damage. However, creating a data processing method that is sensitive to even superficial damage is a challenging task.

This thesis focuses on enhancing the performance of damage assessment for metal and composite structures to sophisticated 3D printed structures for a variety of damage instances utilizing various data fusion techniques. Firstly, the data-fusion based series and parallel combinations of sensors were studied and compared in the damaged steel beam structure with a variation of the environment temperature. The parallel connection has shown an advantage over individual and series piezo connections in varying temperature environment conditions while reducing the damage detection measurement time. Secondly, the thesis presented a novel fused parameter (F) focusing on damage quantification and classification in metal or composite structures based on the sensor's resistance (R) and conductance (G) data in a chosen frequency band. The new signature under different damage conditions is then quantified using established indices such as the root mean square deviation index (RMSD), mean absolute percentage deviation, etc. Further, an integrated approach of a common healthy baseline is used for damage detection and classification in the EMI technique. The principal component analysis (PCA) is carried out for sensor network data and the corresponding damage index is calculated to study the information of piezoelectric transducer's impedance (|Z|), admittance (|Y|), R, and G data in the frequency domain. A new optimized data fusion approach is proposed which was realized at the sensor level using the PCA as well as at the variable level using self-organizing maps (SOMs). In the process, a centralized data-fused baseline eigenvector is prepared from a healthy structure, and the damage responses are

projected on this baseline model. The statistical, data-driven damage matrices are calculated and compared with the RMSD index and used in a fusion-based data classification using SOM. The SOM comparative studies are performed using the Q-statistics (Q index) and Hotelling's T^2 statistic (T^2 index). The proposed methodology is tested and validated for an aluminum plate with multiple drilled holes of varying sizes and locations. The method demonstrates a significant increase in damage sensitivity for hole location and hole size regardless of the frequency range used. Thirdly, this thesis implements localization using a modified probability weight function.

The comparative damage imaging method is applied to the composite plate with impact damage for G and R based fused signature, direct-coupled mechanical impedance (DCMI) signature, and normalized G signature. The approach is further extended to detect multi-damages simultaneously using the network of sensors and used for damage localization in the acrylonitrile butadiene styrene (ABS) plate. The results show that indeed the proposed algorithm works and improves the damage localization using the EMI technique. Further, a database of the damage indices for numerous damage situations is created using this analytical methodology. Based on several fits, an analytical model is created for the inverse technique's association of distance and angle with the damage index (linear and exponential). The damage scenario with the lowest mean error in the damage indices is determined by comparing the measured damage indices from the structure with this database. But the daunting task in the EMI method is the selection of robust frequency ranges. Finally, in order to solve this issue, an innovative standard deviation approach is used for the selection of effective frequency ranges. The novel nature of frequency range selection is based on the difference between healthy and damaged state data. Further, a data fusion technique is introduced for damage detection and classification using analytical and experimental data in this effective frequency range. A combined C-index based statistical data-driven damage matrices are calculated in this frequency for four samples made of metal and composite with different damage scenarios to demonstrate the applicability of the method. The method looks suitable for identifying the damage location and damage severity simultaneously and is more effective for the less severe damage cases.

Publications

Journals

1. Soman, R., **Singh, S. K.**, and Malinowski, P. (2023). Damage localization using electromechanical impedance technique based on inverse implementation. Structural Health Monitoring, 0(0).

2. **Singh, S. K.**, and Malinowski, P. H. (2022). An innovative data-driven probabilistic approach for damage detection in Electromechanical Impedance Technique. Composite Structures, 295, 115808.

3. Sikdar, S., **Singh, S. K.**, Malinowski, P., and Ostachowicz, W. (2022). Electromechanical impedance based debond localisation in a composite sandwich structure. Journal of Intelligent Material Systems and Structures, 33(12), 1487-1496.

4. **Singh, S. K.**, Sikdar, S., and Malinowski, P. H. (2021). An optimized data fusion strategy for structural damage assessment using electromechanical impedance. Smart Materials and Structures, 30(3), 035012.

5. Malinowski, P. H., Wandowski, T., and **Singh, S. K.** (2021). Employing principal component analysis for assessment of damage in GFRP composites using electromechanical impedance. Composite Structures, 266, 113820.

6. Soman, R., **Singh, S. K.**, Wandowski, T., and Malinowski, P. (2020). Development of robust metric based on cumulative electrical power for electromechanical impedance based structural health monitoring. Smart Materials and Structures, 29(11), 115047.

7. **Singh, S. K.**, Soman, R., Wandowski, T., and Malinowski, P. (2020). A variable data fusion approach for electromechanical impedance-based damage detection. Sensors, 20(15), 4204.

8. Soman, R., Kudela, P., Balasubramaniam, K., **Singh, S. K.**, and Malinowski, P. (2019). A Study of Sensor Placement Optimization Problem for Guided Wave-Based Damage Detection. Sensors, 19(8), 1856.

Conferences

1. **Singh, S. K.**, Fakih, M. A., and Malinowski, P. (2023). A Sensitivity Study of Different Actuators for the Electromechanical Impedance Method in 3D-Printed Material. In European Workshop on Structural Health Monitoring (pp. 874-882). Springer, Cham.

2. Fakih, M. A., **Singh, S. K.**, Mustapha, S., and Malinowski, P. (2023). Damage Localization in 3D-Printed Plates with Different Infill Densities. In 49th Annual Review of Progress in Quantitative Nondestructive Evaluation (Vol. 86595, p. V001T04A001). American Society of Mechanical Engineers.

3. Fakih, M. A., **Singh, S. K.**, Mustapha, S., and Malinowski, P. (2023). The Effect of the Infill Density in 3D-Printed PLA on Lamb Waves' Propagation Characteristics and their Sensitivity to the Presence of Damage. 10.1007/978-3-031-07322-9-20.

4. **Singh, S. K.**, Fakih, M. A, Andrearczyk, A, Ijjeh, A, and Malinowski, P. H. (2023), A machine-learning-based health diagnosis of polymer 3D-printed plates using the electromechanical impedance method, In Health Monitoring of Structural and Biological Systems XVII, vol. 12488, pp. 178-185. SPIE.

5. **Singh, S. K.**, Soman, R., and Malinowski, P. (2022). Sensor network based damage detection of structures using weight function in electromechanical impedance method. In Health Monitoring of Structural and Biological Systems XVI (Vol. 12048, pp. 341-351). SPIE.

6. Fakih, M. A., **Singh, S. K.**, and Malinowski, P. (2022). Lamb-wave propagation characteristics and damage imaging in additively manufactured plates. In Health Monitoring of Structural and Biological Systems XVI (Vol. 12048, pp. 213-221). SPIE.

7. **Singh, S. K.**, Ostachowicz, W. M., and Malinowski, P. H. (2021). Damage Study Using Series and Parallel Electrode in Electromechanical Impedance Method. In European Workshop on Structural Health Monitoring (pp. 808-816). Springer, Cham.

8. **Singh, S. K.**, and Malinowski, P. H. (2021). Damage study of structures using Hotteling's T^2 curve in electromechanical impedance method. In Nondestructive Characterization and Monitoring of Advanced Materials, Aerospace, Civil Infrastructure, and Transportation XV (Vol. 11592, pp. 234-241). SPIE.

9. **Singh, S. K.**, Wandowski, T., and Malinowski, P. H. (2019). An innovative decentralised data fusion using electromechanical impedance techniques. In Health Monitoring of Structural and Biological Systems XIII (Vol. 10972, pp. 45-52). SPIE.

10. **Singh, S. K.**, and Malinowski, P. H. (2018). Quantification of damage sensitivity by electromechanical impedance signatures. In Proc. of the 7th Asia APWSHM Conference, Hong Kong, China.

11. Balasubramaniam, K., **Singh, S. K.**, Soman, R., and Malinowski, P. H. (2018). A study of electromechanical impedance and guided wave techniques for the sensitivity of sensors network in damage detection. In Proc. of the 7th APWSHM Conference, Hong Kong, China (pp. 12-15).

Table of contents

Appendix Publications **vii**

List of figures **xii**

List of tables **xviii**

1 Introduction **1**
1.1 Motivation 1
1.2 Literature review of EMI 3
1.2.1 Piezoelectricity and Piezoelectric Materials in SHM 4
1.2.2 EMI principle 5
1.2.3 Physics based SHM using EMI 9
1.2.4 Data driven SHM using EMI 12
1.3 Research Gap and Objectives 16
1.4 Organisation of dissertation 18

2 Damage detection via data fusion of PZTs based on series and parallel connections **19**
2.1 Need and scope of the combined sensor study 19
2.2 Theory and experimental setup for the investigation 21
2.3 Comparative study of parallel combination with other mode of combinations 23
2.4 Robust damage detection in the varied environment temperature condition . 27
2.4.1 Case I 28
2.4.2 Case II 29

3 Variable and sensor level data fusion based damage detection **33**
3.1 Scope of study 33
3.2 Variables based data fusion 33
3.2.1 Experimental investigation of fused F 34

3.2.2 Theoretical implementation of the fused data F 35
3.2.3 Comparative study of spectra using damage indices 37
3.2.4 Summary 40
3.3 Multi-level data fusion approach in damage detection 44
3.3.1 Introduction 44
3.3.2 Data driven methodology based on PCA and SOM 45
3.3.3 Results and implementation of the damage detection 49

4 Sensor network based damage imaging 60
4.1 Background 60
4.2 Damage imaging approach 61
4.2.1 Comparative study of sensing radius using different types of EMI signals 61
4.2.2 Multi-damage localization using sensor network 68
4.3 Damage localization based on inverse model 75

5 A standard deviation approach in damage detection 79
5.1 Introduction 79
5.2 Novel frequency range selection methodology 80
5.2.1 Need of effective frequency range selection 80
5.2.2 Methodology of effective frequency range selection 81
5.3 Fusion-based probabilistic methodology 84
5.3.1 C-index sensitivity study using analytical spectra 89
5.3.2 C-index sensitivity study for metal and composites 90

6 Conclusions and Future work 106
6.1 Research conclusions 106
6.2 Major Contributions 110
6.3 Future work recommendation 111

References 112

List of figures

1.1 Different type of the structures with possible incipient and minor structural damage a) aeroplane, b) wind turbine, and c) crack in bridge. 3
1.2 Schematic diagram of the EMI based SHM. 4
1.3 Piezoelectric material response under different application. 5
1.4 Schematic measurement of mechanical impedance of structure using EMI method. 6
1.5 Impedance plot of 10 mm diameter PZT of various thickness using EMI method. 6
1.6 Impedance plot of 0.5 mm thick PZT of various diameter (D) using EMI method. 7
1.7 Impedance of various structural response of PZT using EMI method. 8

2.1 Coupled diagram of n PZTs impedance. 21
2.2 Diagram of sensor connection using breadboard for the damage detection in the steel beam. 23
2.3 Diagram of p1 and p2 with different damage conditions in the steel beam structure. 23
2.4 Diagram of sensor connection using breadboard for the damage detection in the steel beam. 24
2.5 The R spectrum plot of the p1, p2, p12p and p12s combinations in the healthy state. 24
2.6 The healthy and the damage R spectrum plot of the p1, p2, p12p, p12s combination for Fig. 2.3a damage arrangement. 25
2.7 The RMSD damage indices quantification of the R variable in different combinations of connection for raw and detrended filtered spectra in the damage case of Fig 2.3a. 25

2.8 The RMSD damage indices quantification of the R variable in different combinations of connection for raw and detrended filtered spectra in the damage case of Fig 2.3b. 26
2.9 The quantification of the R variable using the RMSD damage indices of various connections for the raw and detrended filtered spectra for damage case shown in Fig. 2.3c. 27
2.10 The RMSD damage indices quantification of the R variable in different combinations of connection for raw spectra in the case of Fig 2.3c. 29
2.11 The RMSD damage index quantification of the of p1 using R variable of beam. 30
2.12 The RMSD damage index quantification of the of p2 using R variable of beam. 31
2.13 The RMSD damage index quantification of the of p12p using R variable of beam. 31
2.14 The RMSD damage index quantification of the of p12s using R variable of beam. 32

3.1 Composite beam with enlarged view showing delaminated region (S3). . . . 35
3.2 The GFRP plate with impact locations. 36
3.3 Detrended spectrum of variables G, R and fused F. 38
3.4 The RMSD index of the variables G, R and F for GFRP beam. 39
3.5 The GFRP beam's MAPD damage index for the variables G, R, and F. . . . 40
3.6 The GFRP beam's RMSDk damage index for the variables G, R, and F. . . 41
3.7 The RMSD damage index for the GFRP plate's variables G, R, and F. . . . 42
3.8 The MAPD damage index for the GFRP plate's variables G, R, and F. . . . 42
3.9 The RMSDk index for the GFRP plate's variables G, R, and F. 43
3.10 Sensor network distribution against the damage locations in the sample plate. 45
3.11 a framework for the methodology used to classify damage. 46
3.12 A framework of the two dimensional rectangular topology based SOM in classification. 48
3.13 Sensor network G spectra for piezo-actuator (a) P1, (b) P4, (c) P5, and (d) P8 in both the healthy and damaged states. 49
3.14 Sensor network RMSD damage indices of 5 mm, 8mm and 10 mm hole drilled at 'D-a' location for the |Z|, |Y|, R and G in the wider frequency range 17-600 kHz. 50
3.15 Sensor network RMSD damage indices of 5 mm, 8mm and 10 mm hole drilled at 'D-a' location for the |Z|, |Y|, R and G in the narrow frequency range 180-250 kHz. 51

3.16 The PC1 based reconstructed conductance spectrum plot for the sensors (a) P1, (b) P4, (c) P5 and (d) P8. 51
3.17 RMSD damage index for the variables |Z|, |Y|, R, and G in the wide frequency range of 17-600 kHz for the drill holes of 5 mm, 8 mm, and 10 mm based on the first PC. 52
3.18 RMSD based on 1st PC for the variables |Z|, |Y|, R, and G in the specific frequency range of 180-250 kHz for drill holes of 5 mm, 8 mm, and 10 mm. 53
3.19 Variance contribution of the sensor network for the 17-600 kHz large aluminum plate EMI variables |Z|, |Y|, R, and G. 53
3.20 An evaluation of traditional RMSD fused RMSD based on PCA utilizing PC1, PC1 and PC2 (a) 5 mm hole, (b) 8 mm hole, (c) 10 mm hole, and (d) Fused PC1 and PC2 RMSD for 5 mm, 8 mm, and 10 mm hole for P1. . . . 54
3.21 Sensor network 1^{st} PC RMSD damage index for the 'D-b' location for the variables (a) |Z|, (b) |Y|, (c) R and (d) G. 55
3.22 Q index calculation of P1 EMI variables (a) |Z|, (b) |Y|, (c) R and (d) G on a large sample plate. 55
3.23 T^2 index calculation P1 EMI variables (a) |Z|, (b) |Y|, (c) R and (d) G on the sample plate. 56
3.24 Matching hits based healthy (H) and damage data (D-a) classification for the Q index of piezo-actuator P1 in aluminum plate using (a) |Z| and R (b) |Y| and G. 57
3.25 Matching hits based healthy (H) and damage (D-a) data classification using T^2 index of piezo-actuator P1 in aluminum plate using (a) |Z| and R (b) |Y| and G. 57
3.26 Matching hits based 'D-a' damage severity (5 mm, 8 mm and 10 mm hole) data classification for the Q index of P1 in aluminum plate using (a) |Z| and R (b) |Y| and G. 58
3.27 Matching hits based damage 'D-a' damage severity (5 mm, 8 mm and 10 mm hole) data classification for the T^2 index of piezo-actuator P1 in aluminum plate using (a) |Z| and R (b) |Y| and G. 58
3.28 Matching hits based healthy and damage locations data classification for the Q index of piezo-actuator P5 in aluminum plate using (a) |Z| and R (b) |Y| and G. 59
3.29 T^2 indices based matching hits classification of healthy-H, damaged state-'D-a' and 'D-b' of the structure for the P5 in aluminum plate using (a) |Z| and R (b) |Y| and G. 59

4.1 Composite plate with bonded sensor network and with the impact damage. . 62
4.2 The comparative plot for the raw G signature in 2x2 PZT array. 63
4.3 The plot between radius of sensing region (r) and DLA for normalized data a) r=1 mm, b) r=5mm and c) r=20mm. 64
4.4 The plot between radius (r) and DLA for a) DCMI and b) fused F at 20 mm interval. 65
4.5 A comparative RMSD plot for DCMI real and imaginary data, ND data and fused F data. 66
4.6 Illustration of impact damage on the composite structure using real part for the DCMI signatures. 66
4.7 Illustration of impact damage on the composite structure using fused F signatures. 67
4.8 Illustration of impact damage on the composite structure using the ND signatures. 68
4.9 Diagram of sensor network and multiple damage to an ABS plate. 69
4.10 Multi-damage detection flowchart. 70
4.11 DI of sensor network for single damage detection. 71
4.12 Single damage detection using a) triangular coverage and b) damage imaging. 72
4.13 DI of sensor network for two damage detection using normalized RMSD. . 72
4.14 Two damage detection using a) triangular coverage and b) damage imaging. 73
4.15 DI of sensor network for three damage detection using normalized RMSD. . 73
4.16 Three damage detection using a) triangular coverage and b) damage imaging. 74
4.17 Distance based DI in the composite structure. 77
4.18 Angle based DI in the composite structure. 77
4.19 Damage localization based on the inverse mode. 78

5.1 Diagram of a small aluminum sample that was used to choose an appropriate frequency range and detect damage. 82
5.2 Sensitivity model parameters using σ_A values based on the G in the aluminum plate's frequency sub ranges. 83
5.3 Sensitivity model parameters using σ_A values contingent on the R in the frequency sub ranges of the aluminum plate. 84
5.4 Diagram of composite samples used to test frequency range selection approach for damage detection. 85
5.5 Sensitivity plot of the G data in the frequency sub ranges of the GFRP plate using σ_A values. 86

5.6 Sensitivity plot of the R in the frequency sub ranges of the GFRP plate using σ_A values. 86
5.7 An illustration of the damage detection procedure using the samples' C-index. 88
5.8 Analytical signal spectra at the following points: a) baseline, b) amplitude increases, c) with the addition of perturbation, d) with peak intensity, e) new perturbation and f) increase in the amplitude of new peak. 89
5.9 Calculation of the C-index for the analytical spectra. 90
5.10 C-index for the healthy and damaged aluminum plate in the frequency sub-bands: a) 9^{th} , b) 12^{th} , c) 19^{th}, and d) 23^{rd} respectively. 91
5.11 RMSD index for the healthy and damaged aluminum plate in the following frequency sub-bands: a) 9^{th} , b) 12^{th} , c) 19^{th}, and d) 23^{rd} respectively. . . . 92
5.12 C-index of the GFRP plate's structures in the effective 9^{th} frequency sub band. 92
5.13 RMSD index in effective 9^{th} frequency sub band of the GFRP plate. 93
5.14 The sensor P1's G spectrum plot for holes measuring 5 and 10 millimeters. 94
5.15 a) G and b) R sensor network RMSD damage indices for 5 mm and 10 mm holes drilled in a large aluminum plate. 95
5.16 The pdf curve of healthy state's a) v_{gh}, and b) v_{rh} variables. 95
5.17 The pdf curve of a) v_{gd}, and b) v_{rd} variables for the 5mm damage state. . . . 96
5.18 The pdf curve of a) v_{gd}, and b) v_{rd} variables for the 10 mm damage state. . . 96
5.19 C-index of piezo P1 for the damage of 5 mm and 10 mm drilled holes in the large aluminum plate. 97
5.20 GFRP plate with impact damage shown in diagram. 98
5.21 The sensor P1, P2, P3, and P4's G spectrum displayed on a GFRP plate. . . 99
5.22 The sensor network's C-index following the impact at composite plate point "g". 99
5.23 Variables a) v_{gd} and b) v_{rd} pdf distribution diagram for P1 following the impact of damage "g". 100
5.24 Variables a) v_{gd} and b) v_{rd} pdf distribution diagram for P2 following the impact of damage "g". 100
5.25 Variables a) v_{gd} and b) v_{rd} pdf distribution diagram for P3 following the impact of damage "g". 101
5.26 Variables a) v_{gd} and b) v_{rd} pdf distribution diagram for P4 following the impact of damage "g". 101
5.27 The G spectrum plot of the sensor P2 after each impact on the GFRP plate. 103
5.28 Sensor P2, C-index contribution after each damage impact on the composite plate. 103

5.29 The pdf distribution of the a) v_{gh} and b) v_{rh} variables for the P2 repeated measurements in a healthy state. 104
5.30 The pdf distribution of the a) v_{gd} and b) v_{rd} variables for P2 following the impact of damage "h". 104
5.31 The pdf distribution of the a) v_{gd} and b) v_{rd} for P2 following the impact of damage "k". 105

List of tables

2.1 Healthy and damage symbols with their explanations. 28
2.2 Created crack damage symbols with their explanations. 30

3.1 Description of impact damage to the GFRP plate surface. 35
3.2 Comparative performance study of G, R and F variable for GFRP beam and GFRP plate. 41

5.1 Summary of P1 healthy and damaged state statistically. 97
5.2 Standard deviation and width data for the sensor network after impact at location 'g'. 102
5.3 Standard deviation and width data for P2 after impact at 'g','h','k' damaged cases. 102

Chapter 1

Introduction

1.1 Motivation

Civil, aerospace, and mechanical engineering structures need inspection for the assessment of their integrity for life safety and cost effectiveness. Many organizations and independent research groups have developed new approaches for full-scale performance assessment and cognitive interpretation of structures, known as structural health monitoring (SHM), to meet the practical needs for the safety condition management of infrastructure. Basically, SHM denotes the process of acquisition, validation and interpretation of a set of data, collected from the structure at different times to facilitate lifespan risk-management decisions [1]. SHM allows shifting the organization of structural health management from periodically scheduled, time-based maintenance to condition-based maintenance that reduces the cost of maintenance and service downtime. By averting unexpected catastrophic system failures like the fuselage separation that occurred on Aloha Airlines in 1988 [2, 3]. SHM procedures have a tremendous potential to increase life safety by avoiding the sudden tragic collapse of the National Bridge I-35W over the Mississippi River in Minneapolis at the time a total of 111 vehicles were on the collapsed portion in 2007 [4].

Damage is a local phenomena that has an impact on the structure's overall health. Thus, local monitoring is preferred but not always feasible. Therefore, local and global SHM approaches are two key categories of structural health investigation. The test structure is subjected to externally generated, ambient or harmonic or impulse-based low frequency stimulation, and the global SHM approach due to the static deflection or vibration responses in the form of displacement, velocity, and accelerations at predetermined sites along the structure. Based on the vibration data, the first few natural frequencies may not be sensitive to minor structural damage because the global vibration's wavelength is greater than that of early damage or small cracks [5].

The local damage detection techniques analyse features of structural responses corresponding to a specific portion of the whole structure. Many typical local detection techniques such as ultrasonic techniques has been developed based on acoustic waves [6, 7]. A typical drawback of local approaches is the necessity of physically moving probes, fixtures, and other equipment throughout the complex structure in order to record data [8]. SHM deals with continuous monitoring, assessment and can be put in service for establishing a satisfactory performance level of structural system. These techniques are successfully used in the industry to detect local flaws in structural components [9]. The SHM based on wave propagation has received a lot of interest recently. The Lamb wave inspection, which primarily analyzes the symmetric and antisymmetric modes of the 0^{th} order (below 0.5 MHz), is now the most used damage detection technique based on guided (between two boundaries of a plate) ultrasonic waves. By looking into Lamb wave attenuation, reflection and mode conversions, structural flaws are found. The number of modes greatly depends on the frequency range and increases with an increase in the frequency range. The main drawback of these methods, when compared to EMI, is the expensive equipment when operating at high excitation frequencies due to the higher specification requirements of both the actuating and sensing hardware. Operating at such frequencies also entails difficult and extensive data interpretation due to the dispersive nature of guided waves [10]. To reduce the complexities associated with the multi-modal nature of Lamb wave propagation, commonly used guided wave is the shear-horizontal (SH) wave and Rayleigh wave [9, 11]. In contrast to the EMI technique, which uses PZT patches that have the dual function of acting as both actuators and sensors, this method uses PZT patches as actuator-sensor pairs [12]. This requires the wave to propagate for a certain distance within the structure before a proper convergence of the elastic wave modes is ensured [13]. This distance is recommended to be around 12 times the wavelength of the excited wave [14, 15]. However, this necessitates the availability of the wave guide along this distance in the vicinity of the expected damage region, which limits the possibility of GW usage in small-sized components. Additionally, increased signal complexity is attributed to the small dimensions of wave guides due to the superposition of the wave modes with their boundary reflections [13]. Further, it has been discovered that damage sensitivity of GW declines with the propagation distance and sensor spacing [8]. Strain-based SHM employing fiber optic sensors is also one of the promising techniques for SHM currently accessible. These strain sensors can be incorporated into the material throughout the production without being intrusive or impairing the system's function. In this method, the local strain caused by the deformation due to numerous damage types results in changes in the recorded strains. These sensors will transmit different wavelengths based

on deformation and are applied along curves or even vast areas place as a sensor grid [16]. However, they suffer from the drawback of requiring high sensor densities on the structure.

In general, incipient structural damage can be quickly repaired. Therefore, a critical issue among the studies on SHM is the ability to detect minor structural damage at an early stage to prevent progressive structural degradation and potential failure. The researchers are looking for a low cost health monitoring system which is able to detect small levels of damage in light weight structures to prevent failures. Due to its potential to lower maintenance costs and extend product lifetime, EMI based SHM is an area of ongoing research. The EMI approach is frequently studied for airplanes, wind turbine blades, and civil constructions to detect delamination, adhesive bond faults, cracks, and other types of damages [17, 18]. The Fig. 1.1 shows the different important aerospace, mechanical (e.g. wind turbine [19]) and civil structure (e.g. crack in bridge [20]) which can have incipient and minor structural damage critical to the structure. The electrical impedance signature in the frequency domain serves as the primary indicator of structural health in EMI-based SHM approaches.

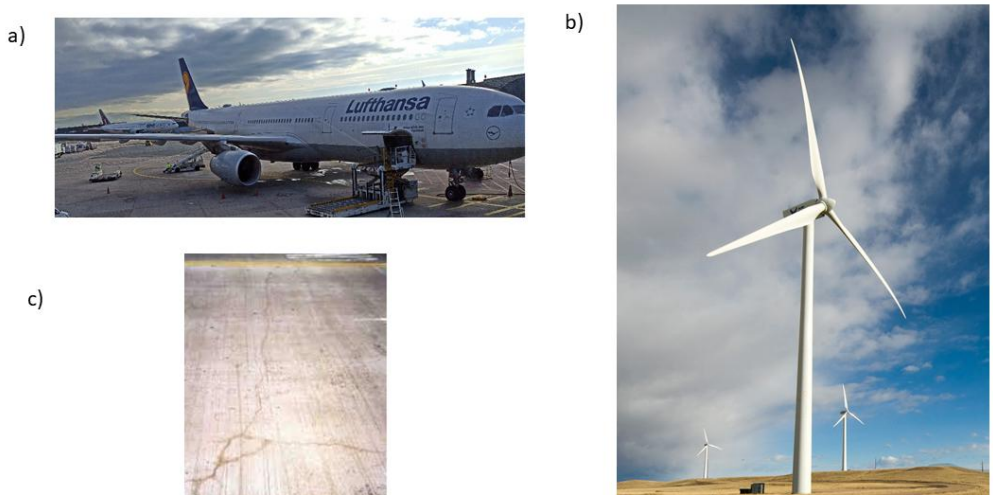

Fig. 1.1 Different type of the structures with possible incipient and minor structural damage a) aeroplane, b) wind turbine, and c) crack in bridge.

1.2 Literature review of EMI

EMI technique-based damage detection has been established for more than two decades. EMI method works in the high-frequency range and due to mechanical coupling, the electrical

response contains information about the mechanical condition of the structure. The damage evaluation approaches based on the impedance signatures by one statistical damage indicator still have limits in damage quantification and localization. A schematic diagram of the EMI-based SHM process is given in Fig. 1.2. This section provides a comprehensive review of the exciting research using the PZT-based electromechanical impedance technique (EMI).

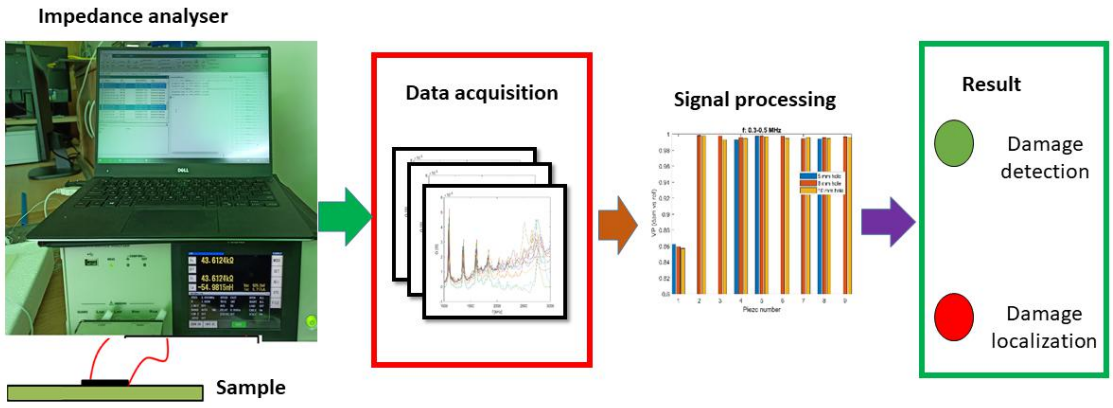

Fig. 1.2 Schematic diagram of the EMI based SHM.

1.2.1 Piezoelectricity and Piezoelectric Materials in SHM

The core tenet of the EMI approach is to use a PZT transducer to trigger structure vibration and to detect changes in host structure physical characteristics in a local area based on the transducer's EMI response. As a result, surface-bonded PZT transducers serve as both an actuator and a sensor at the same time. Eqs. 1.1 and 1.2 describe the fundamental relationships for piezoelectric materials in small field conditions.

$$D_i = \bar{\varepsilon}_{33}^{T} E_j + d_{im}^{d} T_m \tag{1.1}$$

$$S_k = d_{jk}^{c} E_j + \bar{s}_{km}^{E} T_m \tag{1.2}$$

where, D is the electric displacement vector, S is the second order strain tensor, E is the applied external electric field vector, T is the stress tensor, ε^T is the second order dielectric permittivity tensor under constant stress, d^d and d^c is the third order piezoelectric strain coefficient tensors and s^E is the fourth order elastic compliance tensor under constant electric

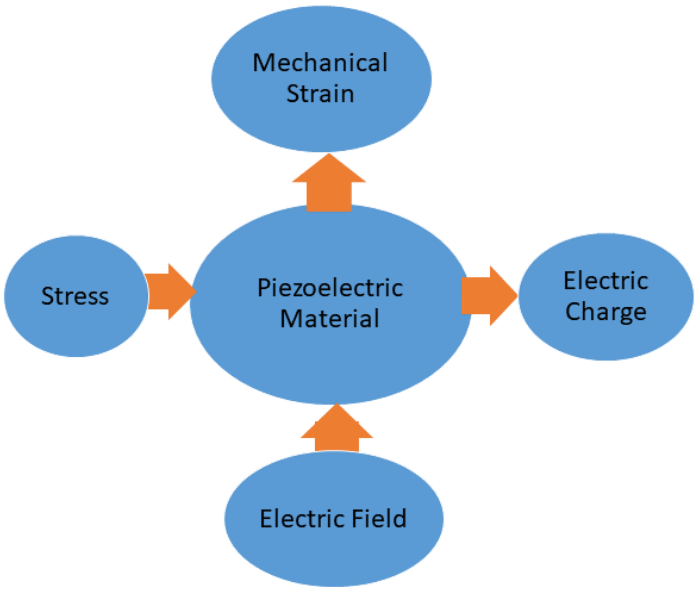

Fig. 1.3 Piezoelectric material response under different application.

field. Direct and converse piezoelectric effects are denoted by the superscripts "d" and "c" respectively.

The piezoelectric strain coefficient d^c_{jk} defines mechanical strain per unit electric field under zero mechanical stress, d^d_{im} defines electrical displacement per unit stress under zero electric field, the first subscript denotes the direction of the electric field, and the second one the direction of the associated mechanical strain [21]. Eq. 1.1 given above is utilized for sensor-based applications and describes the direct effect, or stress-induced electrical charges. The Eq. 1.2 depicts the converse effect, which is mechanical strains caused by an electric field and employed in actuator applications given in Fig. 1.3.

1.2.2 EMI principle

Fig. 1.4 illustrates a 1-D analytical model of the electro-mechanical connection between the structure and PZT to help comprehend the EMI technique proposed by Liang et al. [22, 23].

To comprehend the interaction between the PZT and the structure, Zhou et al. expanded Liang's electromechanical model to a 2-D PZT-structure model. The author used direct mechanical impedance and cross-impedance for the host structure to demonstrate the forces and their corresponding in-plane velocities [24]. Additionally, using a 2-D analytical model, Giurgiutiu and Zagrai studied the PZT transducer and impedance responses under various boundary circumstances [25]. In the subsequent development of the EMI approach, Bhalla

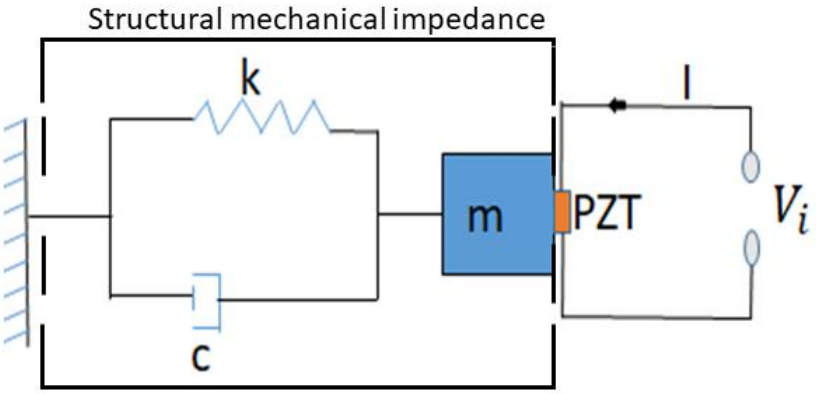

Fig. 1.4 Schematic measurement of mechanical impedance of structure using EMI method.

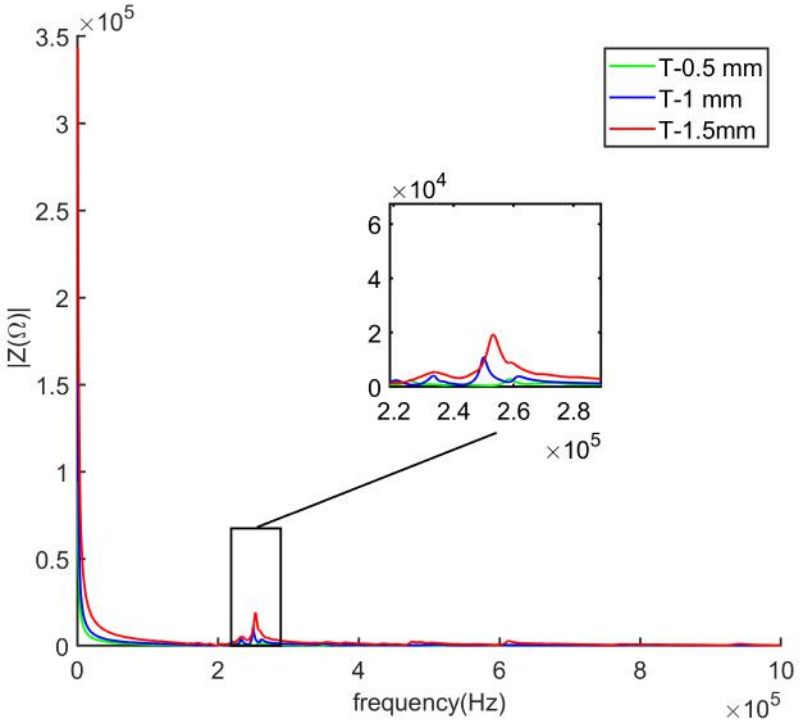

Fig. 1.5 Impedance plot of 10 mm diameter PZT of various thickness using EMI method.

and Soh exhibited the effective impedance in place of the mechanical impedance, which was directly restrained at the endpoints of the PZT patch [26]. The experimental studies on concrete structures, as used by Bhalla and Soh, were used to confirm the accuracy of the suggested modeling [27]. The two-dimensional (2-D) model was expanded to a three-

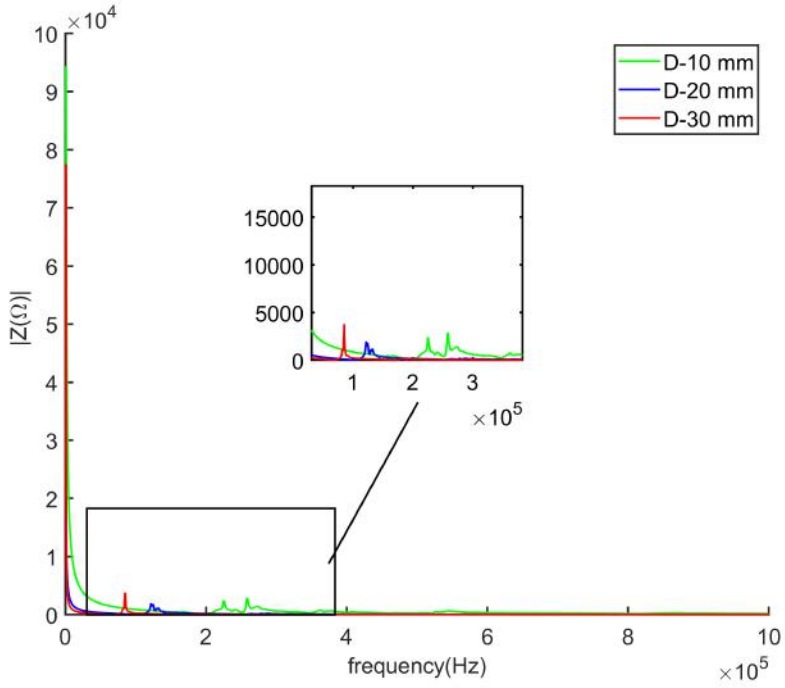

Fig. 1.6 Impedance plot of 0.5 mm thick PZT of various diameter (D) using EMI method.

dimensional (3-D) model by Annamdas and Soh in 2007. The host structure's impedance in the model is determined by adding the directional impedances acting on the PZT structure [28]. Using symmetry in the X and Y directions, the authors created a 3-D FEM of the host structure, PZT patch, and bonding layer in ANSYS to compute the EMI responses using only one quadrant of the structure. The voltage (V) applied to the bonded PZT divided by the electric current (I) flowing through it is the electrical impedance (Z(ω)) of the PZT and is given by Eq. 1.3 [29].

$$Z(\omega) = \frac{V}{I} = \frac{1}{j\omega}\frac{h_p}{\bar{\varepsilon}_{33}^2 \pi a^2}[1 - \frac{2d_{31}^2}{\bar{s}_{11}^E \bar{\varepsilon}_{33}^T (1-\nu)}[1 - \frac{1}{\frac{Z_a(\omega)}{Z_s(\omega)} + 1}(\frac{2}{\bar{\phi}})(\frac{J_1(\bar{\phi})}{J_0(\bar{\phi})})]]^{-1} \tag{1.3}$$

where, $\bar{\phi} = \frac{\omega}{\bar{c_p}}a$, $\bar{c_p} = \frac{1}{\sqrt{\rho \bar{s}_{11}^E (1-\nu^2)}}$, $\bar{s}_{11}^E = s_{11}^E(1 - j\eta)$, $\bar{\varepsilon}_{33}^T = \varepsilon_{33}^T(1 - j\delta)$, J_0 and J_1 are zero and first order Bessel function of first kind respectively, Z_a is the short-circuited mechanical impedance of piezoelectric transducer (actuator), Z_s is the mechanical impedance of structure, h_p - thickness of piezoelectric transducer, a- radius of transducer, ρ - density, s_{11}^E is compliance coefficient , d_{31} is the piezoelectric coefficient of transducer for direction 3-1 (electric field applied in direction 3, strains in direction 1), j complex symbol, ε_{33} is the

complex permittivity of piezoelectric transducer for direction 33, η is the mechanical loss factor and δ is dielectric loss factor.

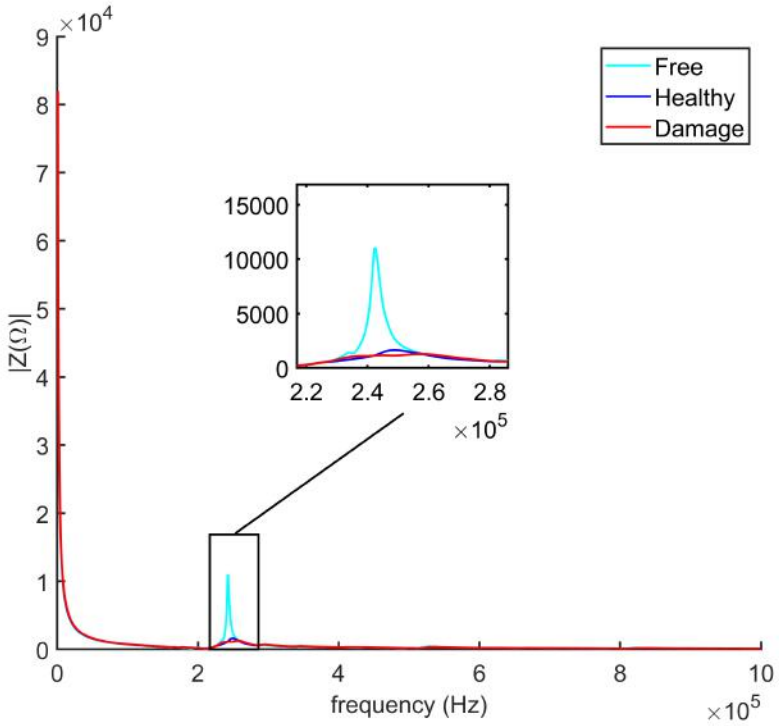

Fig. 1.7 Impedance of various structural response of PZT using EMI method.

Fig. 1.5 and Fig. 1.6 depict a comparative study of free SONOX P502 PZTs based on increasing thickness and diameter respectively. As the thickness increases, the impedance of the PZT is increasing, and resonance maxima occur for T-1.5 mm thick PZT. According to the study, early maxima occur for large size (D-30 mm) PZT between 1 kHz and 1 MHz in |Z| plot. The smallest size PZT of 10 mm diameter and thickness of 0.5 mm is chosen to give the least amount of weight and space addition in the lightweight structural investigation with minimum alteration mechanical properties like impedance etc. at a higher frequency. Fig. 1.7 shows the structural conditions in form of electrical measurements using the impedance of signals. The |Z| plot shows the response for the free, healthy, and damaged conditions of the structure. When the free sensors bonded to a healthy structure, there is a sharp drop in the |Z| resonance peak of the free actuator. Further, In damaged structures, an anomaly was detected in electrical response with respect to healthy structural response.

Different methods for acquiring information were used in the most recent development of the EMI technique. This results in the daunting task of developing a data processing method sensitive to minor degrees of degradation. The most recent state-of-the-art of data processing

algorithm based on EMI damage detection methods fall into two categories: data-driven EMI techniques and physics-based EMI techniques. These techniques' benefits and drawbacks are described below.

1.2.3 Physics based SHM using EMI

Damage identification is treated as an inverse model update problem based on optimization theory in physics-based EMI approaches. The host structure's mechanical characteristics can directly affect one or more impedance responses. The mechanism between variations in impedance response and structural damages can be well understood using EMI approaches based on physics. The changes in the impedance response are directly related to one or more mechanical properties of the host structure. Gadomski et al. investigated the electrical resistance of bending beam-shape specimens under static and periodically varied loads and discovered that measuring electrical resistance change provides more information about the destruction of a CFRP structure than measuring the stiffness of the laminate [30]. Several physics-based EMI damage diagnosis techniques have been researched in the past ten years, taking advantage of precise numerical modeling for PZT-structure interaction. To forecast the impedance output of a PZT transducer, Fairweather and Craig created an analytical model incorporating the finite element approach. The advantages of anisotropic material and non-uniform boundary conditions were utilized in the FEM modeling [31]. For the purpose of identifying damage, Naidu et al. used indicators of mode shape vectors and the nature of frequency shifts. From the numerical simulation of a 2-D FEM of the intact structure, the frequency shifts pattern has been used to identify damage at various locations, and the mode shape corresponding to the damaged structure is then identified by looking for the similar frequency shifts signatures with a Bayesian network model [32, 33]. The magnitude and location of the stiffness change in the host structure are estimated using differences between the simulated and measured impedance signatures developed by Xia et al. [34]. For the smaller aluminum beam and plate, Yang et al. developed the impedance-based 2-D generic model for the damage diagnosis technique. The interaction between the host structure and the PZT patch resulted in a slight shift of the peaks from the natural frequencies, which suggests that the small-size PZT patch can be permanently bonded to the structure for on-line health monitoring without significantly altering its mechanical properties [35]. Damage was represented by Xu et al. as a decrease in the structural material's Young's modulus. Peak frequencies of the calculated impedance responses would match the measured impedance data for the highly reliable structural damage parameters quite well [36]. For several finite element simulations, Yang et al. explored a free PZT patch and PZT-structure interaction for an L-shaped aluminum beam while considering the bonding layer and temperature variation into

consideration. PZT patches with thick bonding thickness and high stimulation frequencies should be avoided, especially at high temperatures [37]. Based on a precise numerical simulation performed with ANSYS, Zhang et al. produced a quantitative simulation of the impedance response of a Timoshenko beam with a crack. The findings demonstrated that the frequency range of the impedance signature had an impact on the precision of damage identification [38]. In order to increase the precision of impedance response predictions over a wide frequency range (0 kHz-1 MHz), Lim and Soh adopted a hysteretic damping model in place of the traditional Rayleigh damping model [39]. In both 1-D and 2-D analytical models, Lim et al. conducted the parametric research for the single PZT patch under free vibrations. According to the study, PZT mechanical characteristics have a greater impact than PZT electrical properties [40]. The association between the variations in impedance signatures and the changes in structural characteristics of the host system needs to be correlated using analytical models based on information about the location and severity of structural damage. By ranking the relative similarity and utilizing a Bayesian inference strategy in the EMI damage detection method for the beam structures, Shuai et al. established the finite element model (FEM) [41].

A pre-screening EMI technique employing statistical calibration and a surrogate model was proposed by Ezzat et al. [42]. A Gaussian process surrogate model, which was utilized to depict the relationship between the specific structural attribute and the impedance variations, was then used in the statistical calibration method. The best agreement between the final calibrated model and the measured physical values is then produced by using a number of pairs of damages with varying severity and locations. Effective structural mechanical impedance was employed by Ai et al. to identify damage in reinforced concrete (RC). For the purpose of detecting damage, they compare the efficacy of electromechanical admittance, structural mechanical impedance, and effective structural mechanical impedance signature [43]. Recently, Zhu et al. suggested a thorough active monitoring strategy that uses a modified electromechanical impedance analytical model to directly couple mechanical impedance-based signature extraction. They located and measured the degree of disbond inside the structures using the RMSD index [44, 29]. Using the analytical approach, it is a daunting task to create an accurate simulation of impedance for complex geometries such as hollow objects or those with slots. Finite element methods have been used to analyze the impact of structural damage based on the development of FEM for the EMI methodology. For more accurate simulation results of complicated geometry and material properties, employ the FEM approach. The fact that the FEM requires a fine mesh size that is smaller than the wavelength involved is one of its most notable disadvantages. The finite element model needs a lot of elements in order to accurately anticipate EMI responses, which comes at

a significant computational cost for the numerical simulation. Studies using the spectral element technique (SEM) to solve the high frequency EMI problem have drawn a lot of attention since they can increase computing efficiency. For instance, Albakri and Tarazaga presented an EMI technique based on SEM for characterizing structural deterioration in an aluminum beam. The created method relies on the length-varying spectral elements to reduce the element count with minimal computational expense [45]. By integrating the gradient descent approach with the sine-fit localization method, the necessary objective functions were minimized to estimate the crack's location and width. In similar way, Esteban et al. developed the SEM incorporated with the existing 1D analytical model (Liang et al.) to evaluate the sensing region of the EMI of a PZT transducer [46]. Ritdumrongkul et al. also used a modified SEM model based on the active restricted layer SEM model to simulate bolt joint connections. This technology has a significant potential for quantitatively monitoring structural damage since the loosening of bolts may be quantified as a change in stiffness and damping at the bolted connection [47]. Fiborek et al. carried out time-domain SEM for the broad frequency range of up to 5 MHz. The piezoelectric transducer attached to the two different types of composite plates has simulated R and G EMI spectra that are in good agreement with experimental results [48].

It is straightforward to achieve the repeatability of monitoring results in the structure by using an EMI response that is physics-based. Physics-based approaches are constrained by the shortcomings of many modeling strategies, such as a few FEM techniques based on PZT-structure interaction and SEM modeling in the high frequency range. Furthermore, using physics-based modeling strategies for things with complex geometries is difficult. The accuracy of simulation using finite element modeling with high computing efficiency is a significant hurdle since the scales of predictable damage and the accuracy of results are strongly dependent on the mesh size [49]. The sensitivity-based EMI technique's damage identification method modifies the numerical model's physical parameters across a number of iterations. Numerous unknowns are also introduced utilizing different aspects with the goal of finding structural degradation. The various meta-modeling approaches, such as machine learning networks, still require in-depth discussion and comparison. In addition, resolving the sensitivity-based inverse identification problem is the foundation of all current fundamental EMI techniques based on physics. Investigations should be done on the topic of sensitivity matrix derivation for complicated structures. Future research on simplified, effective, but accurate numerical modeling techniques for complicated 3-D structures or effective algorithms for handling highly uncertain, inadequately stated inverse identification problems may be the key themes of physics-based EMI technologies. The beam structure is the only successful application in this field [50].

1.2.4 Data driven SHM using EMI

The development of a data-driven methodology to precisely locate and assess the severity of structural flaws is an emerging area of research [51]. To increase the functionality of these approaches and the use of impedance signatures, traditional machine learning approaches, new deep learning approaches, and other pattern recognition algorithms are integrated with EMI. A data-driven based approach is more suitable than a model-based approach when mathematical modeling of the system is not of interest [52]. For the current data-driven based EMI methods, quantification of the difference between the baseline and measured impedance signatures is the key to deciding whether the damage occurs in the engineering structures. The typical data-driven based EMI methods for SHM are detailed reviewed and discussed in this section.

Statistical damage index methods

Based on a comparison of the healthy and damaged spectrum, this method employs measurements to identify the damage. The most popular damage studies, which compare the healthy and damage spectrums, are based on correlation coefficient (CC), mean absolute percentage deviation (MAPD), and root mean square deviation (RMSD). RMSD statistical damage detection indices in EMI techniques proposed by Giurgiutiu and Rogers. Eq. 1.4 is used to quantify damage with respect to a healthy state of the structure in the EMI techniques [53, 54].

$$RMSD = \sqrt{\frac{\sum_{i=1}^{n}(D_i - D_i^o)^2}{\sum_{i=1}^{n}(D_i^o)^2}} \tag{1.4}$$

Other statistical damage indicators, such as MAPD, COV and CC, have been developed and given by Eq. 1.5, Eq. 1.6 and Eq. 1.7 [49, 55, 21]. Based on study, RMSD is the most sensitive for spotting newly occurring damage [56].

$$MAPD = 100/n \times \sum_{i=1}^{n} |(D_i - D_i^o)/(D_i^o)| \tag{1.5}$$

$$Cov = 1/n \times \sum_{i=1}^{n} (D_i^o - \bar{D^o})(D_i - \bar{D}) \tag{1.6}$$

$$CC = \frac{Cov}{\sigma^o \sigma} \tag{1.7}$$

where symbol n is used for number of frequency spectrum samples, D_i is the damage state data at the i^{th} frequency. D_i^o is the healthy state data of single sample of the spectrum for $(i)^{th}$ frequency. σ^o and σ are the corresponding standard deviations of healthy and damage signature.

Recently, these statistical damage indices have also been used to quantify damage to various engineering components and structures by setting thresholds [57–60]. The authors evaluated damages including concrete crack damage, propagating fractures in aluminum beams and freezing-thawing. These damage indices' main flaw has been their inability to accurately locate structural damage or measure its severity without the aid of a numerical model or previously calibrated experimental data [61–63]. There is a wide range of information to be extracted from impedance response data to indicate the difference between damage nearer to the PZT sensor and structural damage with high severity [64]. Additionally, it is challenging to differentiate between changes in impedance patterns brought on by actual defects and other environmental changes [64, 65]. The EMI signature of the various frequency intervals was used to calculate a chessboard distance measure to determine the degree of damage under various temperature settings. The airplane wing segment severed from its trailing edge was the one taken into consideration as a structural component [66]. It might not be enough to simply summarize the impedance signature using a single damage indicator. It is necessary to look at how the noise in the measured impedance signals and the quantity of available frequency shifts affect the effectiveness of the suggested damage diagnosis approach [63, 67].

Machine learning methods

Numerous data processing and pattern recognition techniques have been implemented to improve the effectiveness of EMI approaches to detect damage. Artificial Neural Networks (ANN) are one of the most advanced machine learning techniques. Nazarko et al. used ANN for novelty detection and damage size estimation of notched strip specimens made of various materials (aluminium, steel, Plexiglas) [68]. Fekrmandi et al. developed the ANN-based EMI technique employing the Square of Differences (SSD) indicator between impedance responses for network training [69]. Using the EMI approach, Na and Lee used Probabilistic Neural Networks (PNN) to identify damage in composite structures. For damage prediction, the training data employed RMSD damage index values from split sections of the structure calculated from the PZT transducers bonded at various positions [70]. Using the PNN approach and a condensed version of the fuzzy ARTMAP Network, De Oliveira and Inman analyzed the impedance response for the identification of loosening bolts at various phases. The suggested ARTMAP network may deliver an accurate identification result and

greatly reduce training time, according to performance comparisons using the same training input of the Euclidean distance [71]. Djemana et al. employed an extreme learning-based machine learning method to locate the damage using an EMI approach simulation model for both short and long beams. In order to train and evaluate the model, they used data in the frequency ranges of 10–50 kHz and 60–70 kHz [72]. Meher et al. used a single hidden layer backpropagation ANN to identify damaged features in a metallic bolted structure and identify loose bolts. The RMSD and CC of damage G with respect to the G in the healthy condition are used to derive damage features [73].

The use of principal component analysis (PCA) for damage detection and classification is receiving attention as well. Using impedance data and a PCA model, Park et al. were able to locate all loose bolts in the wireless SHM's bolted aluminum plate construction. They employed an on-board active sensor system made up of macro-fiber composite sensors and impedance measurement chips (AD5933) [74]. Quin et al. employed PCA-based Q statistics and T^2 statistics to diagnose and locate faults in the manufacturing process of the polyester film [75]. To find and distinguish damages in steel plate and turbine blade structures, Mujica investigated various statistical methods. For the first two projections to examine the Q-statistic and T^2-statistic indices, data from sets of experiments for undamaged and damaged scenarios are projected into the PCA model [76].

Deep learning method

Convolutional neural networks (CNNs), which are based on deep learning, have recently been investigated for pattern recognition and classification. For the accuracy of damage prediction in deep learning networks-based EMI approaches, a huge collection of different training examples is needed. De Oliveira et al. successfully identified four different structural situations encompassing three different damage categories in order to increase the damage detection accuracy of the EMI based approaches in complex structures [77]. In this work, the CNN architecture and the EMI technique are combined. The effects of three distinct constant temperature levels on three aluminum beams were investigated. For damage prediction of artificial damages like mass addition, a one-dimensional CNN was created, trained, and employed [78]. To find, measure, and locate structural damage, Osama Alazzawi et al. developed CNN based algorithm using a hybrid training approach. Experimental testing of the suggested technique involved collecting samples of time-domain PZT impedance response signals from a steel beam, both damaged and undamaged. The first layer of damage detection has been completed, and the second layer of damage assessment has been completed with respect to three damage size conditions in two places [79]. The graph convolutional network (GCN) was implemented by Zhou et al. for the various sensors system to locate

and quantify bolt loosening. The GCN approach may quantitatively infer the torque loss of several bolts through node-level outputs by taking into account both the EMI signature and the link between the sensing nodes and the bolted joints [80].

Both the traditional machine learning techniques and the cutting-edge deep learning techniques are totally data-driven, and the effectiveness of these techniques is greatly influenced by the quality and variety of training data. However, due to the restriction on the number of sensors, external noise, the incompleteness of the observed state variables, and boundary conditions with several possible damage situations, gathering such sufficient data in real applications is incredibly challenging. The pattern recognition approach based EMI technology typically needs numerous sensors because of this. It might restrict the use of these strategies to relatively small-scale constructions.

Clustering technique

The majority of recent work on data-driven EMI approaches are based on the concepts of clustering and pattern recognition. The accuracy and generalizability of these pattern recognition systems were mostly influenced by the indicators chosen for classifying patterns. Using impedance data and a PCA model, Park et al. were able to locate any loose bolts in the bolted aluminum plate. The RMSD damage indicators of each order of the primary components are used as the basis for the pattern recognition process utilizing the K-means clustering technique. According to experimental testing, the proposed technique successfully identified bolt loosening in a bolt-jointed aluminum structure [74]. Additionally, the scientists coupled the k-means clustering-based methodology with unsupervised hierarchical clustering for damage detection on the near surface of mounted fiber reinforced polymers using the EMI technique. The authors attempted to divide various loading stages of the structure in the cluster using this technique [81]. In a relatively small frequency range, Junior et al. used a self-organizing maps (SOM) classification architecture with RMSD characteristics of the actual component of impedance. The multipoint metal dressing tool's characteristics shown a considerable improvement in EMI-based damage classification [82]. Sevillano used the statistical index of each sub-frequency interval to execute the hierarchical clustering technique in order to identify the pattern of impedance responses. The experimental studies shown that the method can detect consistent debonding in RC beams that have been strengthened with Fiber Reinforced Polymers (FRP) [83]. Fuzzy cluster analysis was used by Palomino et al. for the categorization and identification of damage based on an EMI approach. As the first signs of damage, a loose rivet and a 1 mm-diameter hole were made in the beam structure. The suggested method was successful in differentiating the damage kinds, although damage severity measurement was not done [84]. The k-NN machine learning algorithm is utilized

to generate classification models by learning from simulated response data and three sets of experimental data with additional noise. The created classification models' used to detect delamination damage in CFRP composite plates [85].

Data fusion based approach

As discussed in the preceding sections, the EMI approach used a variety of variables and several sensors to gather information. Multiple sensors were employed by Zuo et al. to locate pipeline system cracks. They obtained the damage-sensitive feature from the raw admittance's active component [86]. Eight PZT sensors' average value and standard deviation of the RMSD indices were utilized to calculate the crack's size within statistically acceptable parameters. The baseline data used was the average effective impedance as determined by a Monte Carlo simulation. Based on the Rotation Forest (RF) approach and the Dempster-Shafer (DS) theory, Zhao et al. introduced the hierarchical ensemble scheme to data fusion in which RF was employed to create a precise and varied base, while DS was used to aggregate the RF data output [87–89]. ANN, support vector machines (SVM), and deep learning are feature level fusion-based machine learning algorithms that are growing in popularity in data fusion, according to Wu et al. [49]. For the purpose of locating and detecting fractures on the metallic surfaces of nuclear power plant reactors, Chen recently suggested a deep learning-based data fusion idea. In order to improve the system's overall performance and robustness, CNN aggregates the data retrieved from each frame using the Naive Bayes data fusion scheme [90].

The data fusion from the sensors is more the emphasis of the EMI technique's trending data-driven approach to damage identification. It is known that employing numerous sensors is more efficient than doing so with just one [55]. Data fusion is the process of combining data from diverse sources to lessen uncertainty and provide data with a higher signal-to-noise ratio. The data-driven EMI techniques only provide phenomenological characterizations of impedance changes without formulating the relationship between the impedance responses and changes in mechanical parameters of the host structure, but such combinations successfully identify and characterize structural damage. With insufficient impedance data and no theoretical foundation for choosing an acceptable frequency range, achieving high accuracy and repeatability of damage identification remains a significant challenge.

1.3 Research Gap and Objectives

The majority of studies in the development and application of EMI-based SHM approaches to analyze the frequency domain impedance signature estimated by Fourier transform and

establish specific damage indicators. These damage indices are simple to calculate and can be used to detect structural damage. However, a significant difficulty and cause for concern is their sensitivity in identifying localized small damage, particularly in large-size structures. Thus, the first objective of this research is to improve structural damage detection performance by sensor level or variable level data-fusion analysis in the frequency-domain EMI responses from piezoelectric transducers.

The EMI method's effectiveness depends on the selection of an effective frequency spectrum which is usually hard to determine for the incipient damages in the structure. There is no established theoretical methodology to determine the effective frequency range of the transducer from the experimental data. The robust frequency range of damage detection in EMI method can be determined using trial and error method till now [91, 92]. By examining the frequency-domain EMI responses from piezoelectric transducers, this study's second goal is to develop a theoretical data-driven approach for the proper selection of frequency ranges.

The third objective of this thesis is to expand from damage detection to damage localization by accurately imaging the single and multi-damaged locations using the data fusion technique. The proposed damage indicator signals based damage index (DI) will be compared with a variety of EMI-based damage indicators to demonstrate the performance. Further, an inverse model and multi-damage detection are demonstrated to optimize sensor location based on damage imaging.

The fourth objective of this research is to reduce the measurement time using series and parallel combinations of the Impedance analyser electrodes for damage detection based on analysing the frequency-domain impedance responses from piezoelectric transducers. This research is also conducted to investigate the effects of temperature variation on the different type of connections to verify the performance.

The major aim of this thesis is that it can provide robust data-driven data-fusion based approaches to enhance damage detection and localization performance for metal, composite and 3D printed structures. The thesis to be proven are:

- **The data fusion techniques are enhancing performance compared to the conventional approach for damage identification.**
- **Sensor network-based damage localization accurately predicts single and multi-damage locations.**
- **A data-driven theoretical effective frequency range selection is possible that enhances the performance of data fusion-based damage detection and damage severity quantification.**

1.4 Organisation of dissertation

The first chapter of the thesis discusses its scope and objectives. This chapter presents the most recent damage detecting technology based on PZT based EMI method to enhance knowledge about current research. In addition, state-of-the-art EMI damage detection approaches feature a more targeted data driven data fusion approach. The ultimate objective is to apply technique to practical structures, but the challenges that come by complexity of structure force me to move from simple structures to more complicated structures.

The conceivable series and parallel connection-based combination study based on the fusion of two sensor data is covered in the second chapter. Sensor series and parallel combination data are the subject of a theoretical and experimental investigation to shorten the measurement time of the structures. Robust combined sensor damage detection in a range of environmental temperature condition is investigated.

The third chapter includes scope of the variables level and sensors level EMI data fusion techniques and state that how these techniques are helpful in the performance improvement of damage detection. Further, demonstration of the new damage index of the F and PCA for various experimental data for the robust EMI damage detection technique.

The fourth chapter discusses the sensor network based damage imaging approach for single and multiple damage detection using optimise sensing region radius for GFRP plate and 3D printed plate. This section includes an introduction to the probabilistic damage imaging approach and a comparison of how the methodology is implemented using various damage measurements, DCMI, fused F data, etc. Additionally, an inverse model implementation can precisely pinpoint the damage.

The fifth chapter discusses the necessity for a theoretically sound and practical approach for frequency range selection. This section of the thesis will introduce effective frequency range selection based on standard deviation and a further probabilistic integral method to damage diagnosis based on variable data fusion. The procedure serves as an example for a variety of experimental data for the EMI damage detection method.

The last chapter concludes the outcome of the research topic and states the major contribution with recommended future works.

Chapter 2

Damage detection via data fusion of PZTs based on series and parallel connections

The data acquisition in continuous monitoring of the structures is time-consuming and generates a large amount of data. In general, there are many temperature compensation based algorithm investigated theoretically and experimentally. However, there are limited number of measurement based robust techniques designed to minimize temperature variation effect in the damage detection. This chapter successfully demonstrates the advantage of a multi-sensing parallel combination of the EMI-based damage detection. This work describes the EMI based damage quantification using fusion of two piezoelectric transducers on the steel beam structure. Utilizing the resistance of two sensors, the series and parallel combinations were examined, and the output of various sensor arrangements were compared. This methodology enhanced the scope of study from individual connections of the actuators to fusion based damage detection. This chapter is noteworthy in that it focused on using a breadboard, a simpler method, to shorten measurement times for the structures while also using a robust parallel connection method to investigate damage sensitivity even in a temperature-varying environment.

2.1 Need and scope of the combined sensor study

In order to correctly detect damage and determine whether the time required for measurements is decreased or not, this section of the chapter covers the requirement and extent of the selection of the series and parallel combinations investigation. Adhikari et al. proposed a modified dual piezo configuration whose sensitivity increases with increasing number of actuators connected in parallel due to an increase in the output current. The proposed

integration enables an early detection of damage, and improved severity measurement for reinforced concrete structures [93]. Chen et al. investigated the bolt looseness by using series multi-sensing technique based on sensor arrangement. They used series connection of smart washers to obtain impedance signal in one sweep. The proposed 3 dB RMSD can quantitatively assess the level of bolt looseness based on the 3 dB bandwidth that the analogous circuit defines [94]. Balamonica et al. [95] also used multi-sensing technique based on series and parallel to accelerate the data acquisition process. The authors investigated the damage detection in reinforced concrete from sensors patches individually and through multiplexing for maximizing the efficiency using conductance data. Further, Priya et al. has used multi-sensing approach using PZT sensors on carrier plates of different thickness plate for monitoring age strength in concrete due to improper curing. The authors have analyzed the embedded sensor's conductance data using damage metrics like moving RMSD, MAPD, and CC [96]. However, their research focused only on accelerating the data acquisition process; no one has yet demonstrated the value of the specific connections, and neither has the method's performance in environments with varying temperatures. There are many experimental study on temperature effect of PZT and structure and has been shown that changes in the operating temperature of structure has similar effect to the damage introduce in the structure [97]. The effect of temperature observed on the real part of impedance and conductance and horizontal shift behave more differently in the high range impedance frequency samples [98, 99]. To minimize the temperature effect on impedance measurements cross correlation based compensation method used using effective frequency shifts and vertical shift based on the average of difference of signatures initially [98, 100]. However, the results are satisfactory for the narrow frequency bands. In [99], entire frequency band divided into smaller frequency band to implement effective frequency shift based method.

The damage evaluation based on EMI on the steel beam structure using two piezoelectric transducers is explained in this chapter. Along with the theoretical approach that was suggested for serial and parallel connections, **resistance data fusion** was put to the test. The damage assessments of employing two sensors had shown the advantage of using a parallel connection on the basis of the steel beam with the added weight that was used as an example. The mass was finally identified, and the measuring time was cut in half. The method covered in this chapter uses two sensors operating in tandem to lessen the impact of temperature change. For the various damage scenarios, the series, parallel, and individual electrode connection combinations were examined and compared. The chapter examines the RMSD and MAPD damage indices for the simulated additional mass and depth cut (crack) on steel beams under conditions of low-temperature variability.

2.2 Theory and experimental setup for the investigation

EMI-based damage estimation on the steel beam structure utilizing two piezoelectric transducers is described in this section of the chapter. The advantage of employing a parallel connection was demonstrated on the steel beam with added mass using the theoretical approach for modeling serial and parallel connections that were put forth and tested. The damage sensitivity of this approach is studied using experimental signals and the statistical indices RMSD as described in Eq. 1.4. This chapter also focuses on the both parallel and serial connection of the PZT transducers under limited varying temperature conditions. The temperature sensitivity was studied based on an analytical concept and implemented with an experimental EMI signal in the limited temperature variation changes. The arrangement has been done for the two PZTs of the series and parallel connections to get composite signals for the resistance data.

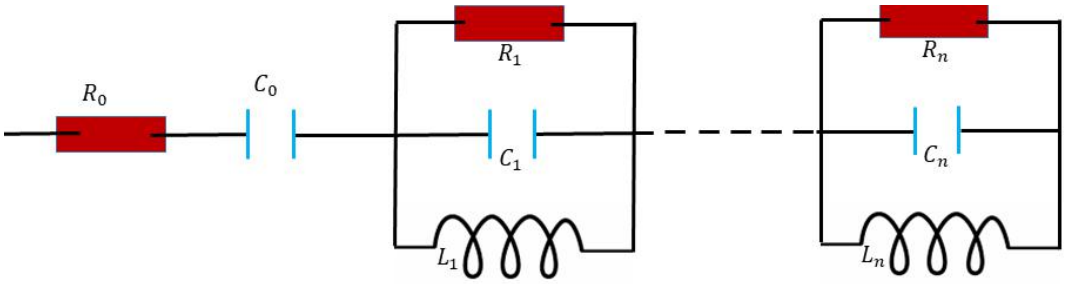

Fig. 2.1 Coupled diagram of n PZTs impedance.

The coupled n PZTs impedance, as depicted in Fig. 2.1, can be expressed by Eq. 2.1 as follows [101].

$$Z_{coupled}(\omega) = R_0 + \frac{1}{j\omega C_o} + \sum_{i=1}^{n} \frac{1}{\frac{1}{R_i} + \frac{1}{j\omega L_i} + j\omega C_i} \tag{2.1}$$

where n is number of PZTs, R_i, L_i, and C_i are analogous to mechanical damping, mass, and elastic compliance respectively for the i^{th} PZTs. R_0 and C_0 stand for resistance and capacitance, respectively [102]. The capacitance of a two-terminal device is a measure of the redistribution of electric charge that occurs as a consequence of a change in the applied voltage [94, 101]. Then from Eq. 2.1, the resistance $R(\omega)$ of the first PZT can be written by Eq. 2.2.

$$R(\omega) = R_0 + \frac{R_1 \omega^2 L_1^2}{\omega^2 L_1^2 - R_1^2(\omega^2 L_1 C_1 - 1)^2} \tag{2.2}$$

Then, using Eqs. 2.3 and 2.4, we can determine the resultant resistance in series ($Rs(\omega)$) and parallel ($Rp(\omega)$). Further, substituting the value of $R_1(\omega)$ and $R_2(\omega)$ using Eq. 2.2 in the Eqs. 2.3 and 2.4.

$$R_s(\omega) = R_1(\omega) + R_2(\omega) \tag{2.3}$$

$$\frac{1}{R_p(\omega)} = \frac{1}{R_1(\omega)} + \frac{1}{R_2(\omega)} \tag{2.4}$$

$$R_s(\omega) = \sum_{i=1}^{2} [R_0 + \frac{R_1^i [\omega L_1^i]^2}{[\omega L_1^i]^2 - [R_1^i(\omega^2 L_1^i C_1^i - 1)]^2}] \tag{2.5}$$

$$R_p(\omega) = 1/\sum_{i=1}^{2} 1/[R_0 + \frac{R_1^i [\omega L_1^i]^2}{[\omega L_1^i]^2 - [R_1^i(\omega^2 L_1^i C_1^i - 1)]^2}] \tag{2.6}$$

The difference between a series connection and a parallel connection in terms of resistance value is demonstrated by Eqs. 2.5 and 2.6 respectively. A series connection accumulates resistance amplitude, whereas a parallel connection suppress amplitude. When connecting the combined signal in parallel, the output external effect resistance is smaller; when connecting in series, it is larger.

A steel beam (35.5 x 3 x 0.3 cm^3) is used for the EMI experimental research, together with attached piezo-actuators p1 and p2, as illustrated in Fig. 2.2. Using a breadboard and connecting wires, the IM3570 Impedance Analyzer was utilized to measure the EMI signatures at the piezo-actuator terminals. The experiment used surface-bonded SONOX P502 PZTs (actuator/sensor) with a 10 mm diameter and 0.5 mm thickness. The study examines three damage scenario of the EMI responses: 50 gram additional mass at distances of 3 cm from the p1 transducer as shown in Fig. 2.3a, 50 gram and 5 gram at 3 cm from the left side's extreme end as shown in Fig. 2.3b and Fig. 2.3c respectively. In addition, a crack is simulated at 1.2 cm from the end by employing a saw-cut to remove material from the steel beam. The temperature of the environment increased from the 19 $^{\circ}C$ to 23 $^{\circ}C$ and further 30 $^{\circ}C$ to investigate the sensitivity of damage in the changing environment of laboratory. Using a refrigeration system, lower temperatures (19 $^{\circ}C$ and 23 $^{\circ}C$) were maintained in the cooling mode while higher temperatures (30 $^{\circ}C$) were recorded in the heating mode. However, the average outside laboratory temperature was 15 $^{\circ}C$.

Using a sweep sine wave signal, 1V of excitation is selected as the excitation magnitude for the tests. The following symbols, as indicated in Fig. 2.4, were allocated to the sensors' connections and the corresponding measurements: p1 and p2 – single sensors, p12s –series combination, and p12p – parallel combination.

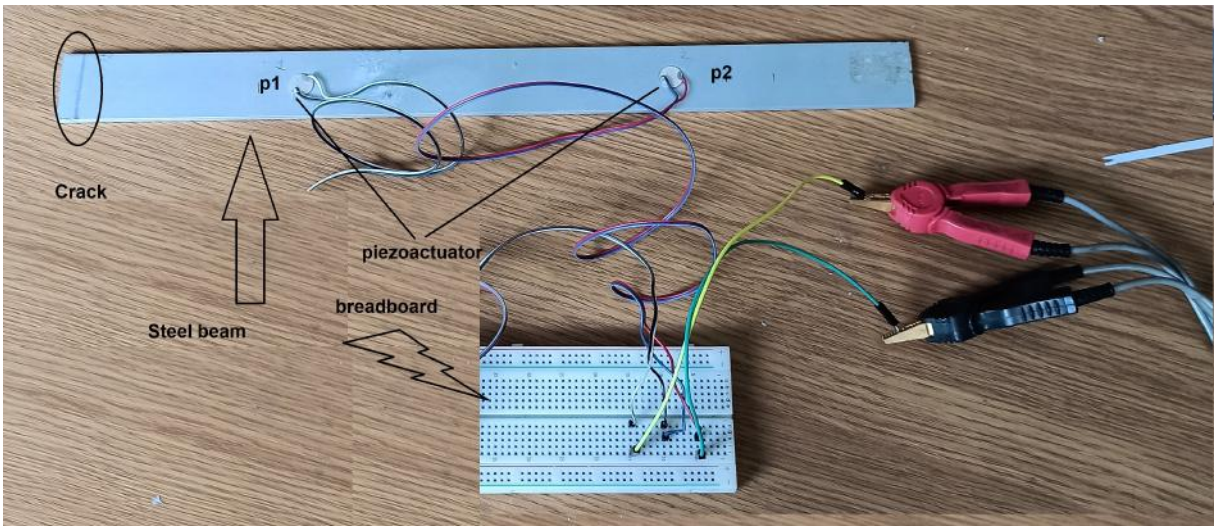

Fig. 2.2 Diagram of sensor connection using breadboard for the damage detection in the steel beam.

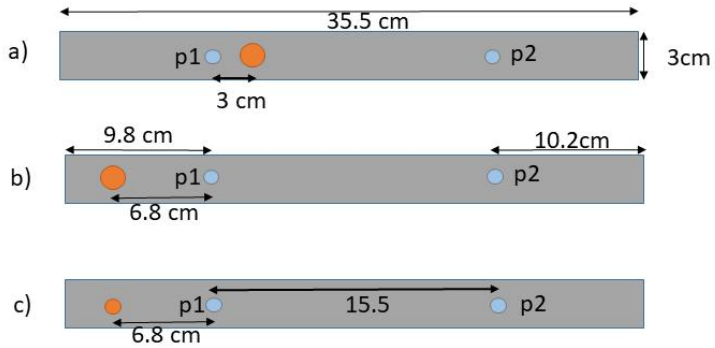

Fig. 2.3 Diagram of p1 and p2 with different damage conditions in the steel beam structure.

2.3 Comparative study of parallel combination with other mode of combinations

Two PZT individual (p1, p2), series (p12s) and parallel (p12p) resistance raw data plot of the healthy state spectrum are shown in Fig. 2.5. The symbol 'H' is used to denote the healthy state measurement. The experimental steel beam data were collected in the 1 kHz–4 MHz frequency range, and good deviation of the healthy and damaged state data was found in resistance for frequency ranges of 1-100 kHz for the simulated added mass and 30-80 kHz

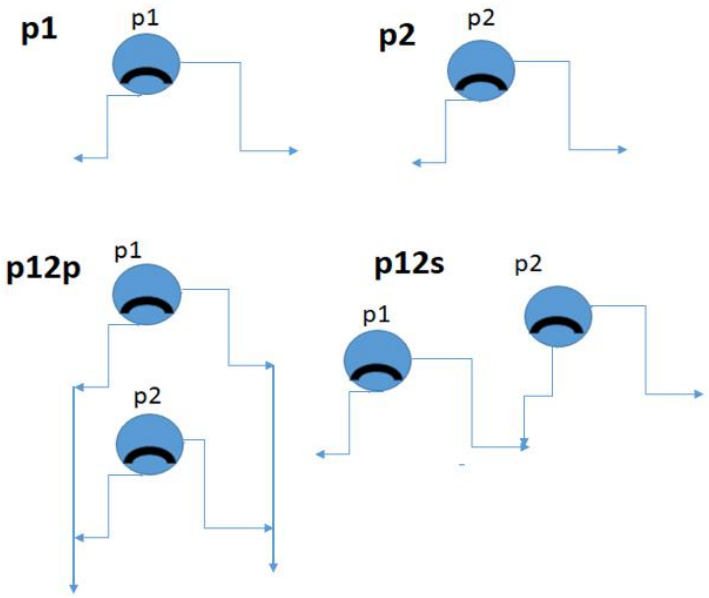

Fig. 2.4 Diagram of sensor connection using breadboard for the damage detection in the steel beam.

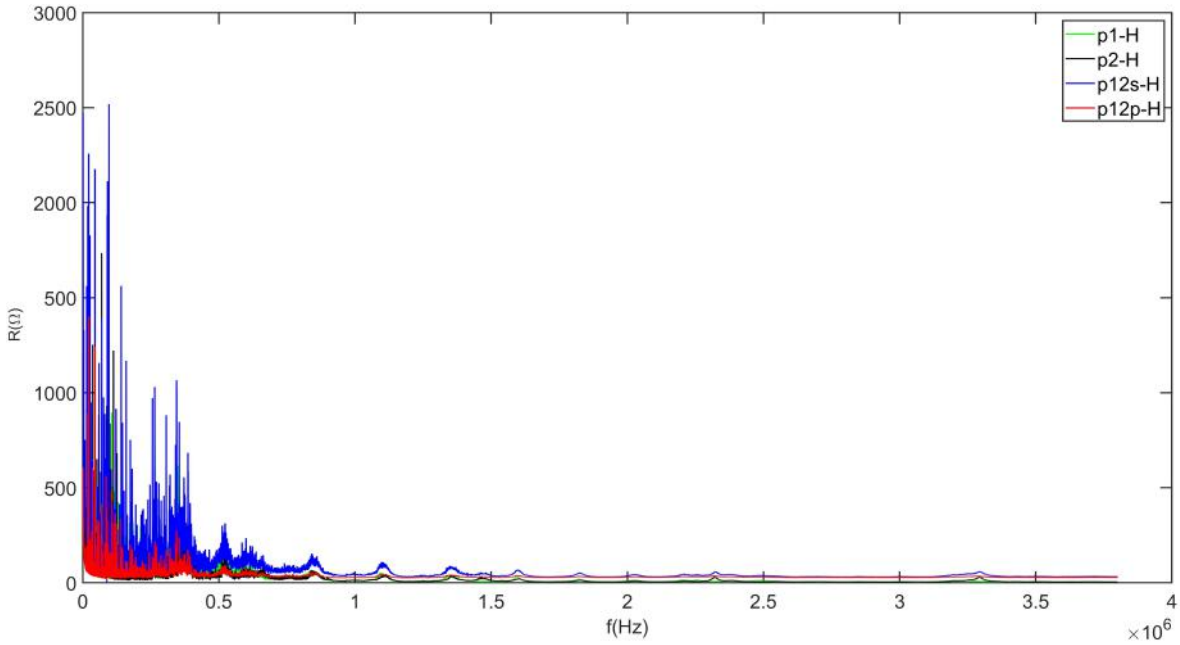

Fig. 2.5 The R spectrum plot of the p1, p2, p12p and p12s combinations in the healthy state.

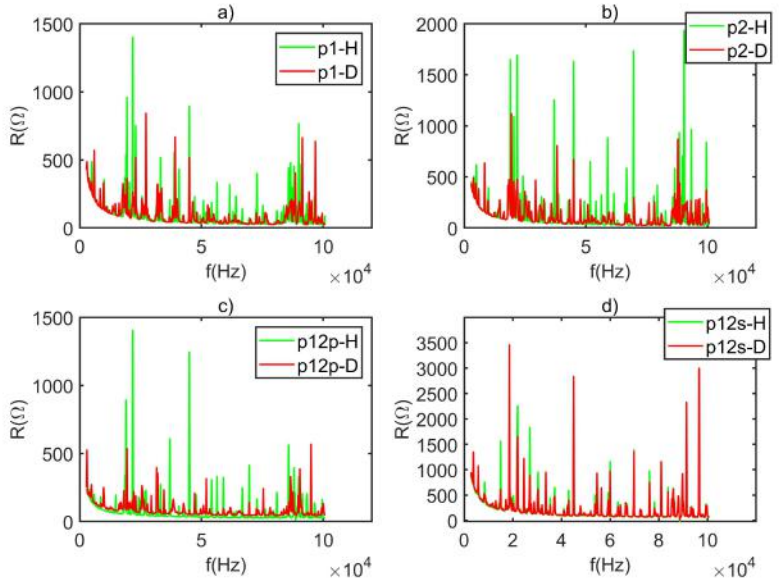

Fig. 2.6 The healthy and the damage R spectrum plot of the p1, p2, p12p, p12s combination for Fig. 2.3a damage arrangement.

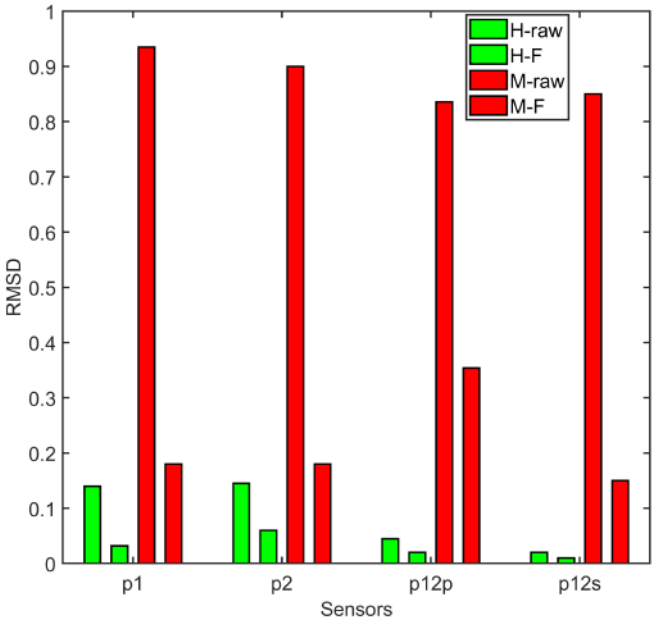

Fig. 2.7 The RMSD damage indices quantification of the R variable in different combinations of connection for raw and detrended filtered spectra in the damage case of Fig 2.3a.

for the cracked steel beam, respectively. Therefore, this range is suitable to demonstrate the suggested approach for damage detection.

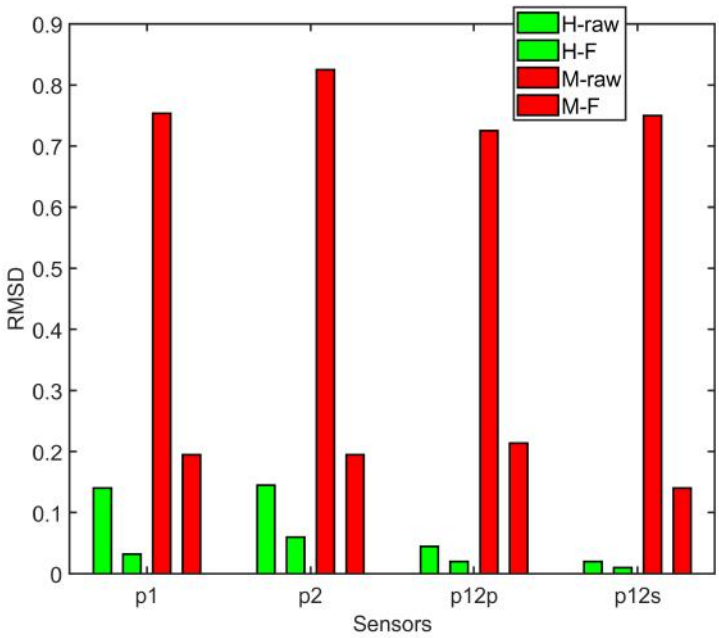

Fig. 2.8 The RMSD damage indices quantification of the R variable in different combinations of connection for raw and detrended filtered spectra in the damage case of Fig 2.3b.

The plot for the healthy and damage state spectrum of the p1, p2, p12p, and p12s are given in Fig. 2.6 for the simulated mass damage scenario for arrangement in Fig. 2.3a. The symbol 'H' and 'D' are used to demonstrate the healthy and damaged state (simulated mass M) of EMI measurements. Two repeated healthy state measurements were used to calculate the threshold (green bar) which reflects the uncertainties in the measurement. Using the RMSD damage index based on raw data, the p2 exhibits greater damage sensitivity than the p1, which goes against our expectations because the raw measurements had noise and contained a trend. Further, the calculation was done for detrended filtered data, and filtering was conducted using the Savitzky-Golay filter [103], while the detrending was made by removing the frequency dependence from the curves [104]. In a p12p combination, both raw (H-raw and M-raw) and detrend filtered (H-F and M-F) indices show significant damage sensitivity in comparison to a healthy state for the damage introduced in the steel beam structure. The p1, p2 and p12s also have shown damage sensitivity for the mass using raw and detrended filtered data-based damage index in the steel beam structure. According to Fig. 2.7, Fig. 2.8, and Fig. 2.9, the RMSD damage index demonstrates the damage sensitivity for all mass positions. In all damage cases, the damage was always discovered since the severity of the damage was always quite high and above healthy values for temperature kept constant at 19 $^{\circ}C$.

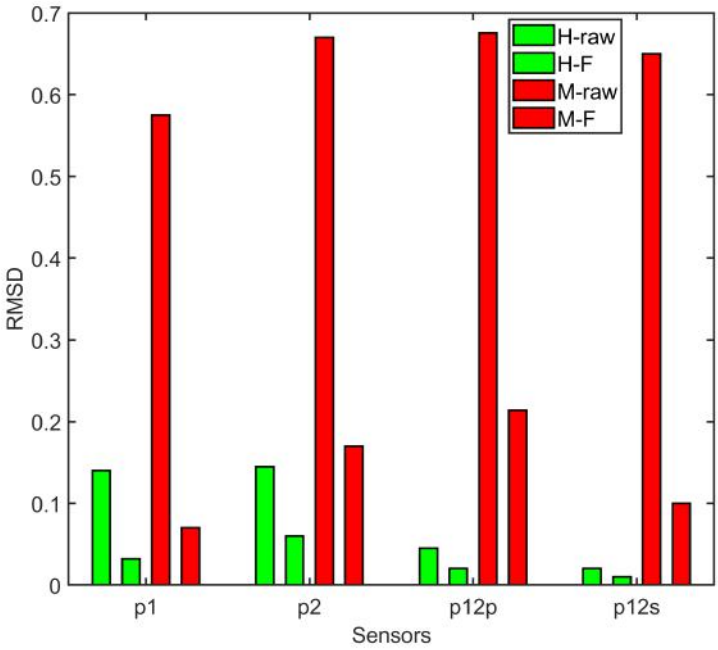

Fig. 2.9 The quantification of the R variable using the RMSD damage indices of various connections for the raw and detrended filtered spectra for damage case shown in Fig. 2.3c.

2.4 Robust damage detection in the varied environment temperature condition

This section is focused on extension of damage analysis using individual, series and parallel connection of the EMI electrode in the limited varying temperature conditions. The series and parallel combinations were studied and compared with the output of single sensors in the added small 5 gram simulated mass and created crack with variation of the environment temperature. The parallel connection has shown advantage over individual connections and series piezo connections in varying temperature environment condition while reducing the damage detection measurement time of the experiment. The simulated mass and cracked damage was successfully detected at higher baseline temperature in case of parallel combination of the piezo-actuator. Two cases made up the damage detection study. In the first case study, a simulated small mass is placed on the beam, and in the second, a crack forms on the beam under the temperature of the surroundings changes slightly.

2.4.1 Case I

Further, damage investigation was done for the small mass (5 grams) as shown in Fig. 2.3c as the large mass (50 grams) has more influence in the structure under varying temperature conditions. The damage sensitivity comparison was done for the healthy state of the steel bar at three temperatures: $19°C$, $23°C$, and $30°C$. H-19 stands for the healthy state at $19°C$, and other temperatures use similar nomenclature. The raw data for the experimental resistance value is compared to the varying limited temperature study for the behavior of the above combinations of the piezo-actuators. The results shown in the Fig. 2.10 represent the RMSD damage index for the raw data of the healthy and damage state data for the H-19, H-23, H-30, H-19/23, H-19/30, M-19, M-30 and M-19/30. The symbols used in the Fig. 2.10 are described in table 2.1.

Table 2.1 Healthy and damage symbols with their explanations.

Scenario	Description
H-19	Repeated two healthy state measurement at $19°C$
H-23	Repeated two healthy state measurement at $23°C$
H-30	Repeated two healthy state measurement at $30°C$
H-19/23	Healthy state measurement at $19°C$ wrt healthy state measurement at $23°C$
H-19/30	Healthy state measurement at $19°C$ wrt healthy state measurement $30°C$
M-19	Added mass state of the beam at $19°C$ wrt healthy state at $19°C$
M-30	Added mass state of the beam at $30°C$ wrt healthy state at $30°C$
M-19/30	Added mass state of the beam at $30°C$ wrt healthy state at $19°C$

The performance of parallel connection p12p dominates over the individual and series combination of piezo-actuators performance because of smaller resultant resistance amplitude and hence its lower sensitivity and precision towards noise and environment. The largest damage index differences for 5-gram mass are for the p12p in comparison to p1, p2, and p12s in varied healthy state temperatures: H-19, H-23, and H-30. Fig. 2.10 shows an increasing trend of the RMSD damage index for added mass with respect to the RMSD index for healthy states in varying temperature conditions of the p12p connection. Hence, the p12p connection-based damage indices are suitable for the detection of added mass damage and are less influenced by temperature variation. For the 5-gram simulated mass, the RMSD damage index does not exhibit the same increasing pattern for the individual sensors p1, p2, and the series connected p12s. The results show that it is enough to connect two sensors

in parallel and conduct the measurement instead of measuring two sensors individually for robust damage detection.

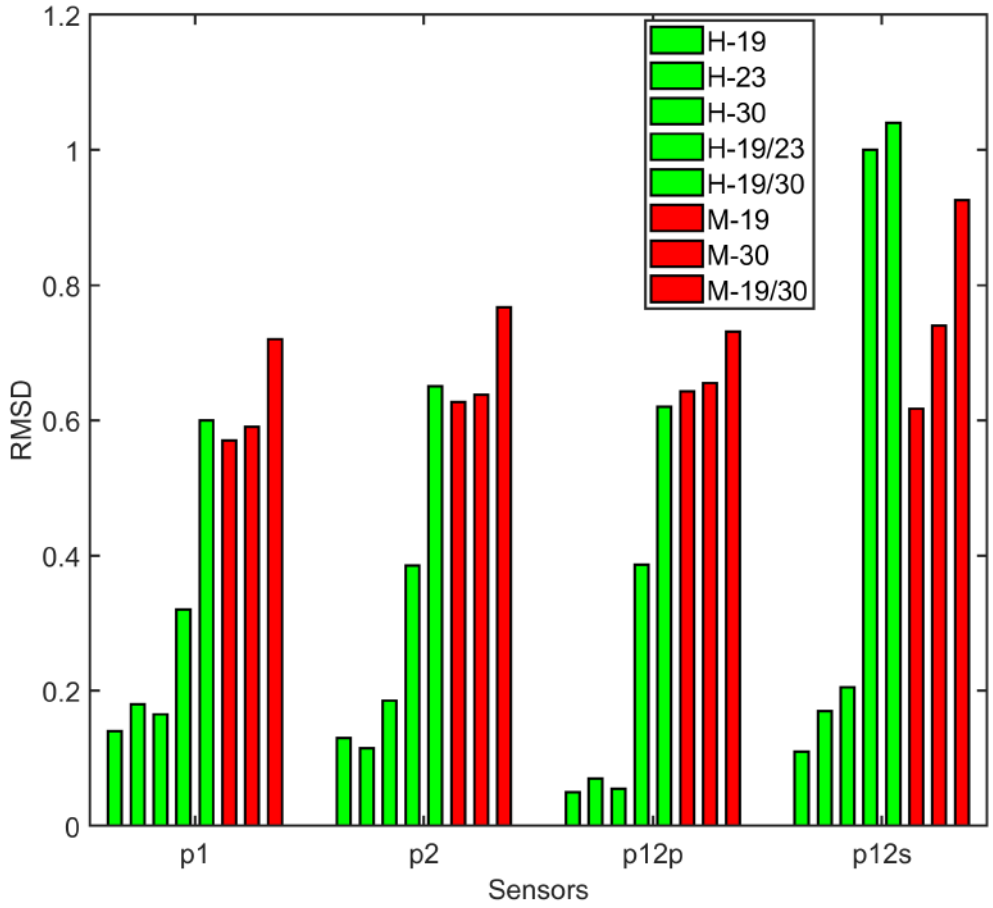

Fig. 2.10 The RMSD damage indices quantification of the R variable in different combinations of connection for raw spectra in the case of Fig 2.3c.

2.4.2 Case II

The temperature of the environment varied to investigate the most effective electrode connections under simulated crack at the end of the beam as shown in Fig. 2.2. The temperature of the environment increased from the $19°C$ to $24°C$ and further $31°C$ to investigate the sensitivity of damage in the varying environment conditions. The abbreviations used in the analysis of crack damage results are explained in the table 2.2.

The Fig. 2.11, Fig. 2.12, Fig. 2.13 and Fig. 2.14 have shown a comparative study of healthy and damage state of the beam experimental data for the p1, p2, p12p and p12s

Table 2.2 Created crack damage symbols with their explanations.

Scenario	Description
H19	Repeated two healthy state measurement at 19°C
H19-24	Healthy state measurement at 19°C wrt healthy state measurement at 24°C
H19-31	Healthy state measurement at 19°C wrt healthy state measurement 31°C
H24	Repeated two healthy state measurement at 24°C
H31	Repeated two healthy state measurement at 31°C
H24-31	Healthy state measurement at 24°C wrt healthy state measurement 31°C
Dc19	Damage state of the beam at 19°C wrt healthy state at 19°C
Dc24	Damage state of the beam at 24°C wrt healthy state at 19°C
Dc31	Damage state of the beam at 31°C wrt healthy state at 19°C
Dc19-24	Damage state of the beam at 19°C wrt healthy state at 24°C
Dc19-31	Damage state of the beam at 19°C wrt healthy state at 31°C
Dc24-31	Damage state of the beam at 24°C wrt healthy state at 31°C

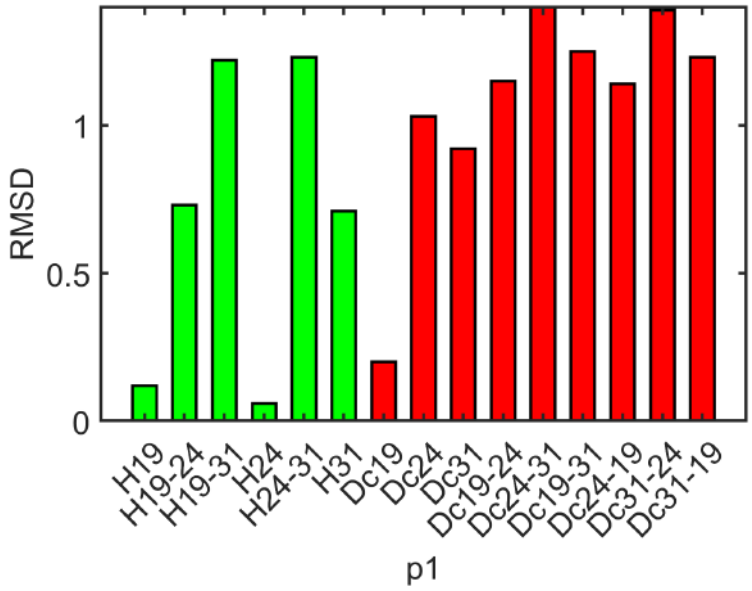

Fig. 2.11 The RMSD damage index quantification of the of p1 using R variable of beam.

connection. The green bar shows the different healthy state measurement and act as a threshold to monitor damage in the beam structure. The RMSD damage index of p12p in the cracked created condition shown by red bar is higher than green bar and irrespective of the healthy state measurement temperature as shown in Fig. 2.13. However, p1, p2

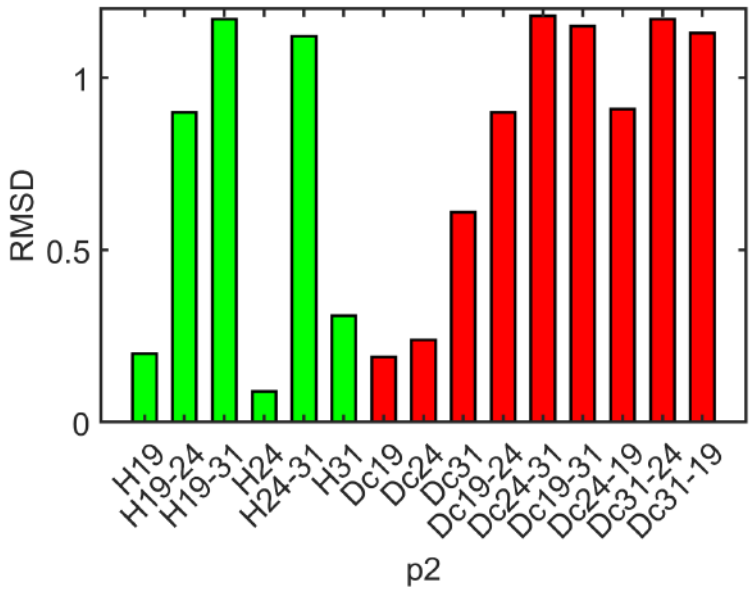

Fig. 2.12 The RMSD damage index quantification of the of p2 using R variable of beam.

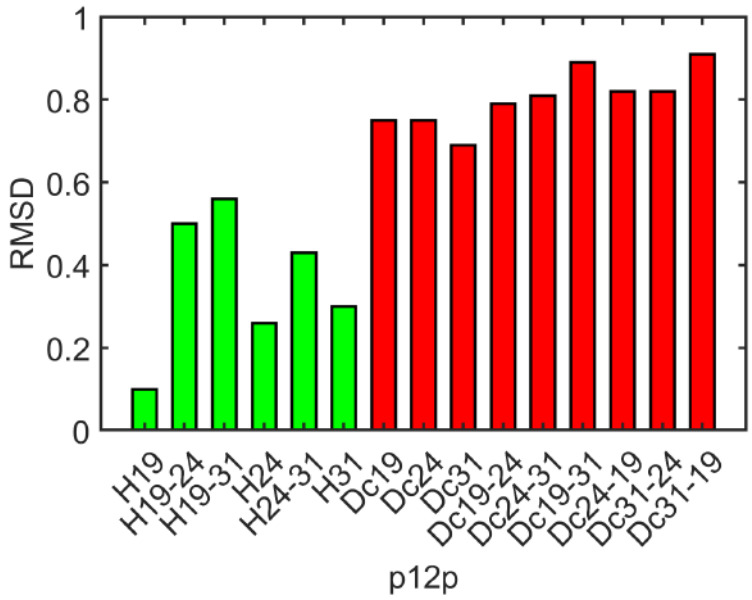

Fig. 2.13 The RMSD damage index quantification of the of p12p using R variable of beam.

and p12s are not showing such an increasing trend for the damage data irrespective of the healthy data variation in changing environment as shown in Fig. 2.11, Fig. 2.12, and Fig. 2.14 respectively. The RMSD performance of parallel connection p12p dominates over the individual piezo-actuator and series combination performance in the created crack condition. Hence, the p12p connection based damage indices are suitable for detection of the damage

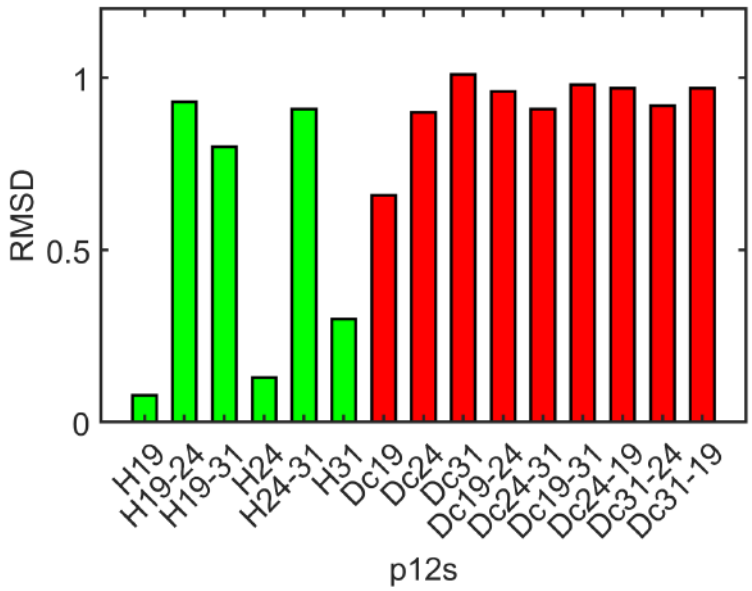

Fig. 2.14 The RMSD damage index quantification of the of p12s using R variable of beam.

steel beam and has less influence of the temperature variation. The parallel connection suppress resultant resistance amplitude and hence its lower sensitivity and precision towards noise and environment. Since the parallel connection is used for damage analysis using the healthy and damage state simultaneously. The damage index based study is less affected with the deviation in the damage signal caused by variation in the temperatures. When connecting the combined signal in parallel, the output external effect resistance is smaller; when connecting in series, it is larger.

In both case I and case II study, the damage was detected since the damage case DI are above the healthy case DI. Obviously there are differences in the absolute values but they do not cause any misinterpretation of the results. Hence, the p12p connection based damage indices are suitable for detection of the added mass and crack. Finally, this approach allows us time consumption reduction using the proposed connection for mass detection in varied temperature conditions. The following advantage and disadvantage parallel connections hold in compared to the individual connections 1. Faster measurement for the combined sensor measurement in comparison to the individual connections. 2. The p12p connections had shown the less sensitivity towards the temperature variation in comparison to the other individual and combined connections and always able to detect the damage. 3. The p12p connection shows the damage detection sensitivity for the small and big added mass as well simulated crack in the steel beam.

Chapter 3

Variable and sensor level data fusion based damage detection

3.1 Scope of study

This chapter discusses the range of variable-level and sensor-level data fusion approaches and how they might improve the performance of damage detection. The framework for data fusion is well established in other research fields of study, although data fusion for EMI is a recently popular approach. The goal of data fusion is to reduce uncertainty and create more effective representations by combining two or more data sets. There are three types of popular fusion approaches, data-level fusion, decision-level fusion, and feature-level fusion. Due to its ability to prevent the propagation and amplification of noise and measurement errors caused by post processing and to provide a higher signal to noise ratio, data level based data fusion enables pure data fusion [105–107]. The objective of the research is to offer a uniform, standardized method for determining structural damage. In order to increase damage detection through sound decision-making, data fusion enables information extraction from frequency domain data. A demonstration of the signature based on fusing G and R signatures for diverse experimental data is also provided for the effective EMI damage detection technique. Further, by utilizing each sensor's contribution to the damage index, a customized method based on PCA projections is employed to locate the damage.

3.2 Variables based data fusion

Although there has been a lot of effort done on data fusion, the EMI-based SHM technique only uses a few variable data fusion techniques. This section describes a data fusion technique

by combining the information for robust damage detection using the EMI method. To reliable damage detection using the EMI approach, the G and R values of sensors are studied in a selected frequency band, and a novel data fusion approach is explained. A novel fused parameter (F) is developed by combining the information from G and R. The F is expected to enhance the ability to identify damage because it magnifies the shared peaks of G and R. As a result, the indices based on the variable F should be more reliable for estimating damage and have a wider frequency range of application. The new damage metric under various damage situations is then measured using well-established indices such as RMSD, MAPD, and root mean square deviation for k^{th} damage state (RMSDk).

Researchers have only used one variable quantity thus far for EMI-based damage assessment, that too for a relatively narrow frequency range. For instance, Annamdas et al. [108] focused on G and limited themselves to range of 40-160 kHz, thereby limiting the examination of conductance curves to smaller ranges.

The better damage sensitivity of resistance was highlighted by Perera et al. [109] and Baptista et al. [110] for a specific frequency range, namely the 10-80 kHz range for the aluminum sample with the bolted connection and the 16-40 kHz range for the aluminum beam with damage modelled by increased mass. Na et al. [111] also applied the low frequency range of 10-80 kHz for resistance in carbon composites.

By combining the two variables in the proposed section, the variable's sensitivity is increased to a more intermediate sensitivity over a wider frequency range.

3.2.1 Experimental investigation of fused F

The piezoelectric Ceramtec transducers used for the EMI tests were disc-shaped, 0.5 mm thick, and 10 mm in diameter. They were built of the SONOX P502 material and are connected to an impedance analyzer. HIOKI IM 3570 impedance analyzer was utilized in the study to take measurements. The sensors are attached to the composite materials using cyanoacrylate adhesive on top of the sample surface. Using a chirp signal, 1V of excitation is selected as the excitation level for the experiments. The average of the 50 measurements is used for each measurement at a given time. The chosen damage location falls within the sensitivity of each structurally attached transducer. The findings of the damage detection were examined using the two structures:

1. The glass fibre reinforced polymer (GFRP) beam with delamination (Fig.3.1).
2. The GFRP plate with several impacts on its surface (Fig.3.2).

The first set of tests were conducted on a rectangular, thick composite beam of 500 mm $\times$ 95 mm $\times$ 3 mm, with a single piezoelectric transducer attached as shown in the Fig. 3.1. The

composite plate's EMI responses were recorded in its healthy state and three different stages of degradation with increasing delamination. The simulated delamination was introduced using the scalpel. Delamination has the following approximate dimensions:(S1) 10 mm $\times$ 5 mm, (S2) 20 mm $\times$ 10 mm, and (S3) 30 mm $\times$ 10 mm. Each delamination measurement stage was subjected to two measurements.

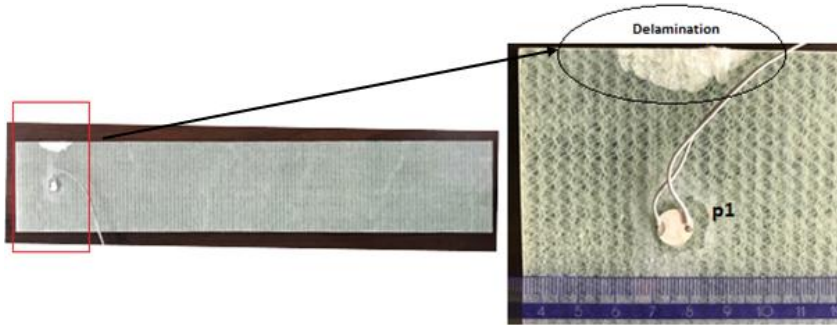

Fig. 3.1 Composite beam with enlarged view showing delaminated region (S3).

The second sample studied was a woven GFRP plate of the size 500 mm $\times$ 500 mm $\times$ 3 mm as shown in the Fig. 3.2. A projectile with a spherical end weighing a total of 1.3 kg was dropped from a height of 2.39 m onto the sample surface to create a single impact of 30 J of estimated energy. The table 3.1 lists the total number of impacts made on the sample as well as a description of the impact data on the surface of the GFRP sample. Even though there are four PZT sensors shown in the figure, only sensor P2's results are shown here. The other sensors were seen to be insensitive to damage being far from the damaged areas.

Table 3.1 Description of impact damage to the GFRP plate surface.

Scenario	Description
DS1	30J impact between P2 and P3 at a distance of 130 mm from P2
DS2	DS1 + 30J impact between P2 and P3 at a distance of 130 mm from P2
DS3	DS2 + 30J impact between P2 and P3 at 55 mm from P2
DS4	DS3 + 30J impact close to P2 at a distance of 25mm from P2

3.2.2 Theoretical implementation of the fused data F

This section of the chapter includes the methodology adopted for the **fused data F**. The EMI parameters of R and G have shown to be highly successful in many applications for detecting structural damage. The definitions of electrical impedance (Z) and admittance (Y) can be used to calculate the relationship between R and G, which is represented by Eq. 3.1 and 3.2.

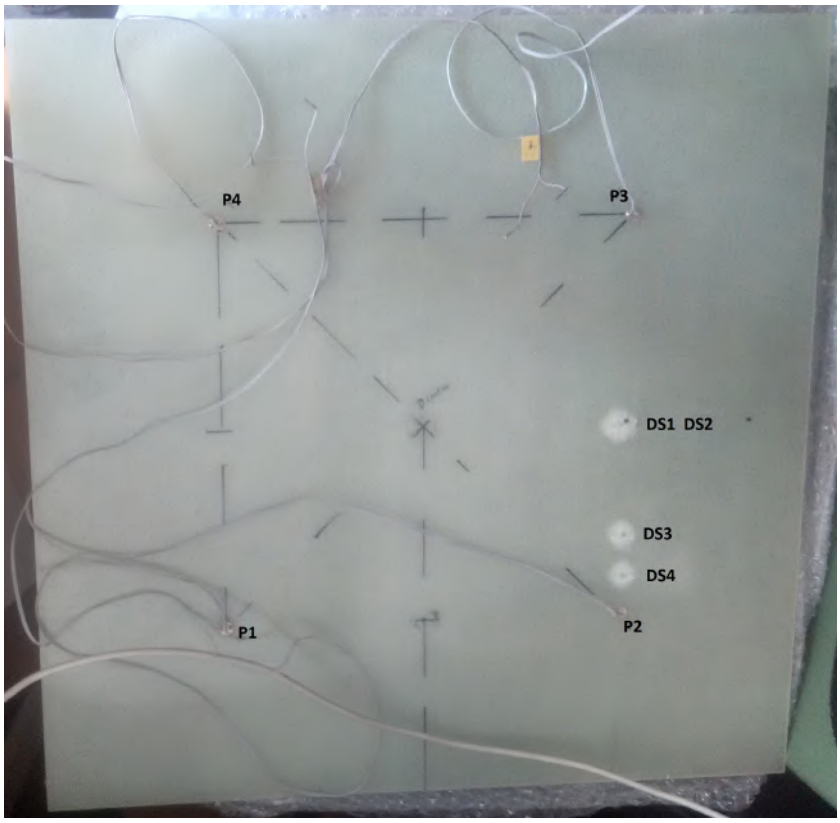

Fig. 3.2 The GFRP plate with impact locations.

$$Z = R + jX = \frac{1}{Y} = \frac{1}{(G + jB)} = \frac{1}{(G + jB)} \times \frac{(G - jB)}{(G - jB)} = \frac{(G - jB)}{(G^2 + B^2)} = \frac{(G - jB)}{[|Y|]^2} \tag{3.1}$$

where B is the susceptance of the system and X is the reactance. After comparing the real and imaginary parts of Eq. 3.2 the relation of R, G, B, and X can be established.

$$R = \frac{G}{G^2 + B^2};\ X = \frac{-B}{G^2 + B^2};\ G = \frac{R}{R^2 + X^2};\ B = \frac{-X}{R^2 + X^2} \tag{3.2}$$

We define a new fused non-dimensional parameter by multiplying G by R, which is a function of two values G and R, or G and B, or R and X, as illustrated in Eq. 3.3. For the purpose of detecting damage, this multiplicative dimensionless data may be employed.

$$F = G \times R = \frac{G^2}{G^2 + B^2} = \frac{R^2}{R^2 + X^2} \tag{3.3}$$

By multiplying the values by the normalized frequency for each measurement of R and dividing by the normalized frequency for each measurement of G, as indicated by Eq.3.4, the

measurements were detrended. The G, R, and F units are maintained via the aforementioned procedure.

$$G_{detrended} = \frac{G \times f_{max}}{f} \qquad R_{detrended} = \frac{R \times f}{f_{max}} \qquad F_{detrended} = \frac{F \times f_{max}}{f} \tag{3.4}$$

The rescaled spectra for G, R, and F for healthy and one damaged scenario are shown in Fig. 3.3. The variable F was rescaled between the frequency observed, as demonstrated in Fig. 3.3 for the healthy and damaged "S3" states. At the same time the F amplifies the common peaks in the G and R giving a higher contribution to these common peaks as shown in the square box of Fig. 3.3. As a result, the indices based on the variable 'F' are more reliable for estimating damage. The computation of F minimizes the effect of the non-dominant peaks which are often related to the measurement noise and other uncertainties. As we can see that the F spectra are smoother than the G and R spectra in Fig. 3.3. As the contribution of these uncertainties to the index for quantifying the difference is reduced, the F yields more stable results. However, it is interesting to mention here that the rescaling operation for variables was used before to simplify the investigation [104].

3.2.3 Comparative study of spectra using damage indices

The implementation of the new fusion signature for damage identification in two structures— a composite beam made of glass fiber reinforced polymer (GFRP) with escalating delamination and another GFRP plate with scenarios of impact-induced damage is shown in this section. A wide frequency range of 1 kHz to 100 kHz was covered for each of the these structures was examined and reported here to ensure consistency and allow for comparison. The RMSD and MAPD metrics, which are utilized in the EMI method as a damage-identification formula, are the most often used damage detection indices in EMI approaches. Eq. 1.4 is employed to determine the damage status on the basis of a comparison of the structure's healthy and damaged spectrums using EMI methods. With the use of RMSDk recently, damage detection performance has significantly increased [43]. This index is used to differentiate and evaluate the absolute variations of damage severity at each level. The main distinction between the RMSD and RMSDk is that the latter compares observed data with the previous state rather than the healthy state, while the latter is calculated using Eq.3.5.

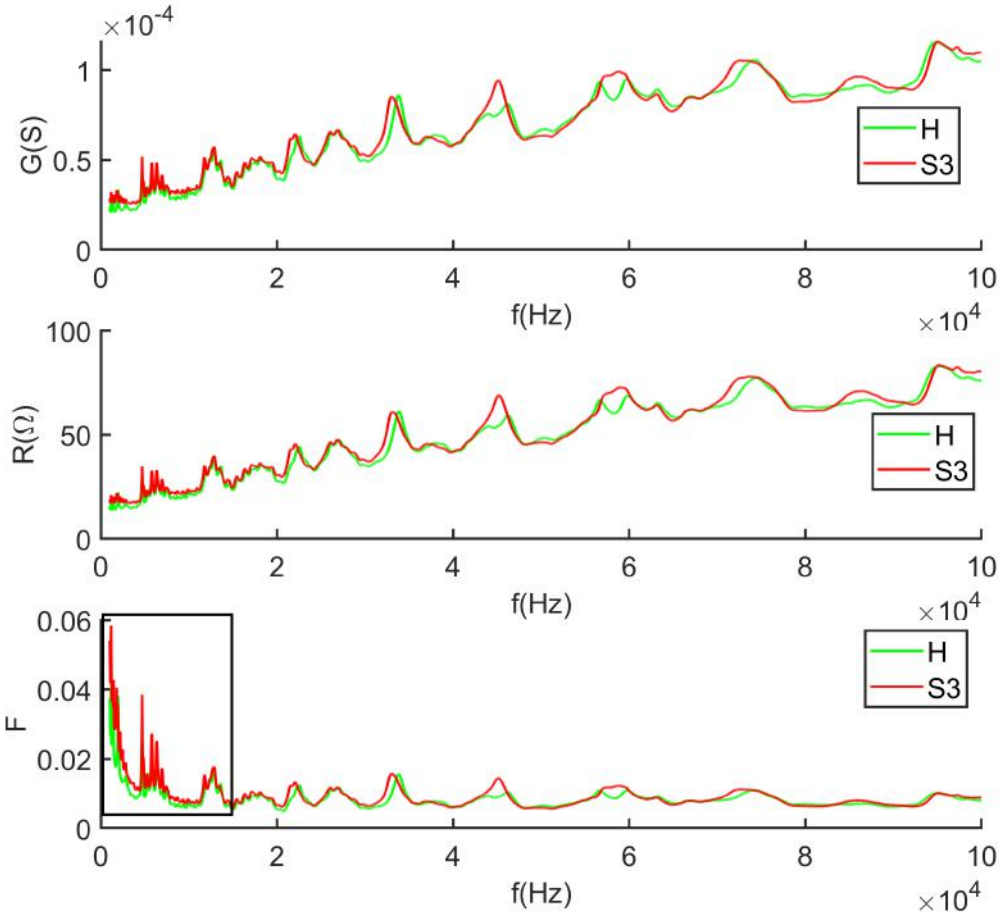

Fig. 3.3 Detrended spectrum of variables G, R and fused F.

$$RMSDk = \sqrt{\frac{\sum_{i=1}^{n}(D_i^k - D_i^{k-1})^2}{\sum_{i=1}^{n}(D_i^{k-1})^2}} \tag{3.5}$$

where symbol n is used for number of frequency spectrum samples, D_i^k is the i^{th} frequency sampling point for each k^{th} damage state.

Delamination analysis of composite beam

The similar peaks in the R and G spectra are increased in the F spectra, giving a stronger contribution to the damage quantification index. The RMSD index of the F, G, and R spectra were calculated for the measurements in the composite beam and shown in Fig. 3.4. it can be noted that all three of the damage measurement indices can be used to detect the

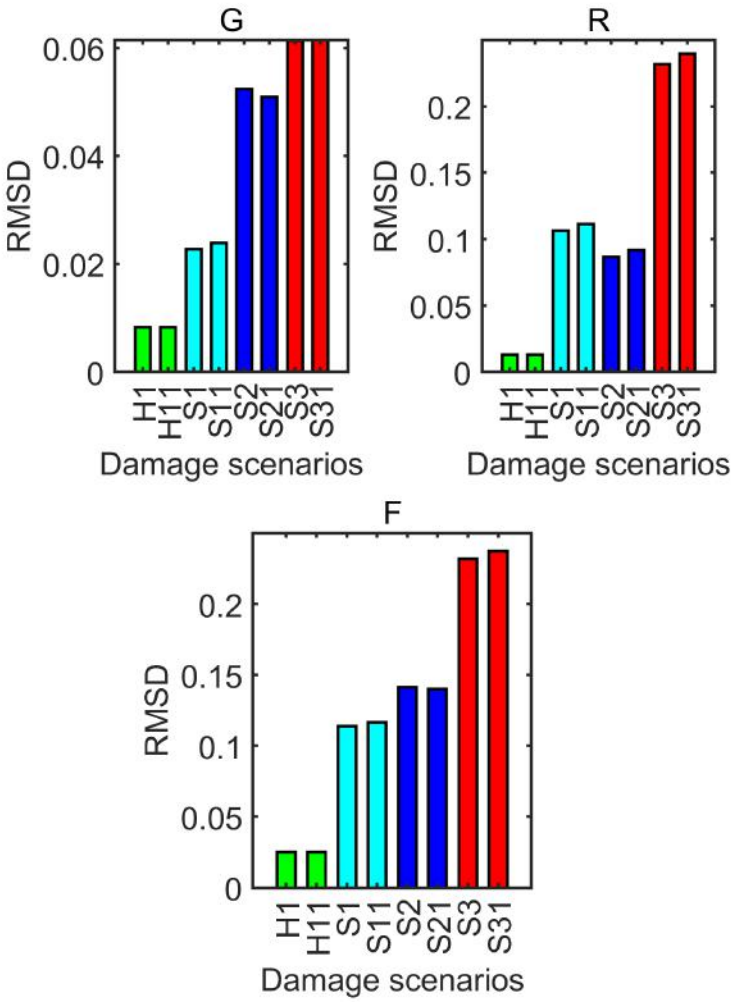

Fig. 3.4 The RMSD index of the variables G, R and F for GFRP beam.

damage. Results from the G and F but R based RMSD index exhibit an increasing trend of damage severity. The MAPD index of the F, G, and R spectra were calculated for the measurements that exhibit an increasing damage severity in the composite beam shown in Fig. 3.5. Additionally, F-based RMSDk exhibits a trend toward an increase in damage severity in the composite beam. Results from the G and R based RMSDk do not exhibit this trend as shown in Fig. 3.6.

Impact damage analysis of composite plate

The GFRP plate with impact-induced damage was the second structure that was examined. The Fig. 3.7 and Fig. 3.8 show the RMSD and MAPD damage index for G, R, and F respectively. It is evident that DS1 is not identified for all three indices under the damage

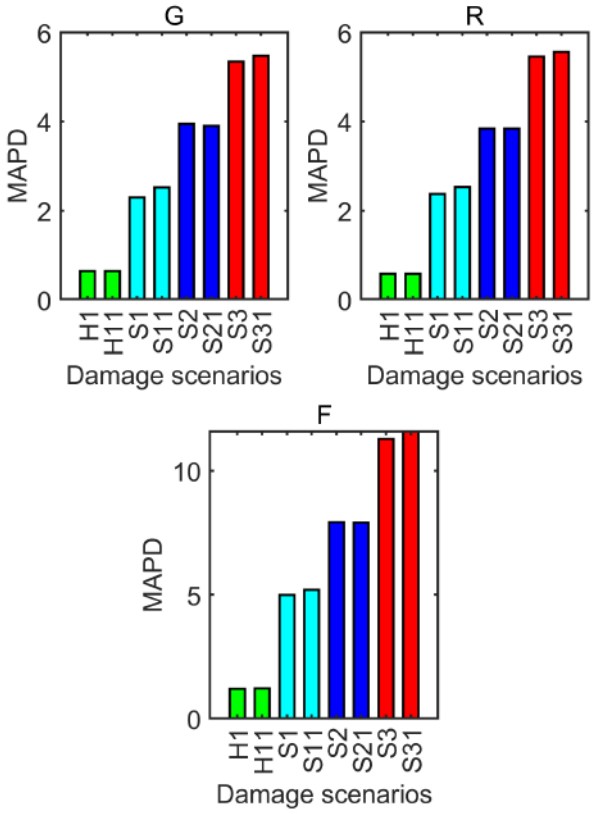

Fig. 3.5 The GFRP beam's MAPD damage index for the variables G, R, and F.

scenario. It is believed that the missed detection was caused by the fact that the first impact's damage to the structure was very minimal and far from the sensors. The three variables G, R and F successfully identify all other damage scenario. The variable F exhibits a greater difference than the G and R variables for cases DS2 and DS3, which suggests a stronger sensitivity to distinguish between damage of various magnitudes. The RMSDk damage index shown in Fig. 3.9 does not exhibit an trend for all G, R and F. The F metric is preferred to the G and R due to its increased sensitivity and capacity to distinguish various damage scenarios.

3.2.4 Summary

The table 3.2 provides a summary of the comparative damage index performance data shown in subsection 3.2. It is important to keep in mind that the performance of each variable depends on the index used for damage evaluation. As a result, given metric used for quantification, it is necessary to compare the performance of each variable. All three techniques for the GFRP beam exhibit a growing trend in the indices with rising damage. and it can be inferred that they perform satisfactorily as a result. For the GFRP plate, none

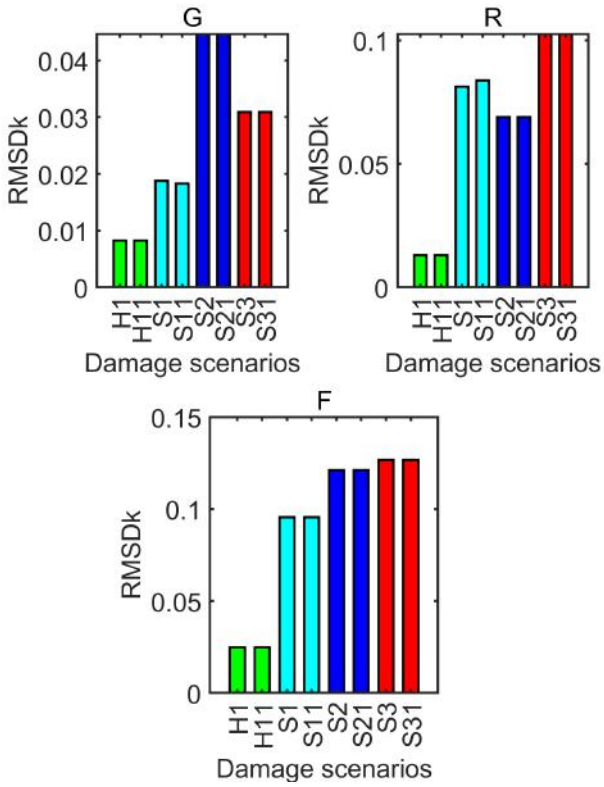

Fig. 3.6 The GFRP beam's RMSDk damage index for the variables G, R, and F.

of the three parameters with any of the three indices are able to detect the smallest damage, DS1. However, the F performs better than the G and R parameters for the other damage scenarios because it can discern between the increased damage between scenarios DS2 and DS3. None of the criteria for the RMSDk metric can identify the damage DS3 using scenario DS2 as the reference point. Therefore, it can be said that none of the parameters apply to this case. This flaw in the parameters can be linked to the RMSDk metric's failure rather than the parameters G, R, or F.

Table 3.2 Comparative performance study of G, R and F variable for GFRP beam and GFRP plate.

Samples	**RMSD**	**MAPD**	**RMSDk**
GFRP beam with delamination	G and F	F,G and R	F
GFRP plate with impact damage	F	G and F	none

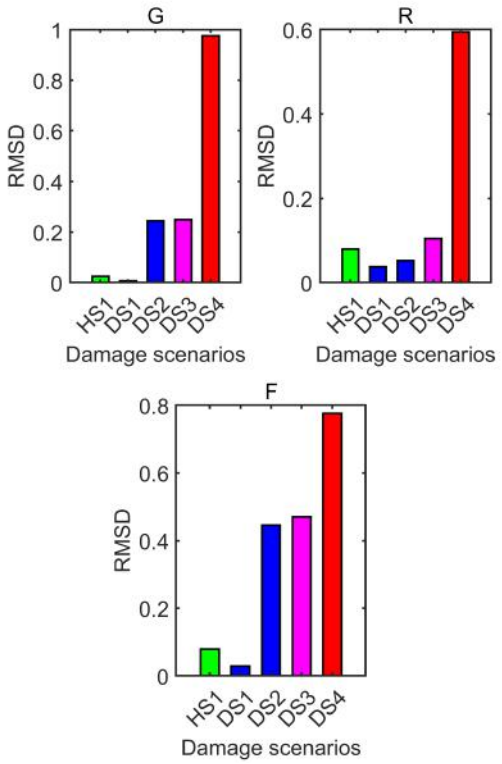

Fig. 3.7 The RMSD damage index for the GFRP plate's variables G, R, and F.

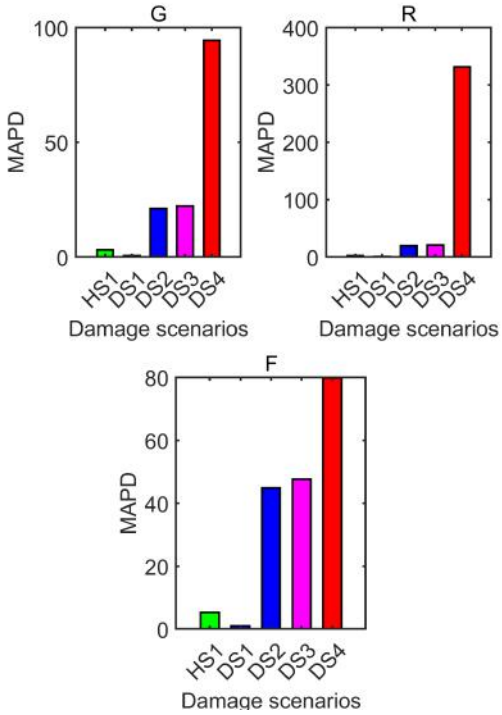

Fig. 3.8 The MAPD damage index for the GFRP plate's variables G, R, and F.

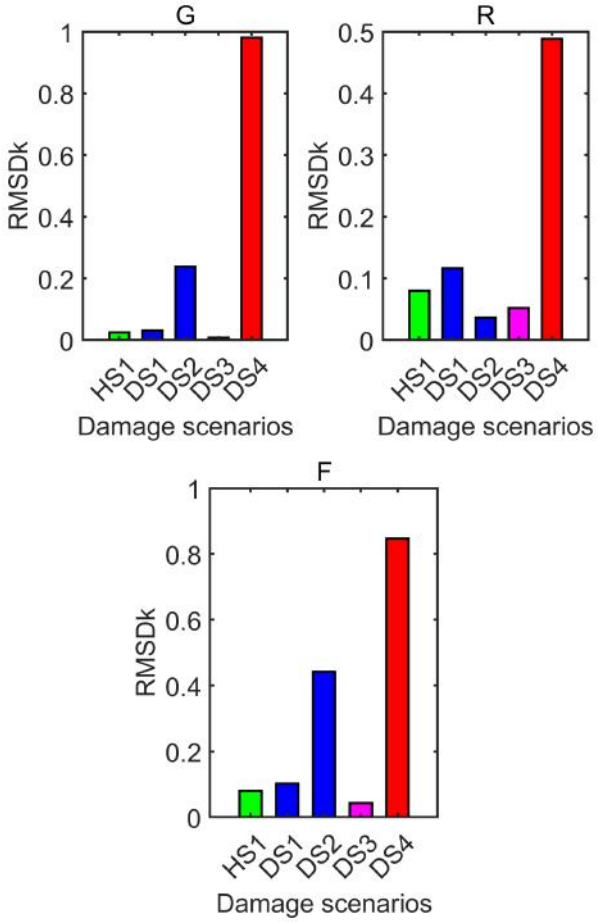

Fig. 3.9 The RMSDk index for the GFRP plate's variables G, R, and F.

3.3 Multi-level data fusion approach in damage detection

3.3.1 Introduction

This section proposes a new sensor network optimized data fusion approach for structural health monitoring of metallic structures using EMI signals. The classification of damage and undamaged health conditions of an aluminum plate with two holes is done using a new EMI-based data fusion approach for the sensor network that employs a damage detection algorithm and a statistical matching strategy.Data fusion makes it possible to extract information from frequency domain data to improve damage detection by making wise decisions. A modified method based on PCA projections is used to locate the damage using the contribution of each sensor to the RMSD index. Firstly, local data fusion (sensor data integration) that combines the data from four sensors is performed. Next, global data fusion (|Z|, |Y|, G and R from four sensors) that combines the frequency-domain features using self-organizing maps (SOM) is performed. SOM is an ANN technique based on the unsupervised algorithm for the classification of different states of the structure. By combining the variance contributions of PCA-based RMSD indices and feature level fusion, which are produced from four separate data variables (|Z|, |Y|, G and R) using SOM, the final assessment result is obtained. The optimized data fusion approach is proposed which was realized at the sensor level using the PCA as well as at the variable level using self-organizing maps (SOM) for the five damage instances of the drilled hole. In order to classify fusion-based data using SOM, statistical, data-driven damage matrices are computed, compared to the RMSD index, and employed. Regardless of the vast frequency range chosen, the approach exhibits robust damage sensitivity for hole sites and hole enlargement; nonetheless, the chosen frequency range contains the resonant frequency range.

The experiments were performed on a large thin square aluminum plate with attached piezo-actuators sensor network. Piezo-actuator placements are the outcome of a study using an optimization method for guided wave-based damage detection. This sensor network should only be used as an example of a distributed network for the EMI study since EMI-based damage detection was not a concern of the optimization. The study investigates the sensitivity of EMI responses to the drilled hole at different locations ‘D-a’ and ‘D-b’ in the aluminum plate. The room’s temperature was kept constant during the above experiment, and the aluminum plate’s dimensions were 100 x 100 x 0.1 cm^3. The EMI signatures at the piezo-actuator terminals were measured using an Impedance Analyzer by HIOKI, model number IM3570. The ’D-a’ position was first drilled to create a 5 mm diameter hole, which was then enlarged to an 8 mm and finally a 10 mm diameter, as shown in Fig. 3.10. After introducing the 10 mm hole at location D-a, a 5 mm of hole was drilled at new location (D-b).

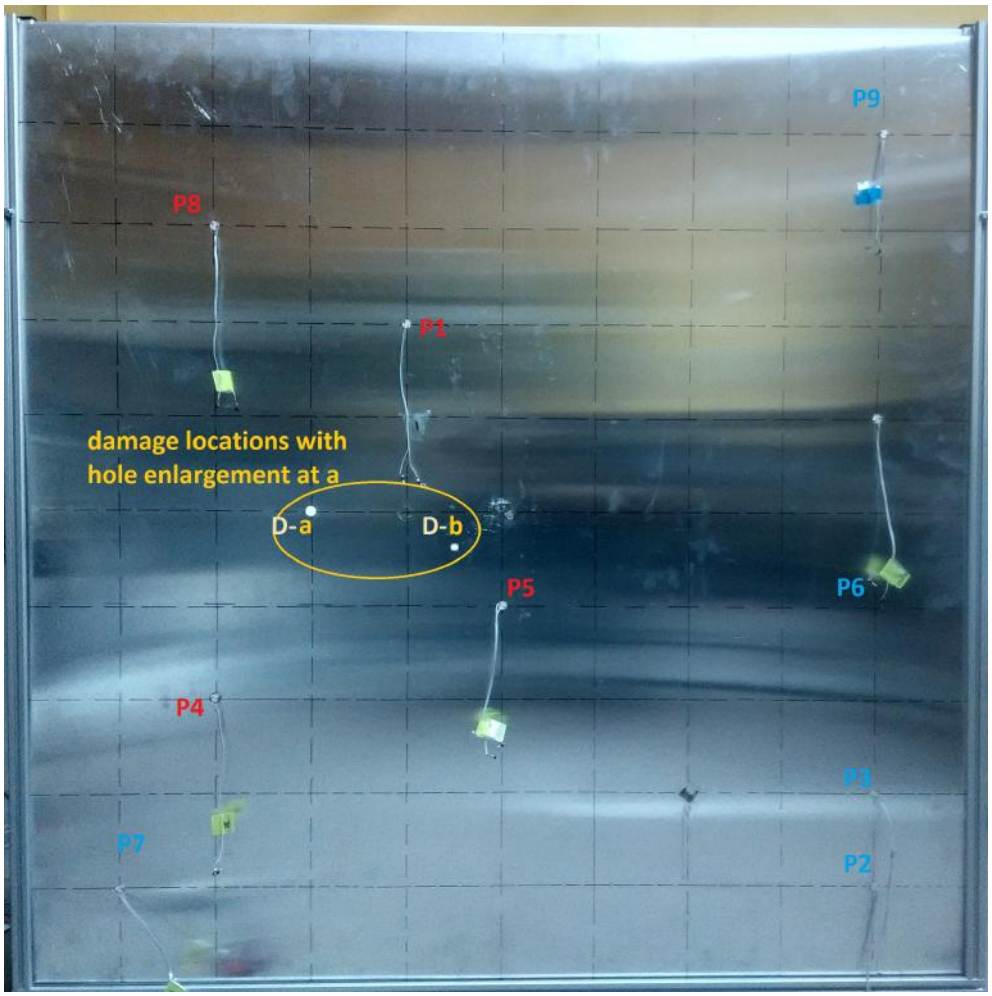

Fig. 3.10 Sensor network distribution against the damage locations in the sample plate.

3.3.2 Data driven methodology based on PCA and SOM

The four sensors were employed in the EMI data fusion demonstration at several levels to examine the structural damage. Firstly, the data level fusion is by combining the raw data (|Y|, |Z|, G, and R) utilizing a variance contribution of the PCs of the sensor network. Secondly, feature-level fusion has performed as a heterogeneous (|Y|, |Z|, G, and R from four sensors) input of statistical indices in SOM. In this approach, a healthy structure's baseline eigenvector is generated using fused data, and then the damage responses are projected onto this model. Statistical features of signatures are extracted from the original raw data using PCA based damage indices, and these features are concatenated prior to the decision level SOM and effective RMSD fusion. PCA provides further opportunities for damage classification using statistical Q index , and T^2 index. The SOM comparative studies are performed using the Q-statistics (Q index) and the Hotelling's T^2 statistic. A data fusion based general framework

of the adopted methodology in damage classification of an aluminium plate using a sensor network is given in the Fig. 3.11.

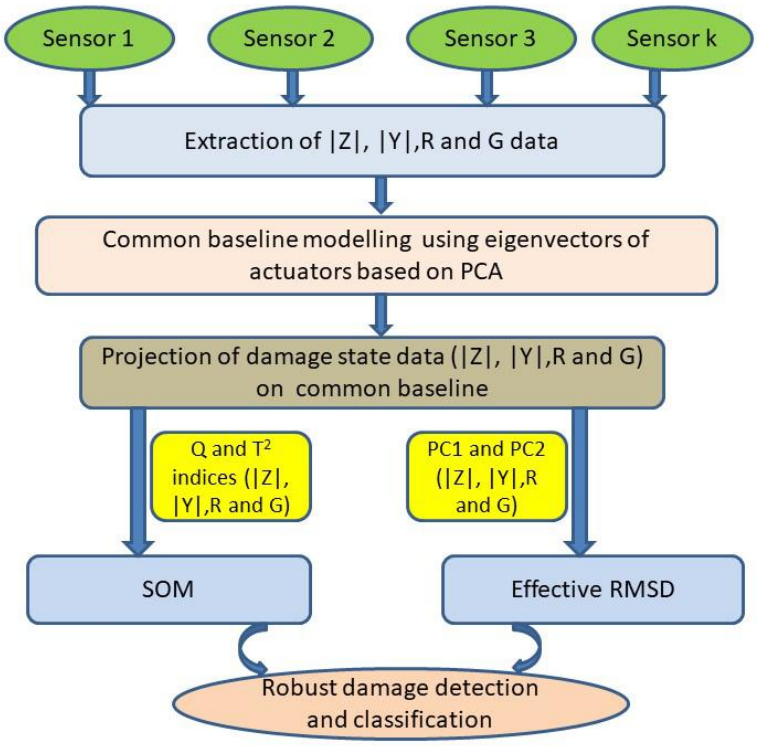

Fig. 3.11 a framework for the methodology used to classify damage.

The sensor network variables |Z|, |Y|, G, and R have various magnitudes and scales that can be scaled using the mean and standard deviation. Using the formula in Eq. 3.6, the normalization process has been carried out according to conventional practice.

$$D1_{ij} = \frac{D_{ij} - \mu_i}{\sigma_i} \tag{3.6}$$

where D_{ij} represents j^{th} sample for the i^{th} sensor, μ_i is mean of D_{ij} , σ_i is the standard deviation of D_{ij}. The PCA-based baseline model can be created by organizing the data into an J×I matrix, D1 being the data set's normalized matrix, and including information (|Y|, |Z|, G and R) from the various sensors (I) of the sensor network. The PCA is used to compute the covariance matrix of the data, eigenvalues, eigenvectors and combine the data from different piezo-actuators. The components are organized in descending order of variance contribution. Using Eq. 3.7, it is possible to construct the covariance matrix of the normalized data matrix [112].

$$C_d = \mathbf{D1}^T D1 \tag{3.7}$$

This covariance matrix has an I×I dimension and measures the degree of linear relationship among all variables. If V contains the eigenvectors of the covariance matrix C_d, P is the damage state data matrix and T is a damage score matrix which represents the projection of damage data set in the direction of V and given by Eq. 3.8.

$$T = PV \tag{3.8}$$

The PCA-based damage detection indices are the **Q index and Hotelling's T^2 index** used in this thesis for the first time in the EMI application. The former uses the residual subspace to examine the variability of projected data, while the latter, the new principal component space [75, 76]. If $\hat{I}$ is the identity matrix, x is the corresponding piezo-actuator variable e.g. |Y|, |Z|, G and R, x^T is the transpose matrix of x, P_1 are the reduced eigenvectors, P_1^T is the transpose matrix of P_1 and $\wedge$ is the eigenvalues based diagonal matrix, then statistical indices can be calculated using Eq. 3.9 and Eq. 3.10.

$$Q = \mathbf{x}^T(\hat{I} - P_1 P_1^T)x \tag{3.9}$$

$$T^2 = \mathbf{x}^T(P_1 \wedge^{-1} P_1^T)x \tag{3.10}$$

Using the mixing weight matrix, the derived damage indices (Q index and T^2 index) from the PCA technique were combined to form a condensed artificial neural network (ANN). SOM is a collection of nodes connected by weight-based inputs. These nodes are often connected using rectangular or hexagonal topology. The winning neuron is determined by the similarity between the weight w_{ij} and the input variables $(x1, x2)$. The SOM algorithm is based on the smallest Euclidian distances $d(x_j, w_{ij})$ between each neuron and the input variables, as given by the Eq. 3.11 [113].

$$d(x_j, w_{ij}) = \sqrt{\sum_{i=1}^{n}(x_j - w_{ij})^2} \tag{3.11}$$

SOM is a potential tool for clustering and visualizing high-dimensional data due to their unique differentiation strategies for different characteristics based on the internal representation of input signals [113, 114]. The input layer neurons are fully connected to the output neurons of the Kohonen layer for the strongest response using the weight matrix. Eq. 3.12 provides the relationships between the weight matrix and input x_{ij}.

$$Output_j = \sum_i (w_{ij} x_{ij}) \tag{3.12}$$

The winner in the Kohonen layer is given by Eq. 3.13 for the k^{th} iteration

$$w_{ij}(k+1) = w_{ij}(k) + \varepsilon(x_j - w_{ij}) \tag{3.13}$$

where, ε is learning rate, w_{ij} is the weighting factor between the i^{th} neuron of the input layer and j^{th} neuron of the Kohonen layer and x_{ij} is the input signal of the network in the form of Q and T^2 index.

The two-dimensional rectangle topology is shown in Fig. 3.12 which presents SOM for the input and Kohonen layer employing neurons. For the two inputs, x_{ij} (x1 and x2) is the combination of the variables |Z|, R and |Y|, G using the Q index and T^2 index, respectively. SOM is performed on the Q index and T^2 index based damage score to classify the damage state of the structure using a Kohonen SOM toolbox of Matlab [115].

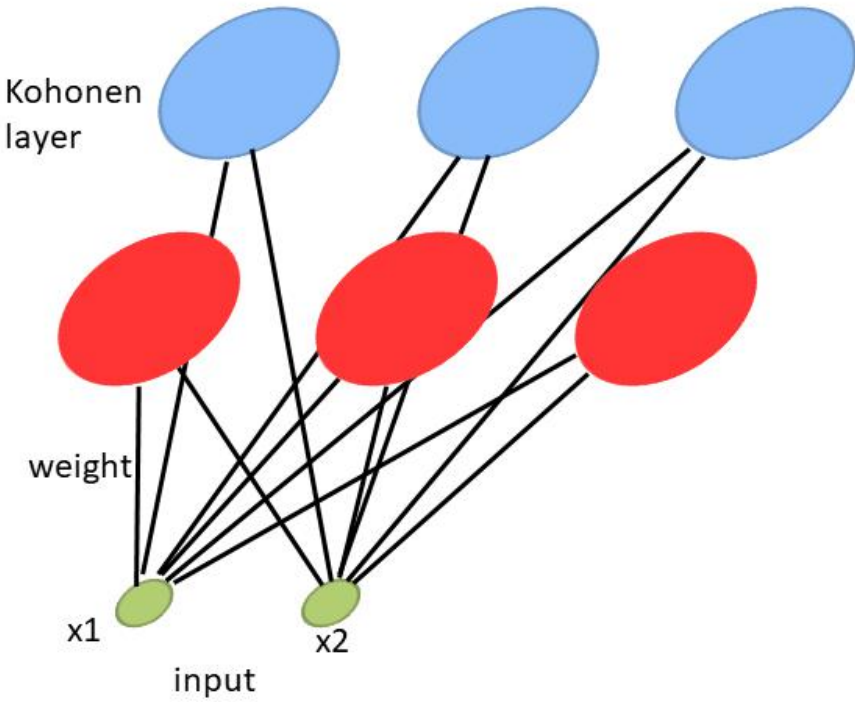

Fig. 3.12 A framework of the two dimensional rectangular topology based SOM in classification.

3.3.3 Results and implementation of the damage detection

Fig. 3.13 displays the sensor network conductance spectra for the aluminum plate in both its healthy and damaged states for piezo-actuators P1, P4, and P5 which are equally spaced from the hole and P8 that is farther apart. The 17–600 kHz frequency range is suitable to illustrate the method for all variables for damage identification and classification, according to the prescreening of the EMI signatures. The peaks of G lied in the narrow frequency range (180-250 kHz) and are also included in this selected wide frequency range. Consequently, the technique is tested in both wide (17-600 kHz) and narrow (180-250 kHz) frequency bands. Eq. 1.4 was used to obtain the RMSD damage indices for these piezo-actuators at various damage severity levels (5 mm, 8 mm, and 10 mm holes).

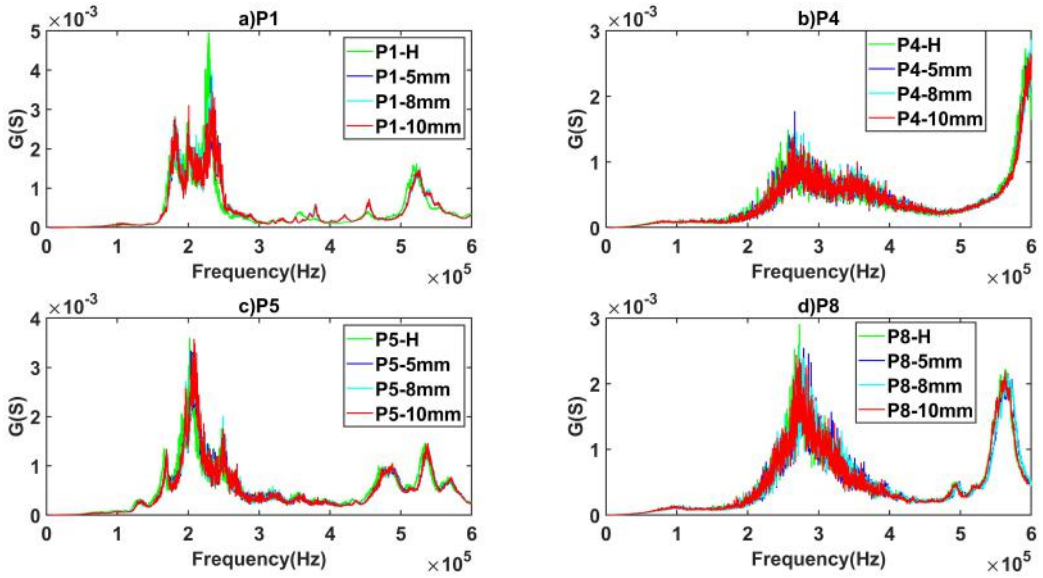

Fig. 3.13 Sensor network G spectra for piezo-actuator (a) P1, (b) P4, (c) P5, and (d) P8 in both the healthy and damaged states.

Fig. 3.14 and Fig. 3.15 provide the RMSD damage index for the wide frequency range of 17-600 kHz and the narrow frequency range of 180-250 kHz, respectively. According to Fig. 3.14, the piezo actuator P1 has demonstrated the highest RMSD index for all features (|Z|, |Y|, G, and R). The piezo-actuator P5 has demonstrated extraordinary behavior and is less sensitive than P8 for the variables |Z| and |Y|. It has the second-highest sensitivity for the variables R and G. It is also clear from the bar plot that the RMSD index is not increasing with damage severity across all sensor's variables. In addition, compared to their performance in the wide frequency range, the piezo actuator's performance for damage sensitivity is subpar in the restricted narrow frequency range (Fig. 3.15). There are several instances when the RMSD values for 8 mm and 10 mm hole damage cases are lower than for 5 mm hole damage

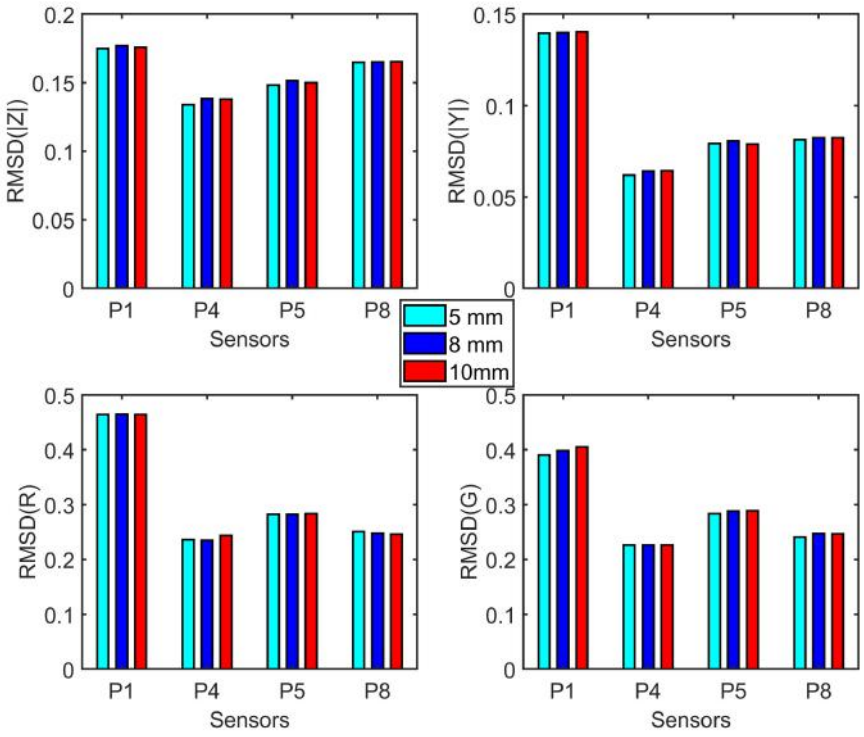

Fig. 3.14 Sensor network RMSD damage indices of 5 mm, 8mm and 10 mm hole drilled at 'D-a' location for the |Z|, |Y|, R and G in the wider frequency range 17-600 kHz.

situations. In both the narrow and wide frequency ranges, the RMSD for the 10 mm hole damage scenario is not necessarily higher than for the 8 mm hole damage case. In conclusion, it is clear that the damage severity cannot be determined for both frequency ranges using the RMSD index.

In order to classify fusion-based data using SOM, statistical, data-driven damage matrices are computed, compared to the RMSD index, and employed. All of these variables (|Z|, |Y|, G and R from four sensors) were examined using a principal component contribution-based technique. The 1^{st} principal component was utilized for damage analysis since it contains the majority of the data variation. To create the healthy state baseline model for four piezo actuators, the data from the healthy state is properly trained from the 10 experiments of each piezo actuator. To generate the baseline PCA model, these data are structured into a high-dimensional space matrix (J×I). After normalizing the projection of damage state data onto the baseline model, the RMSD calculation is performed. The Fig. 3.16 displays the reconstructed conductance spectrum plot for P1, P4, P5, and P8 using the first PC, which is utilized to determine the RMSD index in the frequency range of 17-600 kHz.

The RMSD index for PC1 of projected data was determined using Eq. 1.4. The 1^{st} principal component-based RMSD indices for the P1, P4, P5, and P8 for the |Z|, |Y|, G, and

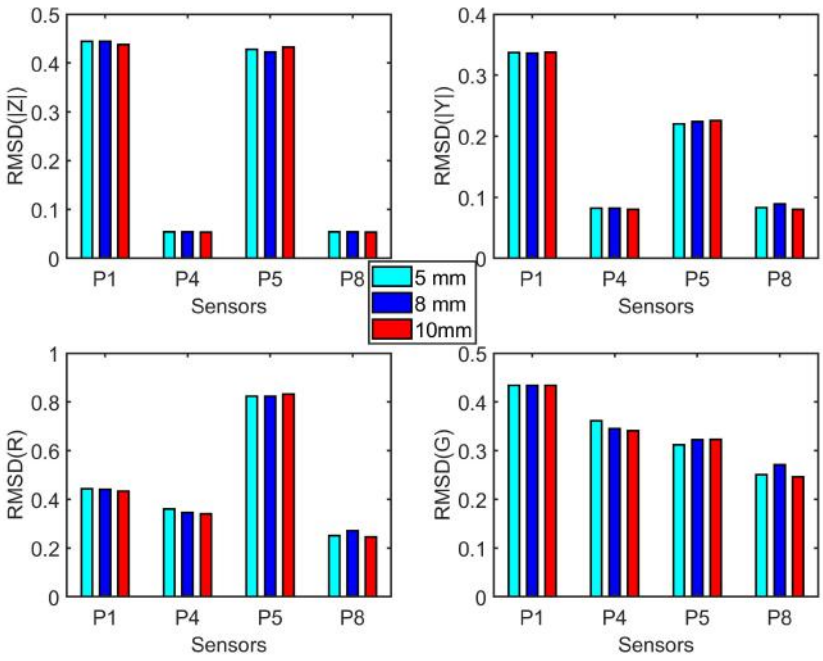

Fig. 3.15 Sensor network RMSD damage indices of 5 mm, 8mm and 10 mm hole drilled at 'D-a' location for the |Z|, |Y|, R and G in the narrow frequency range 180-250 kHz.

.

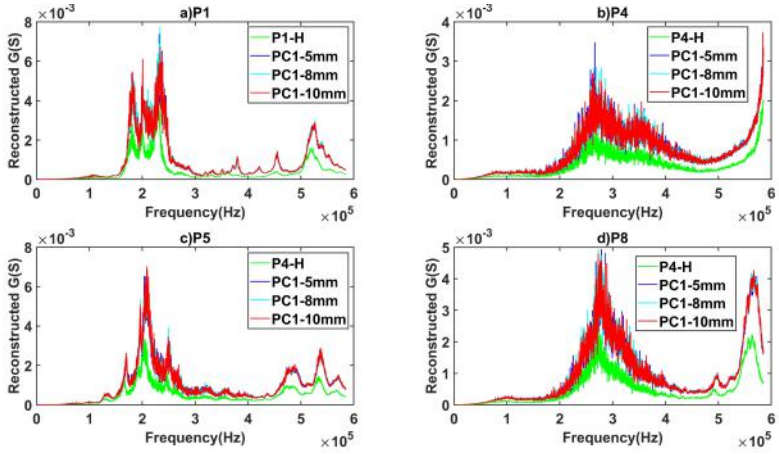

Fig. 3.16 The PC1 based reconstructed conductance spectrum plot for the sensors (a) P1, (b) P4, (c) P5 and (d) P8.

R variables are shown in Fig. 3.17. The first PCA-based RMSD index for piezo actuator P1 demonstrates the highest level of damage sensitivity due to higher index values in each case. P5 exhibits more sensitivity than P8 for all the variables in the instance of an 8mm hole based on the 1^{st} PCA RMSD damage indices, proving that P8 is farther away from P5. In contrast to the RMSD that displays reduced values of P5 for |Z| and |Y|, the R based PCA RMSD of

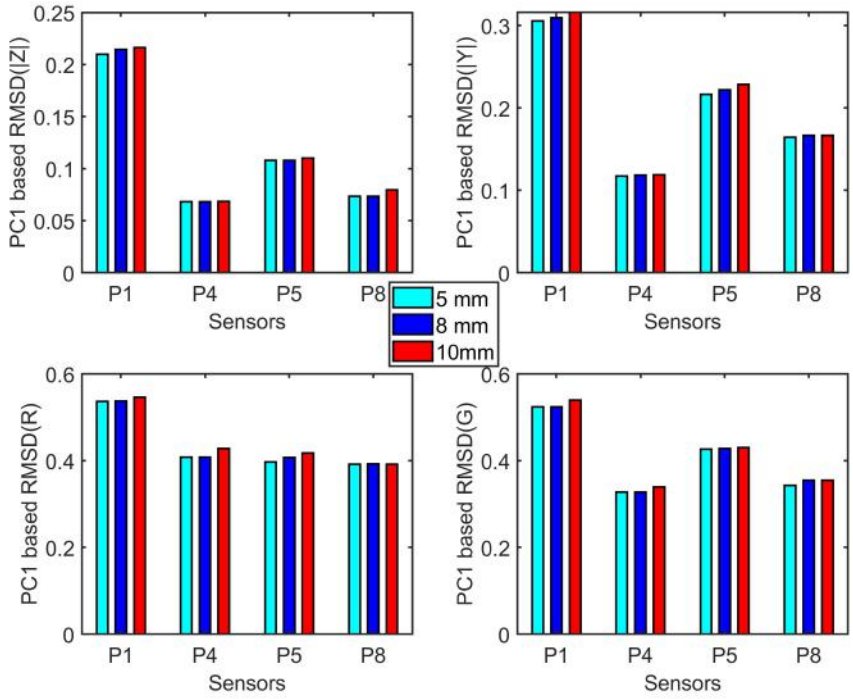

Fig. 3.17 RMSD damage index for the variables |Z|, |Y|, R, and G in the wide frequency range of 17-600 kHz for the drill holes of 5 mm, 8 mm, and 10 mm based on the first PC.

P5 is nearly smaller than P8 for a 5 mm hole. However, P1, P4, and P5 PCA RMSD have demonstrated superior sensitivity than P8 in the resonance frequency region, as seen by the high index value and rising damage severity trend in Fig. 3.18, as opposed to RMSD, as depicted in Fig. 3.15.

Further, to identify the damage in a wider frequency range (17-600 kHz), a principal component's variance contribution based method was also examined for the P1. This method offers flexibility for data fusion using PC1, PC2, and other variance contribution-based PCs in the effective RMSD index. The Fig. 3.19 shows the variance with respect to principal components to the variable |Z|, |Y|, G and R in the baseline model of the sensor network. |Z| and |Y| account for the majority of the variance contribution to the PC1. However, as illustrated in the Fig. 3.19, PC2 cannot be disregarded for the R and G variables for damage detection. The general algorithm used to calculate effective RMSD is given by Eq 3.14.

$$RMSD_{effective} = w_1 RMSD_{PC1} + w_2 RMSD_{PC2} + ... + w_n RMSD_{PCn} \tag{3.14}$$

Where w_1, w_2 and w_n are variance contribution of corresponding principal components; $RMSD_{PC2}$, $RMSD_{PC2}$ and $RMSD_{PCn}$ are the RMSD values based on the 1^{st}, 2^{nd} and n^{th} principal components of projected damage data with respect to the healthy state.

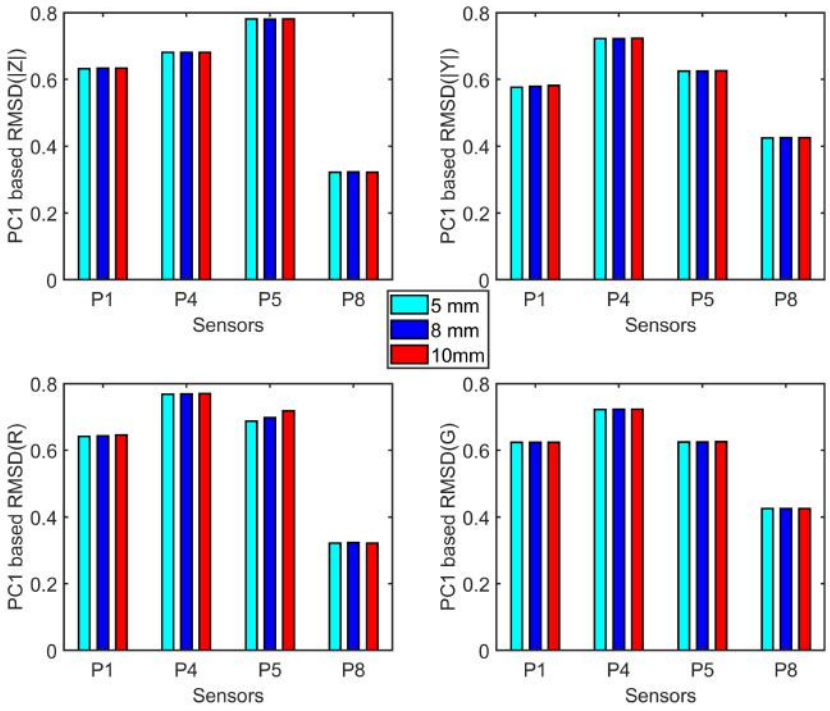

Fig. 3.18 RMSD based on 1st PC for the variables |Z|, |Y|, R, and G in the specific frequency range of 180-250 kHz for drill holes of 5 mm, 8 mm, and 10 mm.

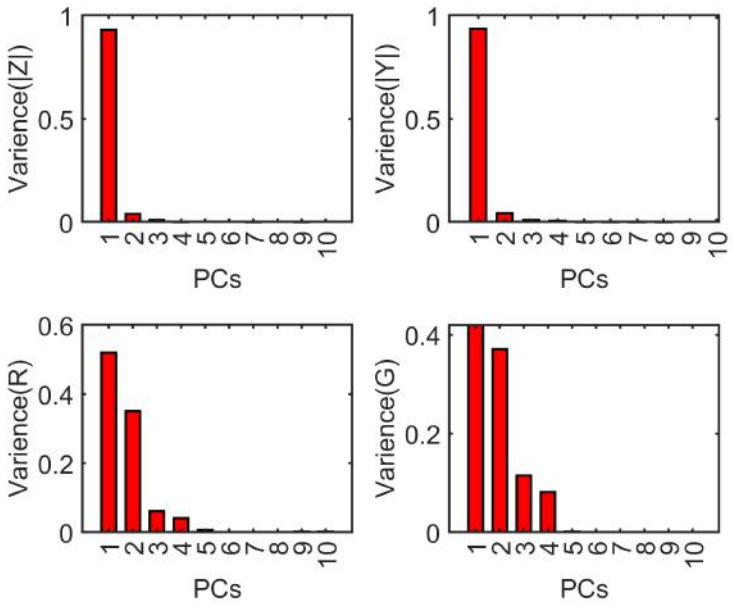

Fig. 3.19 Variance contribution of the sensor network for the 17-600 kHz large aluminum plate EMI variables |Z|, |Y|, R, and G.

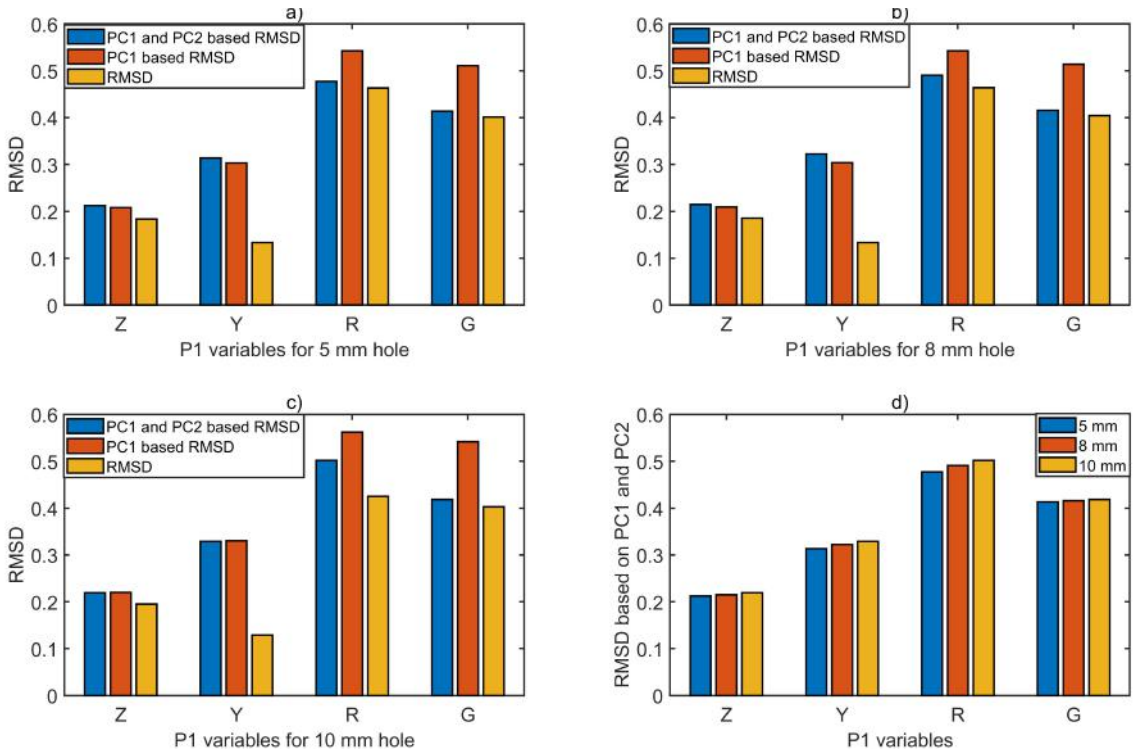

Fig. 3.20 An evaluation of traditional RMSD fused RMSD based on PCA utilizing PC1, PC1 and PC2 (a) 5 mm hole, (b) 8 mm hole, (c) 10 mm hole, and (d) Fused PC1 and PC2 RMSD for 5 mm, 8 mm, and 10 mm hole for P1.

Fig. 3.20 depicts the most sensitive piezo actuator P1 damage scenario (5mm, 8mm, and 10mm diameter hole). The effective RMSD index combines 1^{st} PC and 2^{nd} PCA as opposed to standard RMSD and 1^{st} PCA RMSD. For the variables |Y|, |Z|, G, and R, utilizing PCA has a greater scale for RMSD than using standard RMSD. Effective RMSD (using PC1 and PC2) used to quantify the severity of damage has showed a rising trend for 5 mm, 8 mm, and 10 mm diameter holes shown in Fig. 3.20.

Using the PC1 based RMSD of the common baseline healthy state model indicated above in approach, the second damage position (hole at "D-b") is identified. The Fig. 3.21 displays the PC1 RMSD of the P1, P4, P5, and P8 for all variables |Z|, |Y|, G, and R. The P5 has the maximum sensitivity in this investigation, indicating that it is located closest to the site of damage (D-b). P8 exhibits the lowest sensitivity in the all cases in compared to P1, P4, and P5.

The study's scope for damage classification and detection utilizing data fusion was expanded by the addition of PCA-based damage indices and scores. Fig. 3.22 and Fig. 3.23 illustrate the determination of the Q index and T^2 indexes for the P1 in damage categorization for the holes that are 5 mm, 8 mm, and 10 mm in diameter. The P1 was chosen to show

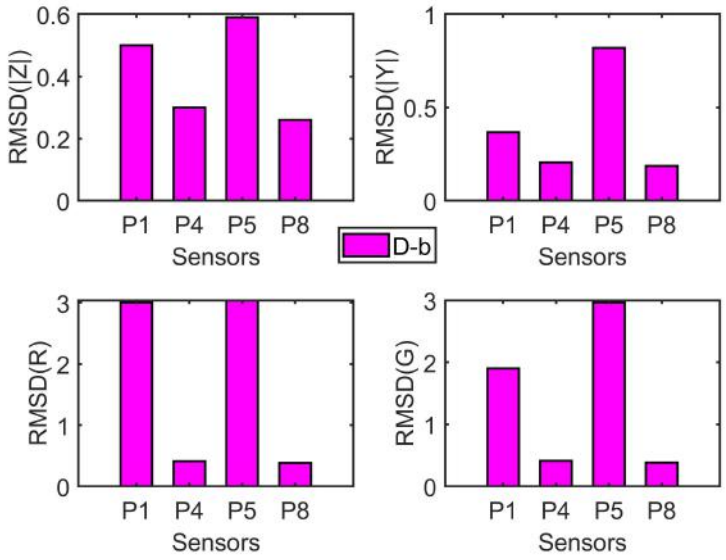

Fig. 3.21 Sensor network 1st PC RMSD damage index for the 'D-b' location for the variables (a) |Z|, (b) |Y|, (c) R and (d) G.

the change of the Q index (eq. 3.9) and T^2 index (eq. 3.10) based on the highest degree of damage sensitivity of all the piezo-actuators. These indices are displayed against the rearranged dimensional score of the four sensor data variables |Z|, |Y|, R, and G which corresponds to 25 measurements in each case, and they indicate small differences.

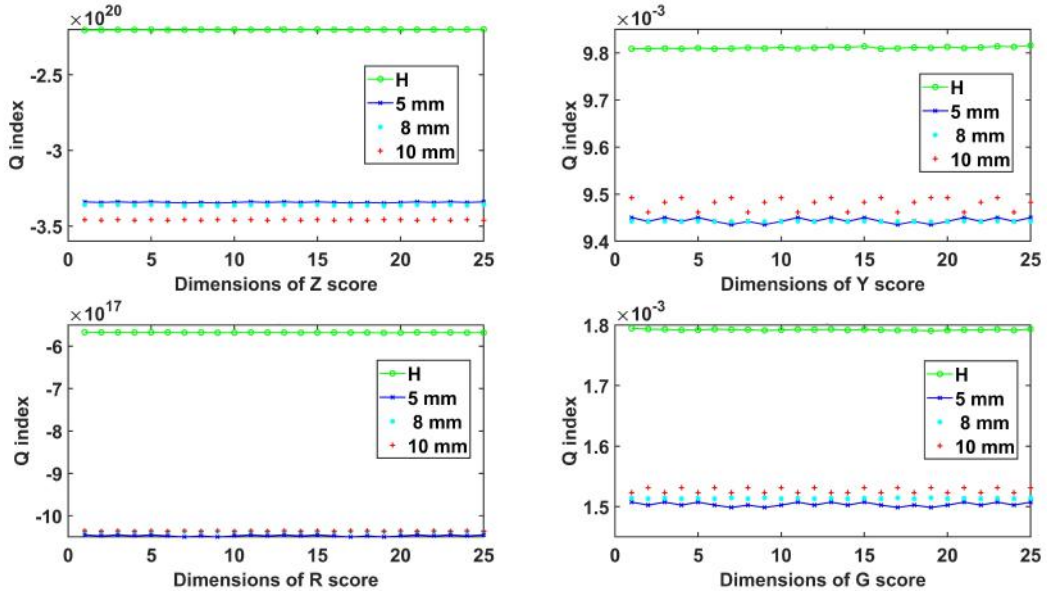

Fig. 3.22 Q index calculation of P1 EMI variables (a) |Z|, (b) |Y|, (c) R and (d) G on a large sample plate.

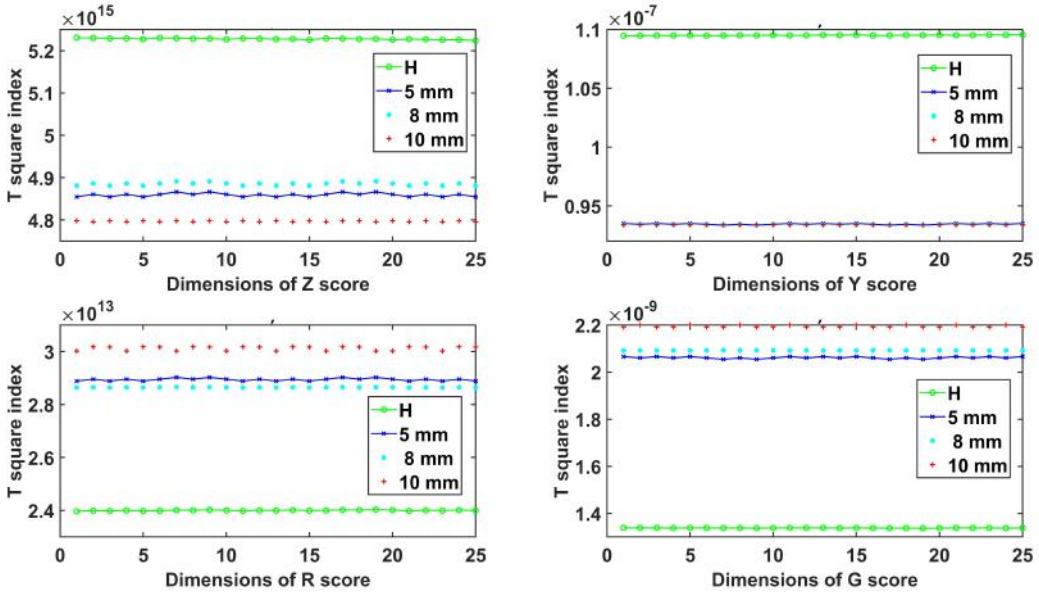

Fig. 3.23 T^2 index calculation P1 EMI variables (a) |Z|, (b) |Y|, (c) R and (d) G on the sample plate.

This is the data fusion stage, where the results from the Q index and T^2 index for healthy, 5 mm, 8 mm, and 10 mm diameter drilled holes are combined for |Z|, |Y|, R, and G by entering them as input to the SOM. Based on heterogeneous feature-level fusion, a SOM can be used to organize and compare similar and dissimilar features. Using the input to the SOM, variables of piezo-actuator P1 are grouped into a data matrix. The variance approach is used to further normalize these datasets. The training time for the feature data is quite minimal and mostly depends on the amount of the score because the input to SOM is in terms of the indices (Q index and T^2 index). In this process, 42 neurons were employed in total. The organized classification matrix data component of the |Z|, R and |Y|, G variables of the piezo-actuator P1 was trained using the batch algorithm. Based on their intended use, data visualization techniques using the SOM are divided into three categories: 1. visualization of components/variables: component planes; 2. visualization of clusters and shape of the data: projections of U-matrices based distance matrices; and 3. visualization of data projections: hit histograms. In order to display the SOM's cluster structure, distance matrices are frequently utilized. They display the separations between adjacent units and are hence closely related to single linkage clustering methods. The U-matrix is the distance matrix method that is most frequently employed. The map's U-matrix is displayed here (using all three components in the distance calculation). The U-matrix of hexagonal topology and cluster of aluminum plate health are shown in Figs. 3.24 and 3.25 using the SOM toolbox as mentioned earlier in the methodology section based on distances between neighboring Q index and T^2 index. The

aggregate distribution of the index components is displayed on the map in the hit histogram as a grey color. Greater discrepancies of the Q index the T^2 index components are shown by higher values of the U-matrix based damage classification, respectively. Based on the best matching unit (BMU) of the associated indices, these hits histograms are computed. The damage case D-a (holes of 5, 8, and 10 mm diameter are considered here as one damage case) is labeled by the red color, while the healthy state (H) is indicated by the green color.

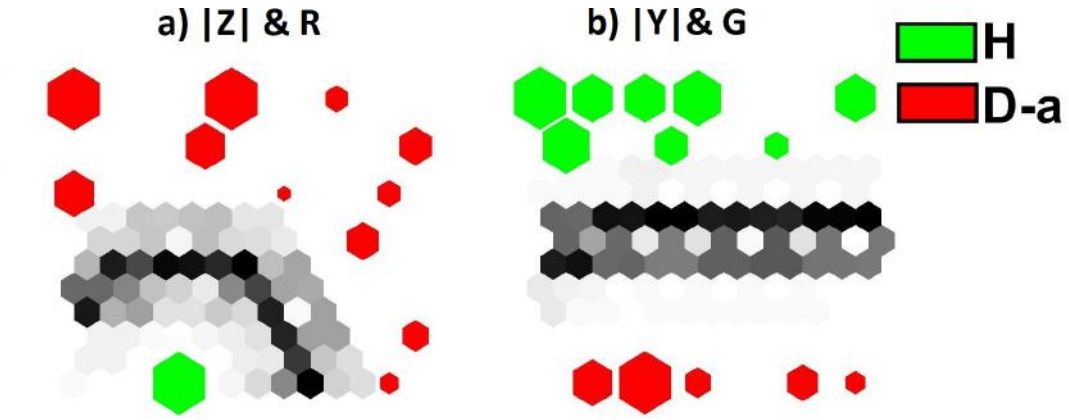

Fig. 3.24 Matching hits based healthy (H) and damage data (D-a) classification for the Q index of piezo-actuator P1 in aluminum plate using (a) |Z| and R (b) |Y| and G.

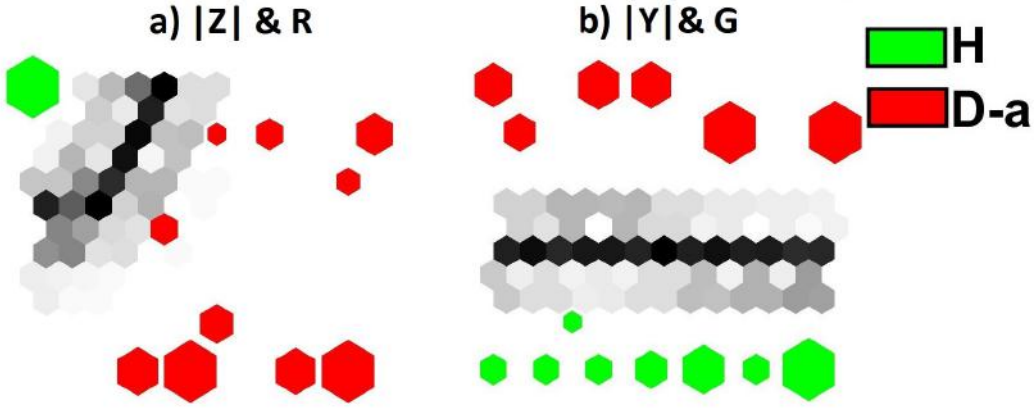

Fig. 3.25 Matching hits based healthy (H) and damage (D-a) data classification using T^2 index of piezo-actuator P1 in aluminum plate using (a) |Z| and R (b) |Y| and G.

Additionally, damage severity of holes with diameters of 5 mm, 8 mm, and 10 mm is categorized using the colors green, blue, and red. As seen in Fig. 3.26 and Fig. 3.27, these

values for the Q index and the T^2 index are clearly distinct, supporting the quality of the information used in the damage detection.

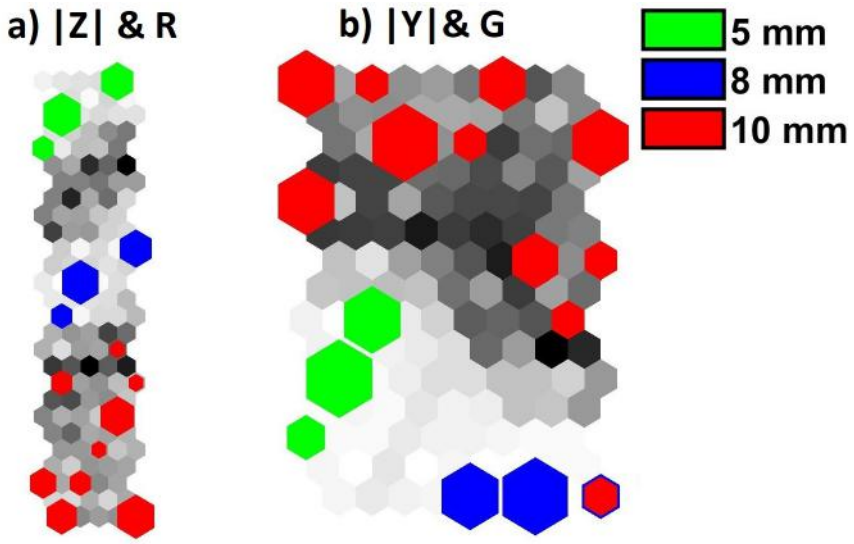

Fig. 3.26 Matching hits based 'D-a' damage severity (5 mm, 8 mm and 10 mm hole) data classification for the Q index of P1 in aluminum plate using (a) |Z| and R (b) |Y| and G.

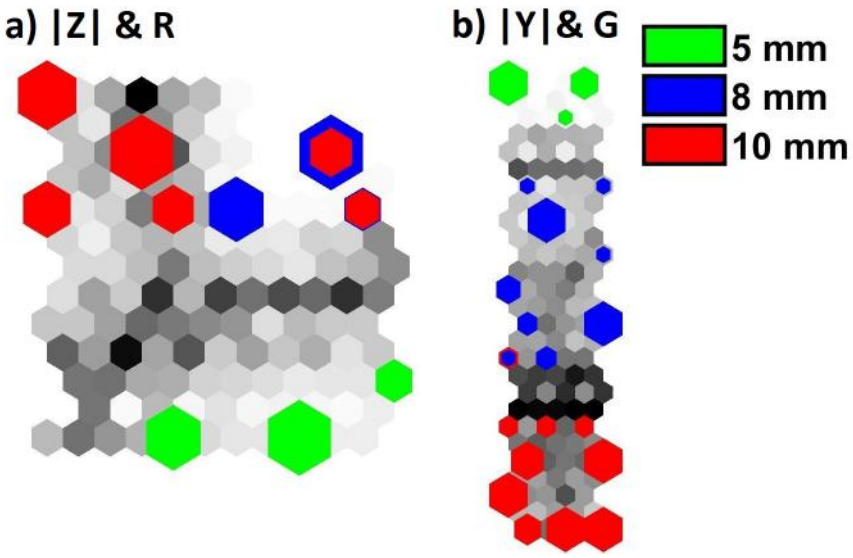

Fig. 3.27 Matching hits based damage 'D-a' damage severity (5 mm, 8 mm and 10 mm hole) data classification for the T^2 index of piezo-actuator P1 in aluminum plate using (a) |Z| and R (b) |Y| and G.

Due to its highest sensitivity out of all the piezo-actuators employed for damage detection in the second damage scenario, "D-b", the actuator P5 was chosen to illustrate damage

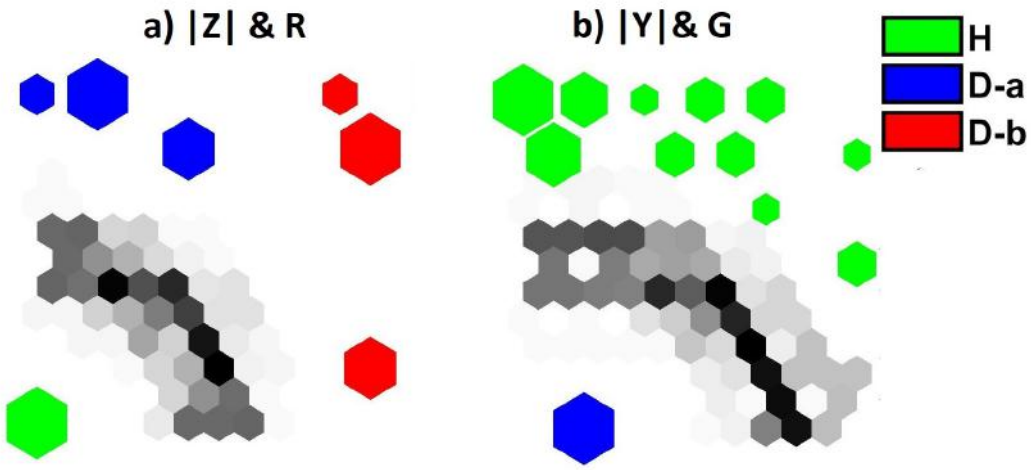

Fig. 3.28 Matching hits based healthy and damage locations data classification for the Q index of piezo-actuator P5 in aluminum plate using (a) |Z| and R (b) |Y| and G.

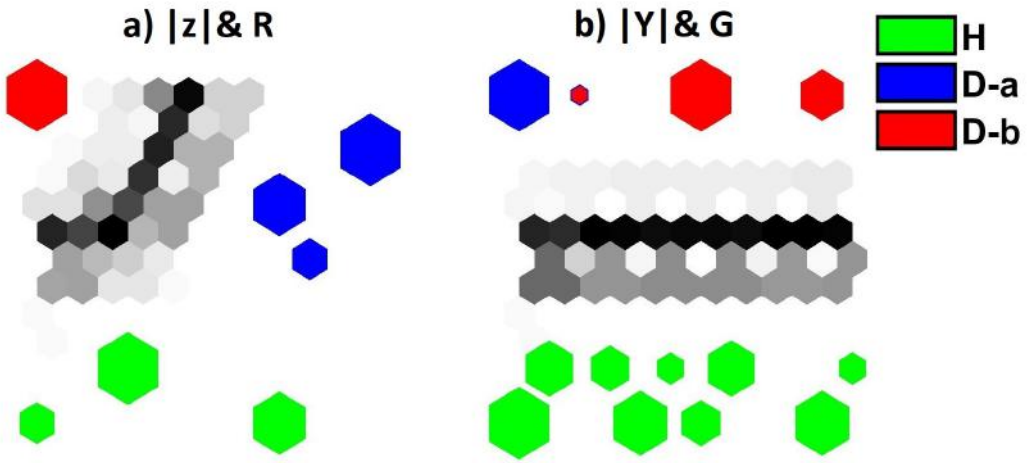

Fig. 3.29 T^2 indices based matching hits classification of healthy-H, damaged state-'D-a' and 'D-b' of the structure for the P5 in aluminum plate using (a) |Z| and R (b) |Y| and G.

classification. As shown in Figs. 3.28 and 3.29, the |Y| and G based fused Q index and the T^2 index are unable to distinguish between healthy (H) and damage cases (D-a and D-b). The fusion of variables |Z| and R is therefore a superior quality of data than variables |Y| and G, supporting the calculation of the fusion-based RMSD index. The technique involved the merging of data with similar unit definitions. It is also noted that damage classification based on the Q index is less sensitive because it cannot classify all damages, but the T^2 index is more sensitive and recommended for use.

Chapter 4

Sensor network based damage imaging

4.1 Background

Even while EMI-based damage detection received a lot of attention, damage imaging localization algorithms received much less attention. Ultrasonic-guided wave frequently uses a probability weight function-based damage detection method that benefits from larger weights for particular mathematical aspects [116]. Direct-coupled mechanical impedance (DCMI) based derived signatures were employed for damage localization using a modified probability weight function damage imaging algorithm that Zhu et al. suggested [117]. They use 16 sensors placed evenly to locate damage on a honeycomb composite plate. Using a finite element model, Kralovec et al. [118] constructed a relationship between the distance and damage index, such as the RMSD and MAPD. For the purpose of detecting damage in an isotropic Al plate, they constructed an exponential relationship and employed the triangulation approach. Experimental verification of the developed exponential relationship revealed good agreement in an extremely narrow frequency band, which has an impact on the system's robustness. Furthermore, the detection of damage at places outside of the network was not shown due to the sparse sensor count. For the purpose of locating damage, Cherrier et al. [61] developed the inverse distance weighting technique. Based on the theories of acoustic wave attenuation, they established the relationship between the damage index and the distance and used it for impact localization. Experimental validation of the method was performed on a beam and plate construction with two and three actuators, respectively. A damage localization method was developed by Na et al. [70] based on a probabilistic neural network that was trained on 90 damage scenarios and evaluated on 6 scenarios. Although the network functions effectively, the resolution of damage is not as accurate as would be expected from NDE/SHM methodologies. Even so, this might be enhanced with more sensors and training data. The process of generating training data does take a considerable amount of time.

The work of the data fusion-based damage detection approach was expanded upon in this chapter to include data fusion-based damage localization. A comparison of damage imaging's radius resolution is conducted to achieve exact localization in less time. The effectiveness of damage localization has been tested by the comparative application of the damage imaging methodology utilizing various damage metrics, such as normalized RMSD, DCMI, fused F data, etc. Further, sensor network optimization has been done for the **multi-damage detection** simultaneously using the damage imaging approach for sensor-network based damage detection in the structure. In order to enhance damage localization accuracy, a novel **inverse method** is also used. In the suggested method, an analytical model of the relationship between distance and angle with respect to the damage index (DI) is established using a data-driven methodology. This methodology is utilized to construct an analytical model based on the correlation of distance and angle with the DI.

4.2 Damage imaging approach

4.2.1 Comparative study of sensing radius using different types of EMI signals

A square GFRP plate with six layers of 0 degree ply was used for the EMI studies. The EMI data are measured for a GFRP composite plate with four sensors. The composite plate has the following dimensions: 40 x 40 x 0.1 cm^3. The damage, which is depicted in Fig. 4.1, was caused by a hit with a projectile that had a spherical end with an energy of 30 J. Using a trial-and-error methodology, the damage analysis involves choosing the optimal sensing radius while moving the damage location away from the sensor network in a range of frequencies between 50 and 140 kHz. Fig. 4.2 displays the G plot for all sensors in both a healthy and damaged state.

R and G information from sensors are evaluated in the frequency domain, and data fusion is accomplished at the variable level using fused variable F, which is created by multiplying G and R, as mentioned in Chapter 2 section 2.2.1.

In the normalized data (ND) approach, the sensor's G information is divided by the maximum absolute data points for G as given in Eq. 4.1.

$$G_{modified} = \frac{G}{max|G|} \tag{4.1}$$

The DCMI signatures extraction approach is utilized from the sensitive portion of the EMI coupling model described in Eq. 1.4. Z_f is a DCMI in the complex domain and expressed by

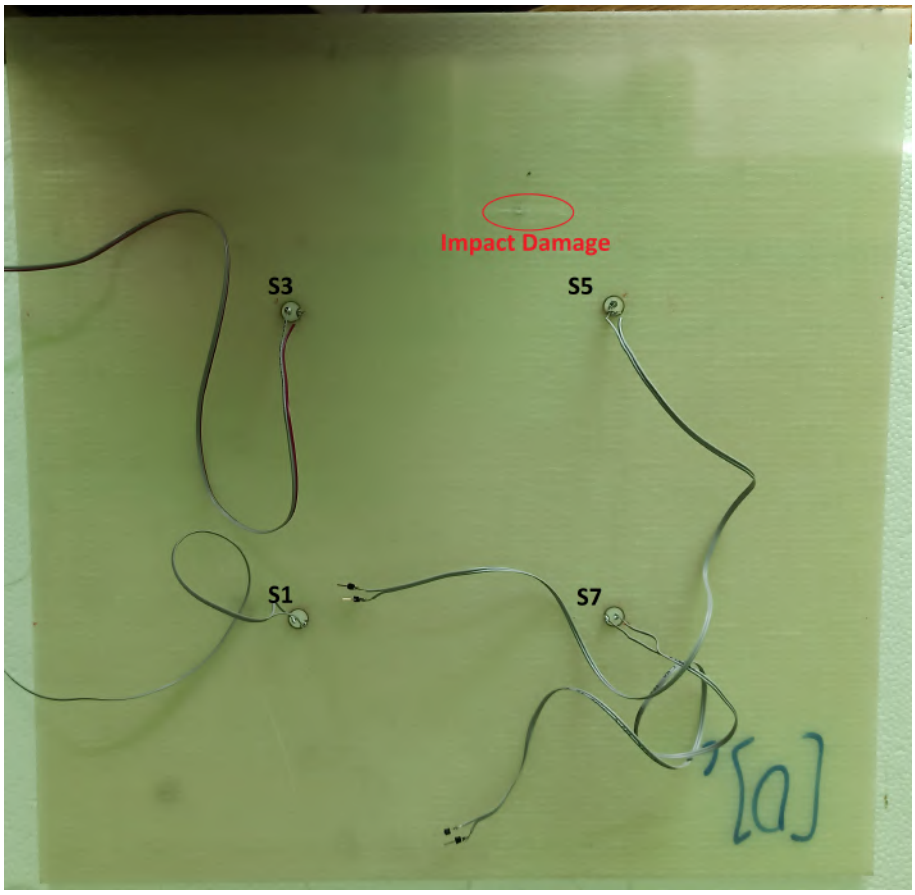

Fig. 4.1 Composite plate with bonded sensor network and with the impact damage.

Eq. 4.2.

$$Z_f = x_f + jy_f = \frac{Z_s(\omega)}{Z_a(\omega)} \tag{4.2}$$

where, x_f is the real part of the DCMI expression while y_f is the imaginary part. $Z_a(\omega)$ is the short-circuited mechanical impedance of actuator, $Z_s(\omega)$ is the mechanical impedance of structure [117].

An ideal sensing region radius (r) value in the sensor network can be found using damage location accuracy (DLA), and is required for proper damage localization. DLA is determined by Eq. 4.3 and is the inverse of positional deviation.

$$DLA = \frac{1}{\sqrt{(x_r - x_c)^2 + (y_r - y_c)^2}} \tag{4.3}$$

where (x_r, y_r) denotes the real position of the damage and (x_c, y_c) denotes the calculated position.

The plot of G for the sensor network is studied in the 1 kHz- 150 kHz frequency range where maximum variation occurs in the signatures as shown in Fig. 4.2.

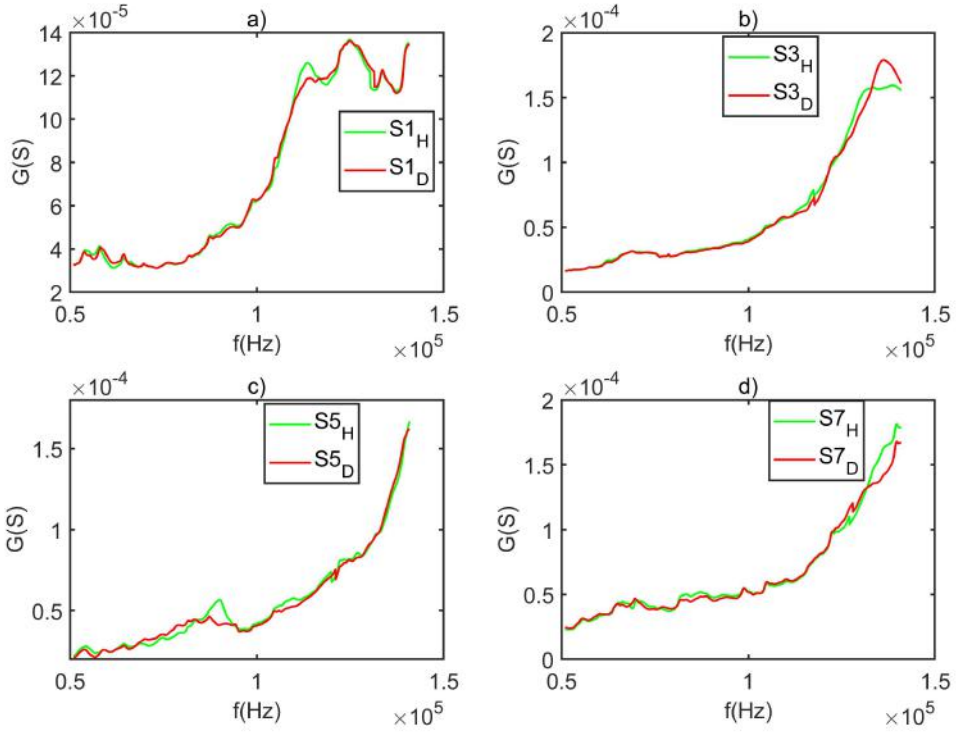

Fig. 4.2 The comparative plot for the raw G signature in 2x2 PZT array.

The method has investigated the effects of damage imaging's location accuracy (DLA) behavior for both big and small r steps/intervals. Through the testing of various 'r' values, the relationship between the 'r' value and DLA is examined in connection to structural damage. Fig. 4.3 displays the DLA on the vertical axis and the sensing region's radius (r) on the horizontal axis. For the highest value of DLA, there is an ideal 'r' value to use while performing damage localization. The 'r' value of the 1 mm, 5 mm, and 20 mm steps and intervals were examined. The 'r' value is the same for movements with small intervals of 1 mm and 5 mm, but for movements with wide intervals of 20 mm in the same frequency range, there is a minor deviation. The stimulation frequency, PZT types, structure characteristics, and shape are the key determinants of the r-value. From Fig. 4.3, it can be shown that the 'r' value deviates little at increasing sensing radii. The initial 'r' value is 806 mm, while for the larger steps of 20 mm, 'r' value is 821 mm.

The damage image plot for extracted changed signatures is then compared using a large step of 20 mm radius of the sensing region. The large step simulation often takes less time, requires fewer computer requirements, and has a much smaller accuracy difference. Fig. 4.4,

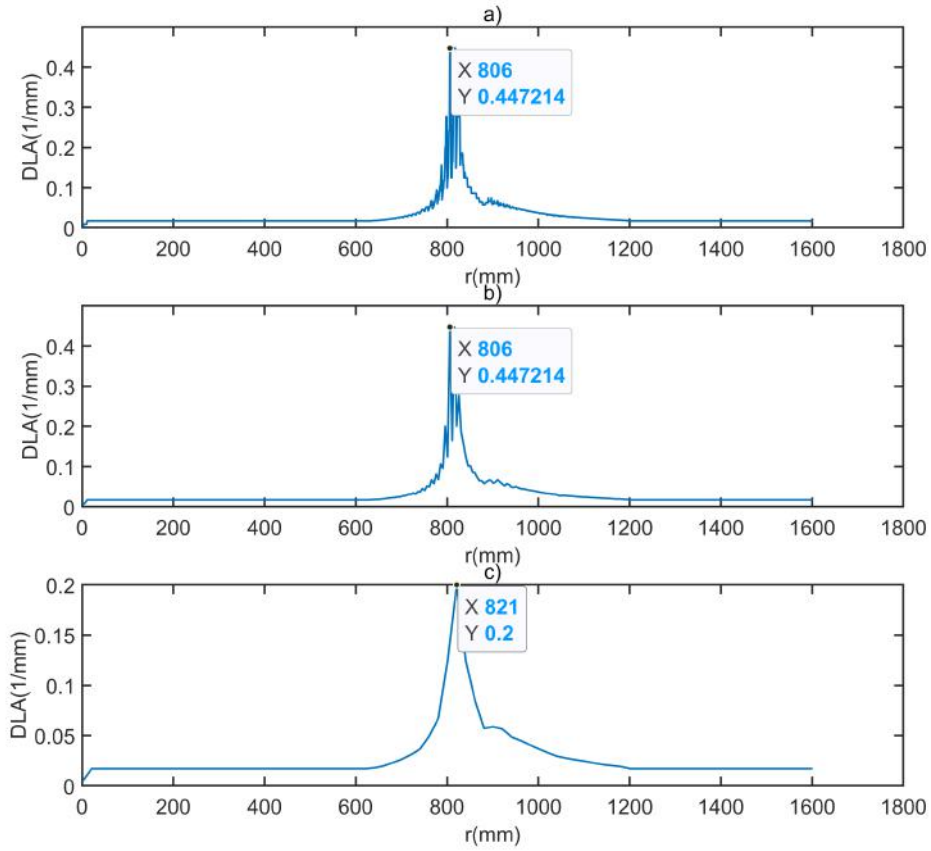

Fig. 4.3 The plot between radius of sensing region (r) and DLA for normalized data a) r=1 mm, b) r=5mm and c) r=20mm.

which shows the DCMI and fused F data r plots, respectively, suggest the ideal 'r' values of 501 mm and 1084 mm.

Because big intervals take less time and require less computation, the current study demonstrates a modified probability weight function-based damage imaging approach for the large steps/intervals of radius (r) in GFRP plates. Additionally, the method compares the efficacy of DCMI data, fused F signature data, and modified normalized data (ND) data of G signals for the big interval. The composite plate with impact damage was used to show how damage imaging works with probability weights. Eq. 4.4 illustrates the probability weight function that is employed in EMI-based damage imaging to determine the weight values for

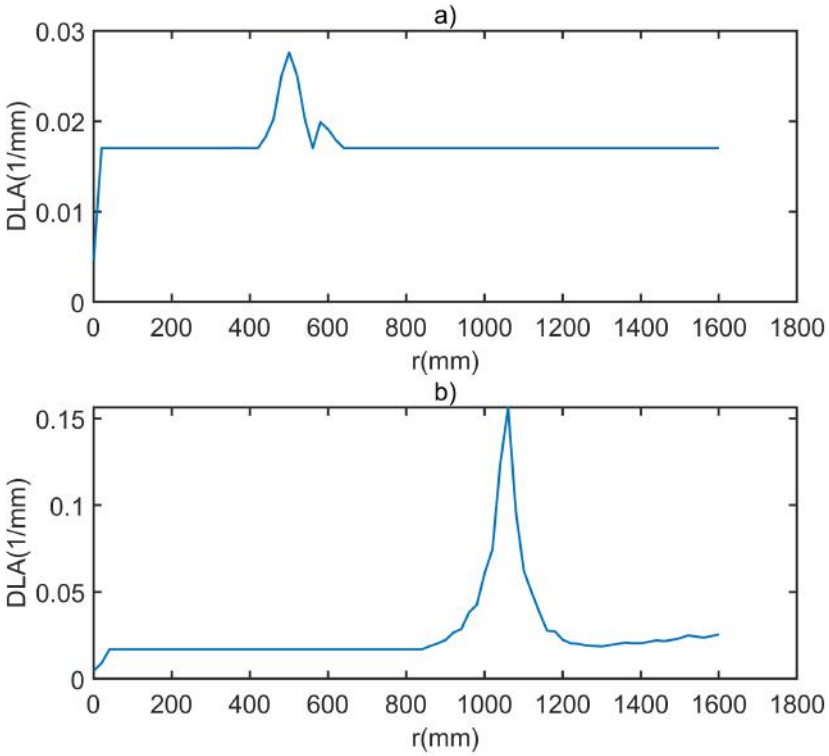

Fig. 4.4 The plot between radius (r) and DLA for a) DCMI and b) fused F at 20 mm interval.

each element.

$$W_i[l_i(x_i,y_i)] = \begin{cases} 1+[\frac{l_i(x_i,y_i)}{r}-(1-\frac{d_i}{d_{max}})], & \text{if } l_i(x_i,y_i) < (1-\frac{d_i}{d_{max}} \times r) \\ 1-[\frac{l_i(x_i,y_i)}{r}-(1-\frac{d_i}{d_{max}})], & \text{if } (1-\frac{d_i}{d_{max}}) \times r < l_i(x_i,y_i) < [1+(1-\frac{d_i}{d_{max}})] \times r \\ 0, & \text{other.} \end{cases} \tag{4.4}$$

where $W_i[l_i(x_i,y_i)]$ denotes the probability function at a given element (x_i,y_i). $l_i(x_i,y_i)$ denotes the Euclidean distance between the element (x_i,y_i) and PZT. d_i is the calculated RMSD damage indices of EMI signals. d_{max} is maximum value among all damage indices of the sensor network. r is the sensing region radius of the piezo-actuators on the surface of the structure.

Eq. 4.5 uses the weight function of the distance between the piezo-actuator and the element to calculate the probability weight density of the sensor network. In comparison to other indices, the DI value for damage near to PZT is given more weight. By plotting the above-estimated probability density distribution in monitored structures, damage localization can be implemented.

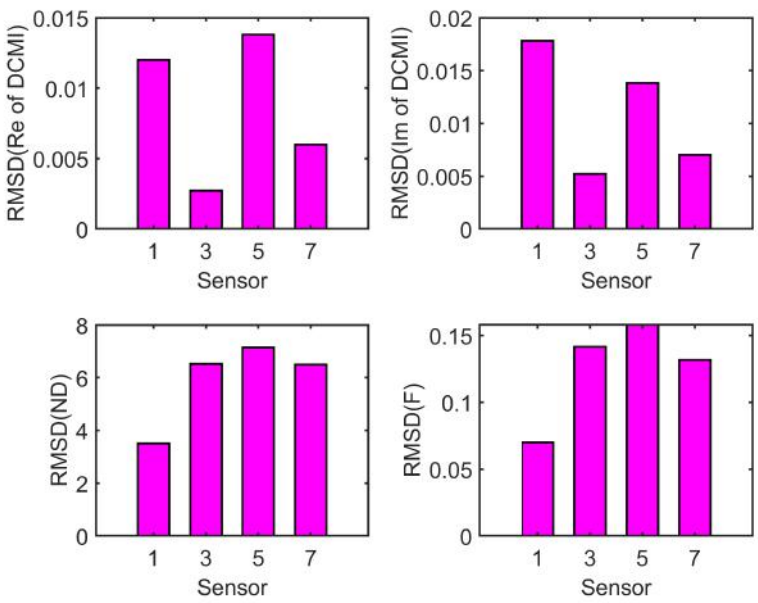

Fig. 4.5 A comparative RMSD plot for DCMI real and imaginary data, ND data and fused F data.

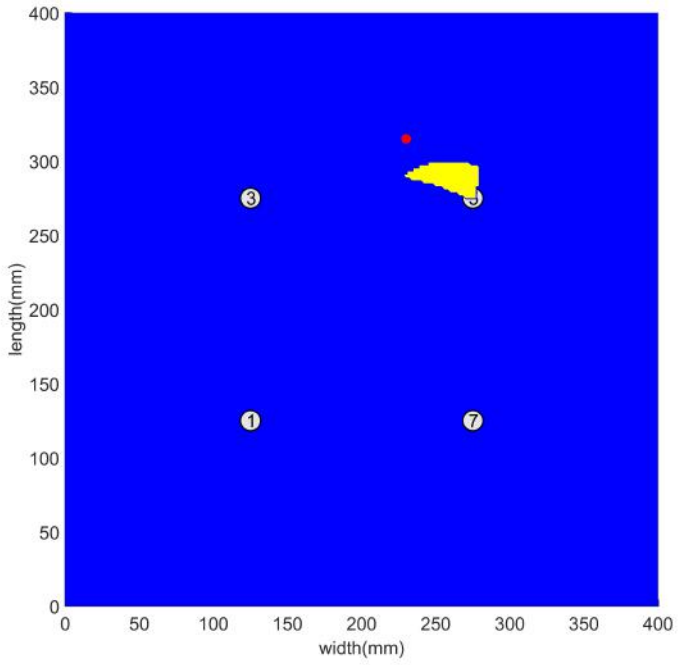

Fig. 4.6 Illustration of impact damage on the composite structure using real part for the DCMI signatures.

$$p_i(x_i, y_i) = \sum_{i=1}^{N} W_i[l_i(x_i, y_i)]d_i \tag{4.5}$$

Where N is the total number of the sensors in the sensing network.

In comparison to S1, S3, and S7; S5 exhibits the highest RMSD sensitivity, as seen in Fig. 4.5 except DCMI imaginary signature based RMSD. Since the real part of the DCMI signature has demonstrated more accurate damage imaging, it is explored here [117]. The actuator S1 which is farthest from the impact damage has the lowest RMSD value. Fig. 4.5 shows the comparative DI plot of ND signatures, rescaled fused data F, and DCMI curve in the frequency range of 50-140 kHz. The differences between the composite structure's healthy and damaged states are shown by the heights of the RMSD bars. As a complex number, the DCMI expression is also broken down into real and imaginary parts for analysis.

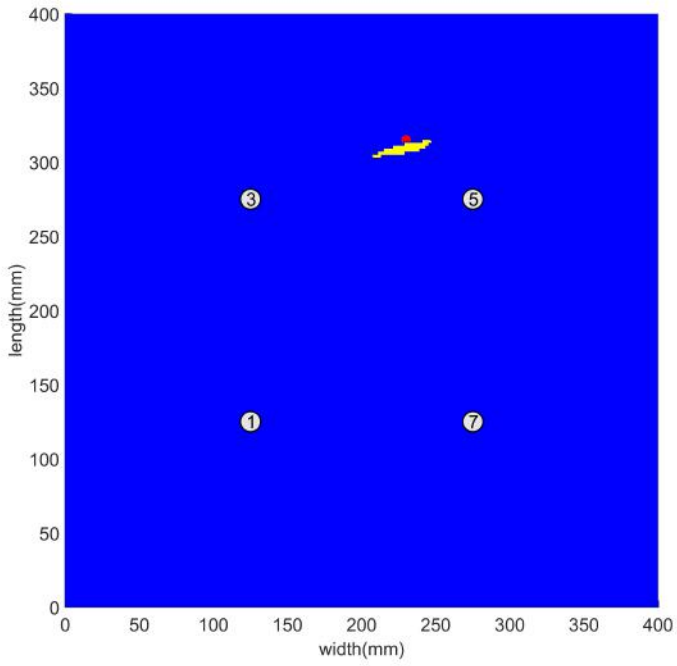

Fig. 4.7 Illustration of impact damage on the composite structure using fused F signatures.

Figs 4.6, 4.7, and 4.8 each demonstrate the damage imaging of the impact damage location utilizing DCMI, fused F, and ND signatures. The actual damage position in an impact damage scenario is indicated by the red circle, while the predicted damage state is shown by the yellow shape. The yellow shape of the predicted damage is big for DCMI and small for ND signature. Based on Euclidean distance, the error in identified damage and actual damage location is 10.14 mm, 10.12 mm, and 30.24 mm for the fused F, ND, and

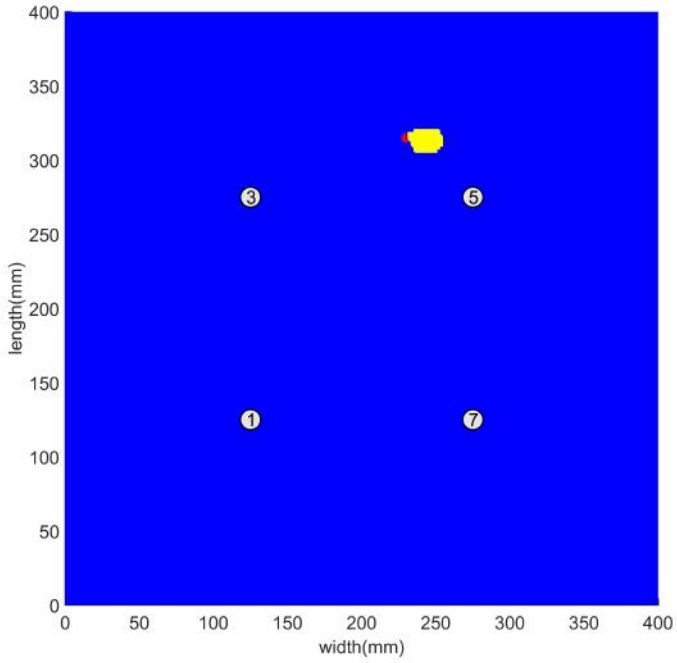

Fig. 4.8 Illustration of impact damage on the composite structure using the ND signatures.

DCMI signatures respectively. In comparison to DCMI, F, and ND signatures have the lowest relative error in Euclidean distance between identified damage site and the actual damage location. The DCMI technique has the maximum Euclidian distance between the precise location of damage and predicted damage, and it looks less accurate for the steps of the large 'r' value.

4.2.2 Multi-damage localization using sensor network

This part explains sensor network-based multi-damage detection using the damage imaging approach. The validations of the multiple damage detection methods are carried out using simulated damage by magnet placement on an acrylonitrile butadiene styrene (ABS) polymer printed plate with nine sensors having distance 'd' between two consecutive sensors, as illustrated in Fig. 4.9. The suggested strategy, shown in Fig. 4.10, simultaneously localizes one damage case, two damage cases, and three damage cases.

The sensor's resistance value is divided by the maximum absolute value before calculating RMSD-based DI values in the frequency range of 1 kHz-200 kHz. Using Eq. 4.3, the sensing region r of the sensor network has been explored based on DLA for 5mm steps/intervals. Based on calibration of known damage cases, a radius of maximum sensitivity was estab-

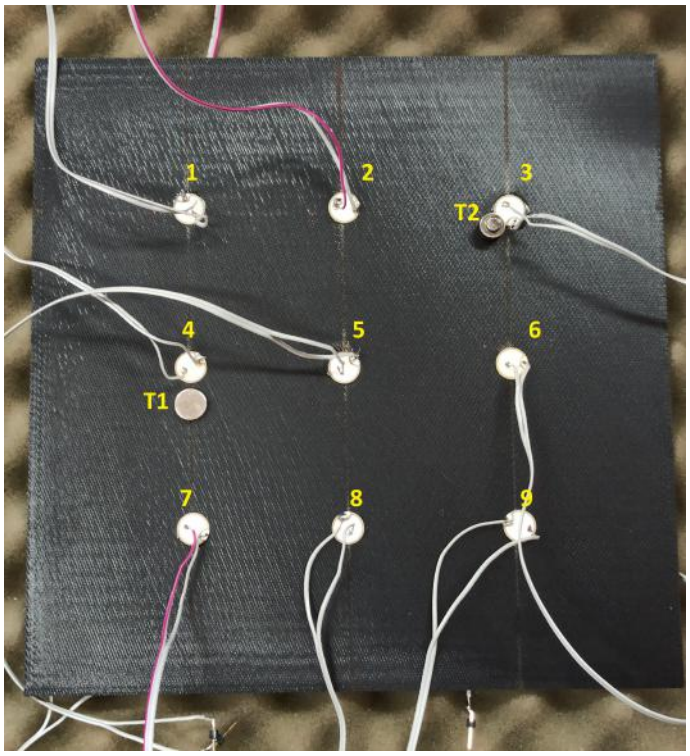

Fig. 4.9 Diagram of sensor network and multiple damage to an ABS plate.

lished, with the assumption that the radius would remain constant for all actuators, regardless of their location. The correlation between the r value and DLA is examined in connection to multi-structural damage simultaneously in the same frequency range. For the highest value of DLA, there is an optimal r value for the damage localization found to be r_{op}= 66 mm. The following procedures are adopted for the localization of a single damage.

- Firstly, DI is calculated for the healthy and damage states of all the available sensors.
- The highest DI of the repeated healthy measurements among all the sensors is named $DI_{threshold}$. All the sensors with DI above $DI_{threshold}$ are selected as suitable candidates to be used for damage localization. Consequently, sensors 1, 2, 4, and 5 are found suitable for damage localization in this case, as shown in Fig. 4.11.
- All the available three-sensor combinations from the set of the selected sensors are determined, from 4 sensors in the current case. Each three-sensor combination will hereafter be referred to as a triangle.
- The triangles based sensors having the distance between each two sensors less than or equal to the optimum radius ($d \leq r_{op}$) are further selected for damage localization. In

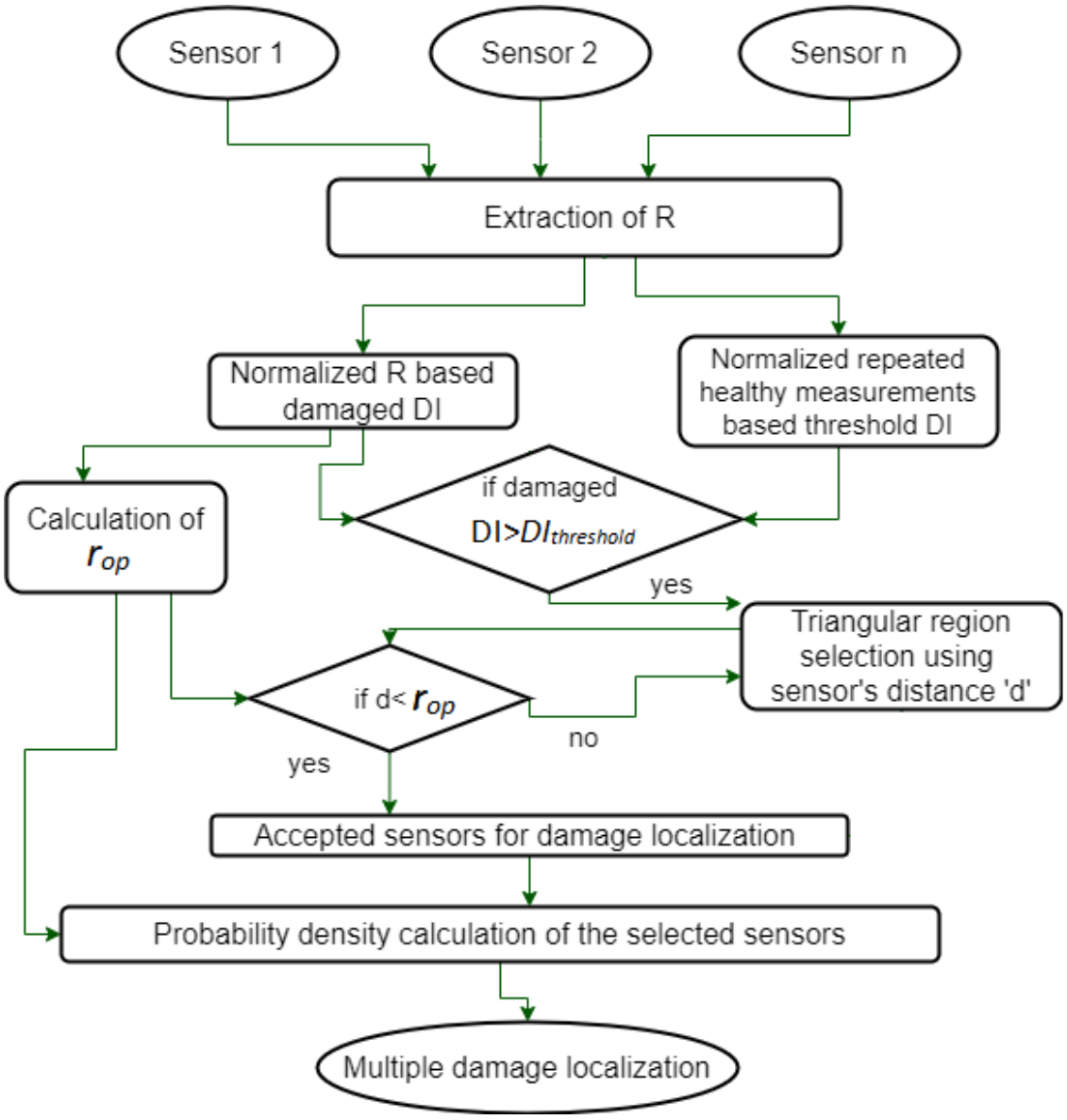

Fig. 4.10 Multi-damage detection flowchart.

this case, all the available combinations are selected, where the formed triangles are 4-5-1, 5-4-2, 1-2-4, and 2-1-5.

- The location of a single defect is determined by triangles forming a quadrilateral. If multiple quadrilaterals are formed by the selected triangles, the quadrilaterals are separated for multiple-damage localization. This updates the number of potential damage locations. Since T1 is a single-damage case, the selected triangles form a single quadrilateral 1-2-4-5, as shown in Fig. 4.12a.

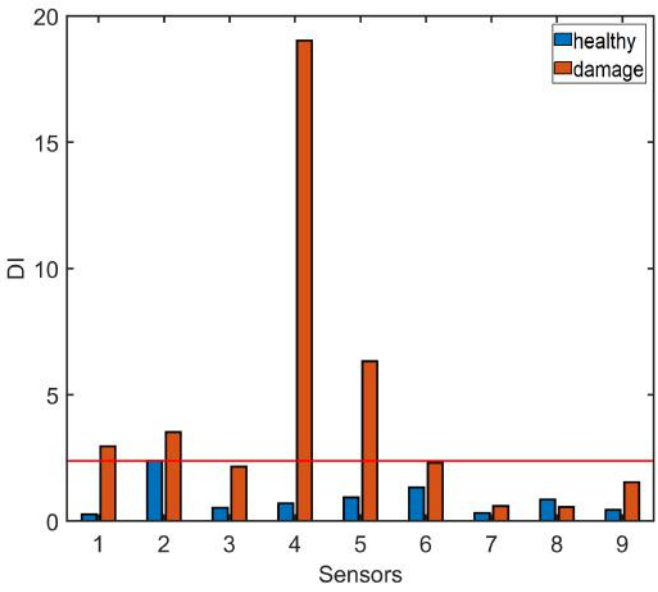

Fig. 4.11 DI of sensor network for single damage detection.

- The sensors corresponding to each of the quadrilaterals are stored separately to be used for damage localization.
- Eq. 4.5 is used to calculate the probability-density-based damage-localization image for each available quadrilateral. The localization of the single-damage case T1, using the proposed method, is shown in Fig. 4.12b.

For the two damaged cases, the DI of the respective sensors for healthy and damaged cases are given in Fig. 4.13. Using the same procedure stated above, the triangles used for damage localization are 7-4-5, 4-5-2, 2-3-6, 2-5-6, 5-6-3, and 5-2-3 based on the condition of $d \leq r_{op}$. Examining the triangular distribution of sensors that suggests a potential region with the defect location is shown in Fig. 4.14a. The location of each defect is determined by triangles of sensors forming a quadrilateral. The first best triangle of sensors formed quadrilateral: 2-4-5-7 of sensors. The algorithm moves on to the next phase for detecting the second damage and updates the number of sensors for the possible second quadrilateral 2-3-5-6 of sensors. Then each sensor is arranged according to respective DIs for each quadrilateral to localize the damage. The localization of two-damage cases T1 and T2 simultaneously with the proposed method is shown in Fig. 4.14b.

For the three damage case, the DI of the respective sensors are given in Fig. 4.15. The triangle of damage identifications are 4-5-1, 5-4-2, 1-2-4, 2-1-5, 2-3-6, 2-5-6, 5-6-3, 5-2-3, 8-5-6, 8-9-6, 5-6-9, and 5-8-9. By examining the triangular distribution of sensors with

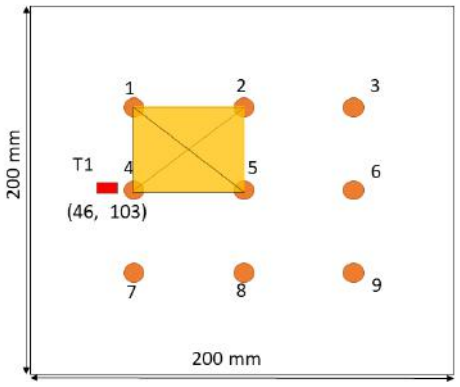

(a)

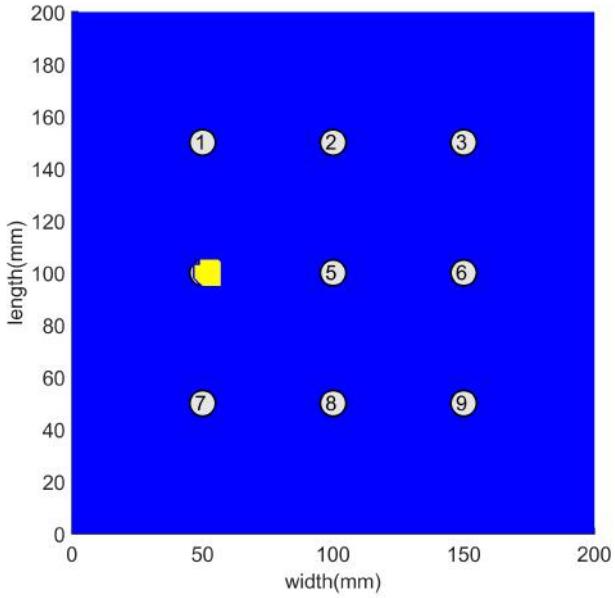

(b)

Fig. 4.12 Single damage detection using a) triangular coverage and b) damage imaging.

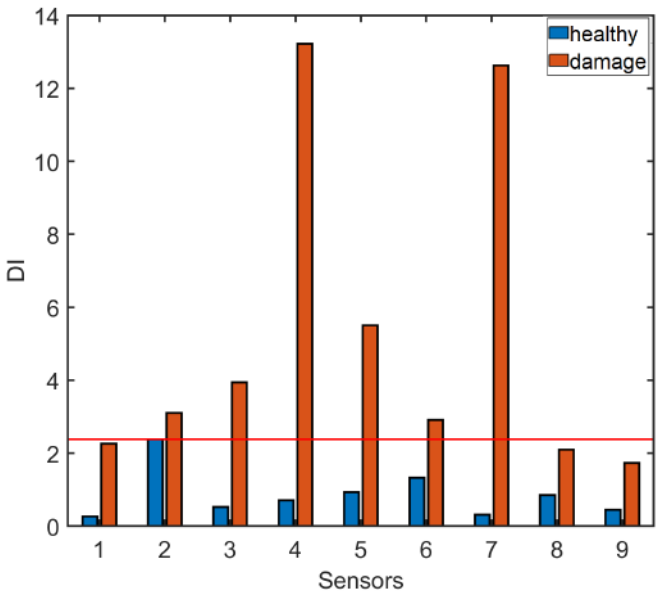

Fig. 4.13 DI of sensor network for two damage detection using normalized RMSD.

the defect location is shown in Fig. 4.16a. Using these triangles, formed quadrilateral by sensors are 1-2-4-5, 2-3-5-6, and 5-6-8-9, to detect three damages in the structures. Then, the sensors are arranged according to each sensor's DIs for each quadrilateral to detect

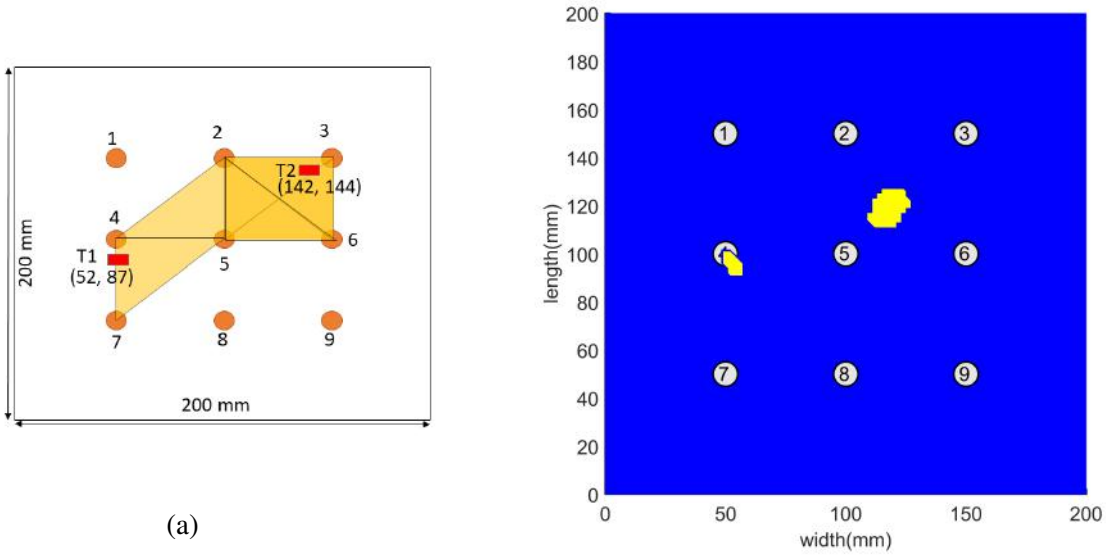

(a) (b)

Fig. 4.14 Two damage detection using a) triangular coverage and b) damage imaging.

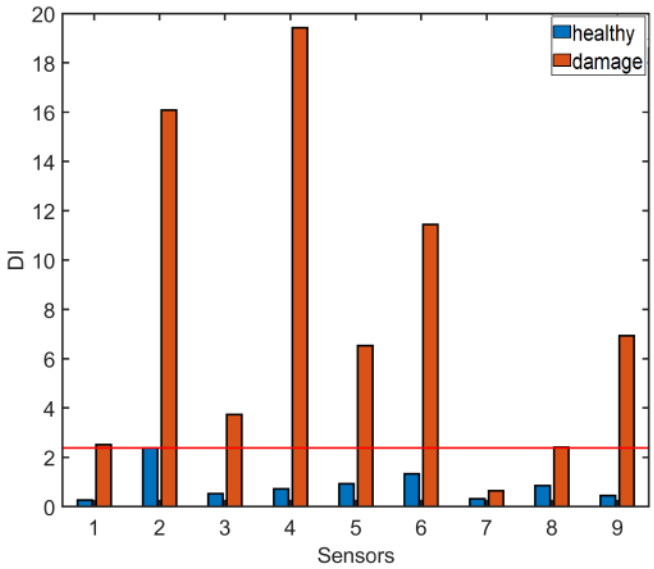

Fig. 4.15 DI of sensor network for three damage detection using normalized RMSD.

the multi-damage locations. Eq 4.5 uses to calculate the probability density-based damage imaging localization of the possible quadrilateral of PZT. The localization of multi-damage T1, T2, and T3 simultaneously with the proposed method is shown in Fig. 4.16b.

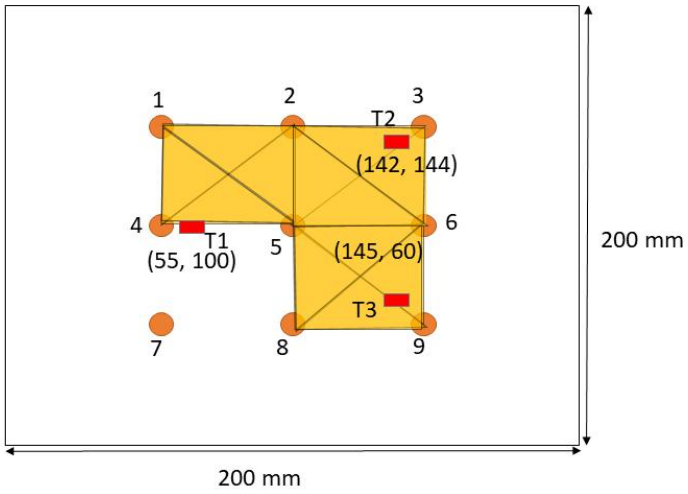

(a)

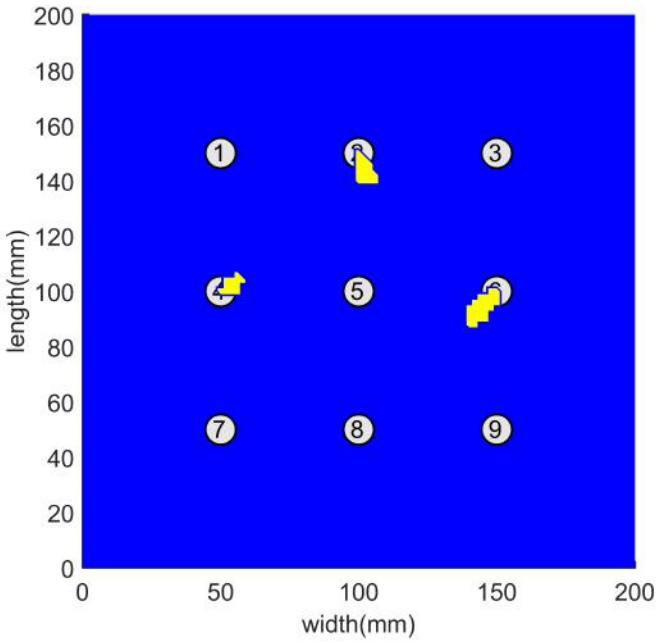

(b)

Fig. 4.16 Three damage detection using a) triangular coverage and b) damage imaging.

4.3 Damage localization based on inverse model

This section continues the pattern by employing a brand-new inverse approach for damage localization to improve accuracy. In conventional techniques the DI for the sensors is used to locate the damage, in the proposed approach the DI is computed for a given damage location and hence is termed as an inverse approach. The establishment of an analytical model in function of the dependence of the distance and the DI is done using a data-driven methodology. This analytical model is then used to calculate the DI for all sensors for a large number of damage locations. The error in the measured DI and the analytically computed DIs is then minimized to obtain the damage location. This enables for more precise damage localization. The study's were used fused data F based DI, which is covered in the section 4.2.1 pf this chapter. Based on the information that can be used for the next steps, any DI can be computed. Due to its reliability and improved performance, the proposed Frechet distance metric based on normalized cumulative power was adopted [119]. By adding a mass of magnets with a diameter of 10 mm, the damage was induced in the plate. Then, using curve fitting, it is discovered how the DI depends on the angle and distance from the sensor. Eq. 4.6 can be used to define the analytical equation for the dependency of DI on the angle and distance.

$$DI(s,\theta) = f(s)h(\theta) \tag{4.6}$$

where 's' is the separation between the sensor and the damage location, and θ is the angle between the two. For anisotropic constructions, such as composites, the dependency of DI with angle is required.

Figs 4.17 and 4.18 depict the DI values for varying distance and angle in the composite structure based on the work done by Kralovec et al. [118] to fit the exponential distribution and by Zhu et al. [117] on a linear fit. The function f(s) for linear and exponential fit is given in Eq. 4.7 and Eq. 4.8 respectively.

$$f(s)_{lin} = m.s + c \tag{4.7}$$

$$f(s)_{exp} = m1.e^{m2s+m3} + m4 \tag{4.8}$$

where m=-9.18 $\times 10^{-4}$, c=0.0024, m1=0.004, m2= -0.0089, m3= 0.002 and m4=0.00012 are constant values. The linear fit has a R squared value of 0.9 whereas the exponential fit has a value of 0.96. Additionally, a visual comparison reveals that the exponential fit outperforms the linear fit in terms of agreement and error.

An absolute cosine fit given by Eq. 4.9 was deemed suitable for the dependence on the angle due to the structure's symmetry about x and y axes.

$$h(\theta)_{cosine} = c1 \times |cos(\theta + c2)| + c3 \tag{4.9}$$

where, c1 = 1.9430×10^{-4}, c2 = -7.1103 and c3 = 0.9025 and θ is in degrees.

Once the analytical model has been established, the DI values for each actuator can be generated using it. In the present study, the plate was discretized with a resolution of 41×41. This resolution was chosen to match the size of the magnets (10 mm diameter) used for simulating the damage corresponding to the size of the structure. This resolution gave a total of 1681 possible damage scenarios. The technique was examined for impact damage of 30J. When the plate was equipped with 4 sensors (namely S1, S3, S5, and S7), impact damage was introduced. Only these 4 sensors were employed for the impact analysis because the baseline for just those 4 sensors was available. An error based sensor elimination procedure is implemented to rectify for the modeling and measurement errors. The highest DI artificially enforces zero relative error at the sensor location. This enforcement of the zero error ensures that the sensor with highest DI will not be removed and ensures good damage localization. The relative error (RE) for each of the damage scenario is given by Eq. 4.10.

$$RE = |DI_{analytical} - DI_{experimental}| \tag{4.10}$$

The sensors with a relative error of more than 50% are eliminated from the computation, and then a new search is conducted for the damage scenario with the least error. One sensor at a time is removed, beginning with the one that is located farthest away from the identified damage. Until all sensors that exhibit relative error larger than 50% are eliminated, the process is repeated. The damage map for the impact localization using the suggested technique is shown in Fig. 4.19. The damage detection algorithm was run for impact damage (230 mm, 315 mm) which predict the damage position with error of 11.120 mm.

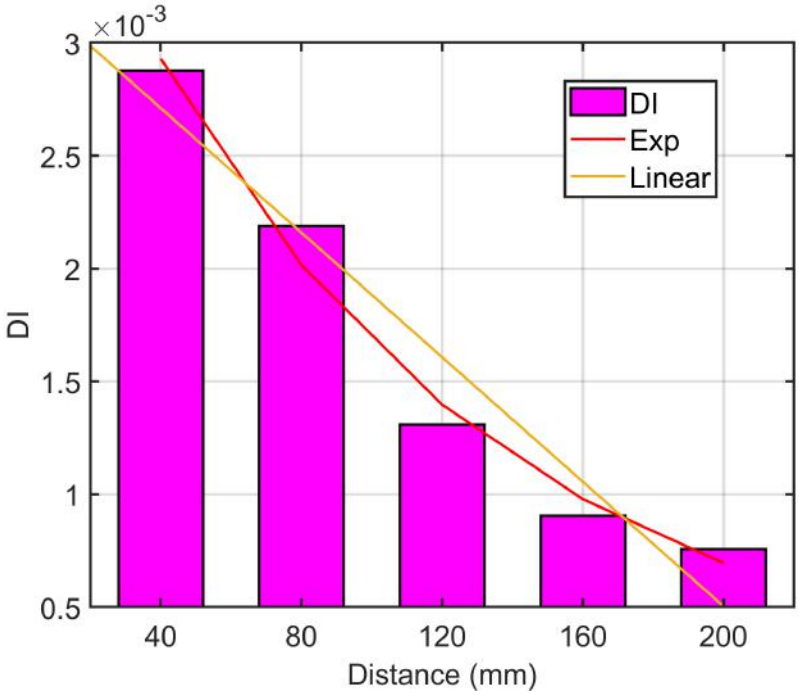

Fig. 4.17 Distance based DI in the composite structure.

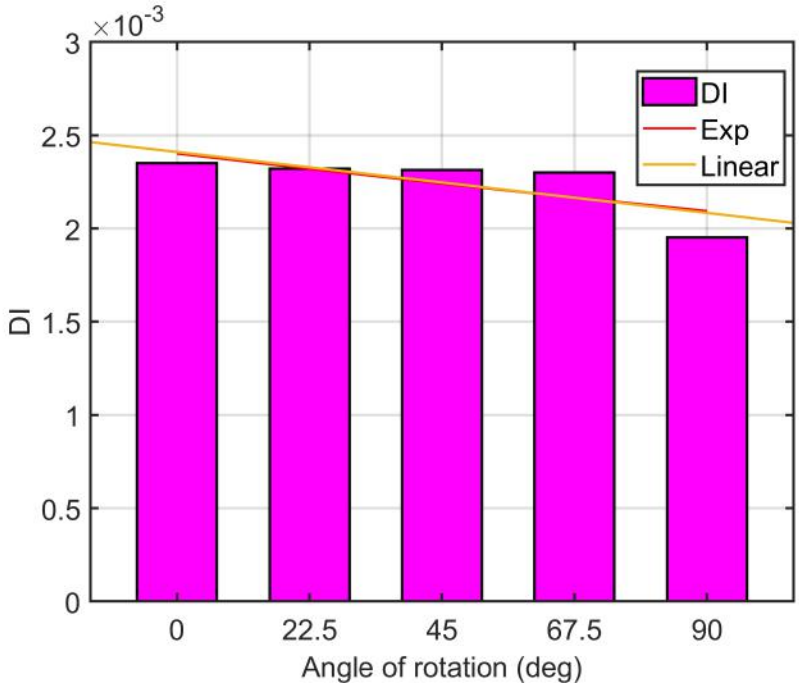

Fig. 4.18 Angle based DI in the composite structure.

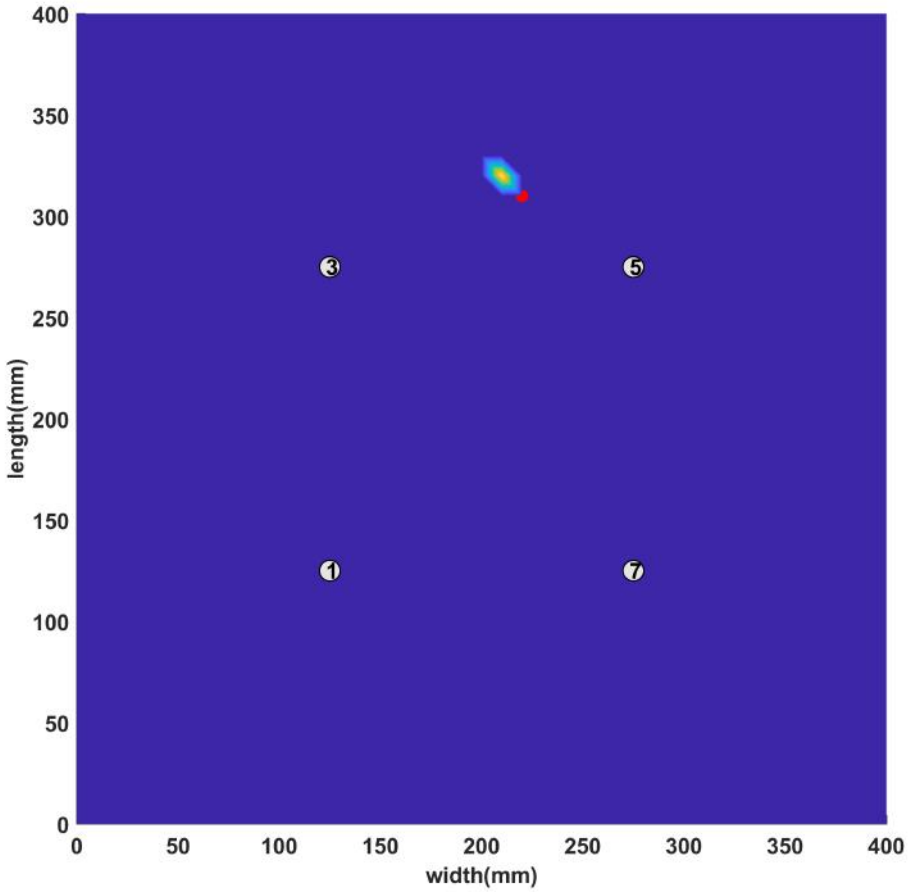

Fig. 4.19 Damage localization based on the inverse mode.

Chapter 5

A standard deviation approach in damage detection

5.1 Introduction

The EMI-based damage detection method's challenging task is choosing reliable and efficient damage indices, frequency ranges, and merging the data for damage quantification. In this chapter, a novel standard deviation approach is utilized to pick the best frequency bands for damage detection. The innovative frequency range selection is motivated by the distinction between data in healthy and damaged states. Further, combining G and R fused data with a probabilistic density function (pdf) to identify and classify the damage. It will aid in deriving reliable information from frequency domain data so that damage detection can be improved through reliable decision-making. For damage identification and classification utilizing analytical and experimental data in this practical frequency range, a data fusion based **probabilistic integral** technique is also introduced. The RMSD index technique is then compared with the combined **C-index** statistical data-driven damage matrices. The approach appears appropriate for concurrently determining both the location and the severity of damage, and it works better in circumstances of less severe damage. Regardless of the sort of damage in the structure, the method is useful for identifying damage since it takes into account the area difference in the structure's health. The damage severity and piezo placement problems are both solved using the newly introduced C-index. The novel approach improved the ability to detect damage when compared to the conventional RMSD approach by employing the highest likelihood area covered under the healthy and damaged state curves for the chosen frequency range.

5.2 Novel frequency range selection methodology

The research emphasizes how crucial it is to choose the effective frequency range to assess the structure's high-sensitivity performance and guarantee strong repeatability.

5.2.1 Need of effective frequency range selection

In comparison to the traditional vibration-based SHM approaches, the working frequency is typically higher than 10 kHz [51]. The wavelength is short enough at such high frequencies to make the EMI approach sensitive to minute changes in structural physical characteristics. On the other hand, due to the local based damage detection approach, the EMI is less dependent on the boundary conditions. According to Park et al., various frequency ranges with 20 to 30 peaks are typically chosen for damage assessment due to the fact that a higher mode density denotes a more dynamic interaction [120]. The selection of an effective frequency spectrum that is difficult to detect for incipient structural damage that has a significant impact on how well the EMI approach performs. The efficiency of the EMI approach depends on the choice of the effective frequency spectrum, which is typically challenging to estimate for the early structural problems. The effective frequency range of the transducer cannot be inferred theoretically from the experimental data. Trial and error can be used to determine the damage detection in EMI method's robust frequency range [91]. According to Peairs et al., the high mode density frequency spectrum exhibits a more sensitive reaction when using the EMI approach than the low mode density frequency spectrum [92]. Yang and Divsholi provided a sub-frequency range based on damage location and severity detection utilizing the RMSD index in the broad frequency range, since PZT resonance frequency also plays a significant influence in the selection of the effective frequency range. Using EMI, Sienkiewicz examined and confirmed the mechanical characteristics such as stiffness, viscosity, and Young's modulus, of soft tissues particularly human skin. The electromechanical equivalent circuit discovered for the actuator's resonance frequency and calculations based on Hertz's contact mechanics theory are connected via an analytically method [121].

This chapter describes the new theoretical way to predict the **effective frequency range** for damage detection from the experimental data of the EMI. This chapter includes two sample instances with different damage scenarios to show how this strategy might be applied. In this study, the sample consists of a small-sized aluminum plate with drilled hole and a composite plate made of glass fiber reinforced polymer (GFRP) with added mass to simulate damage.

5.2.2 Methodology of effective frequency range selection

In the beginning, a novel mechanism for selecting an appropriate frequency range based on standard deviation (σ) is proposed. For each of the samples taken into consideration for the investigation, the entire frequency band data is separated into subfrequency bands. The σ values calculated for the damage and healthy structure data's corresponding G and R subfrequency intervals. In Eq. 5.1, variables v_{gh} and v_{gd} are used to represent the difference in repeated healthy states ($h1$, $h2$) and damage-healthy (d, $h1$) data respectively for G. Similarly, variables v_{rh} and v_{rd} are used to represent the difference in repeated healthy states of ($h1$, $h2$) and damage-healthy (d, $h1$) data respectively for R.

$$v_{gd} = G_d - G_{h1}; v_{gh} = G_{h2} - G_{h1}; v_{rd} = R_d - R_{h1}; v_{rh} = R_{h2} - R_{h1} \tag{5.1}$$

Here, the variables v_{gd},v_{gh}, v_{rd} and v_{rh} are represented by the general notation A. The typical local maximum of the σ_A values in the σ_A-frequency plot is utilized to investigate the useful frequency range. The standard deviation for A is calculated using Eq. 5.2.

$$\sigma_A = \sqrt{\frac{\sum_{i=1}^{n} (A_i - \mu)^2}{n-1}} \tag{5.2}$$

where A_i represents i^{th} sample. The mean value (μ) of the A is calculated using Eq.5.3.

$$\mu = \frac{\sum_{i=1}^{n} A_i}{n} \tag{5.3}$$

The subject of attention is shown by the highest σ_A values taken from the G and R matching frequency band for the method's demonstration. Assume that σ_A is the value of a specific frequency subrange band η and that $\delta\sigma_A$ is the small change that corresponds to the frequency band's minor changes. Eq. 5.4 can be used to mathematically express the proper σ_A selection, which depends on the local maximum nature of these from the left and right side of the chosen frequency range η.

$$\frac{\partial \sigma_A}{\partial \eta} = \lim_{\delta n \to 0} \frac{\sigma_A(\eta + \delta\eta) - \sigma_A(\eta)}{\delta\eta} > 0 \tag{5.4}$$

In this section, the EMI-based damage detection methodology is illustrated using experimental data gathered from the two structures. Metal and composite are presented in the damage detection of experimental measurement for the demonstration of identifying the damages. In vast frequency ranges between 1kHz and 2MHz, data for aluminum and composite constructions were gathered in 200Hz increments, and the σ_A values were evaluated for a number of smaller bands. Although a smoother sample size will be time-consuming,

using 200Hz appears adequate for such a high-frequency range of damage analysis. Using an HIOKI IM3570 Impedance Analyzer, the experiments were carried out on the structures with attached piezo-actuators. The Ceramtec piezoelectric transducers made of SONOX P502 material had a 10 mm diameter disc form and were utilized for the EMI tests. The aluminum and composite plates are attached to the piezo-actuators using cyanoacrylate adhesive. In the testing, a 1V stimulation voltage was used. The chosen damage location falls within the PZT sensitivity range.

A small aluminum plate with drilled hole damage

A small aluminum plate with a hole drilled through it is used for the first analysis to show the frequency band selection. The study investigates the sensitivity of EMI responses produced by a single piezo-actuator to a 10 mm hole drilled in a small aluminum plate using the drilling technique shown in Fig. 5.1 on the aluminum plate. The dimension of the aluminum plate were 10 cm x 10 cm x 0.1 cm and the temperature of the room was maintained at constant $23^{\circ}C$ in the above experiment.

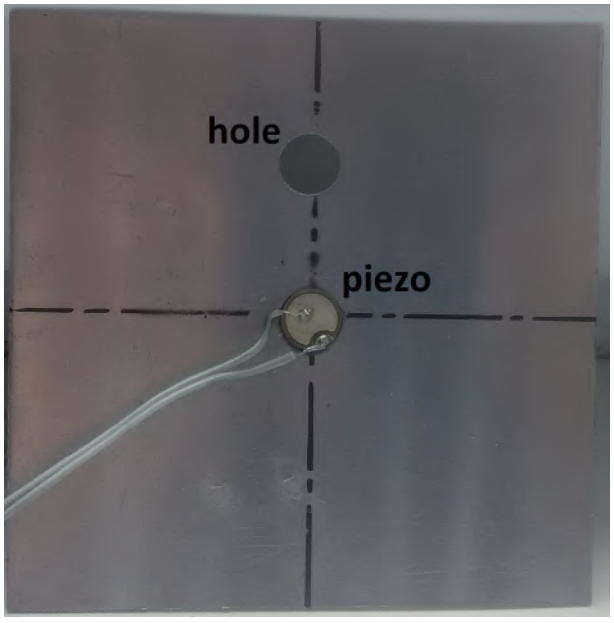

Fig. 5.1 Diagram of a small aluminum sample that was used to choose an appropriate frequency range and detect damage.

The full frequency range is divided into subranges (1, 2, 3, 4,... 28) of the appropriate band at a frequency of roughly 70 kHz in this data-driven approach. Due to the fact that the G and R to maximum 70-80 kHz range was employed for the majority of research on damage sensitivity in EMI [122–124]. Then σ values were determined for each frequency

band of G and R. The area of interest was explained by the local maximum deviation in the damaged and healthy sub-frequency bands. The σ_A subranges plot for the effective frequency range analysis is given in Fig. 5.2 and Fig. 5.3. The frequency sub-bands 9^{th}, 12^{th}, 19^{th}, 23^{rd} exhibit the shared local maxima of σ_A, hence these values are chosen for the sensitivity analysis. The plot of σ_A is estimated for repeated measurements of the healthy state using v_{gh} and circular hole damage state concerning the healthy state by v_{gd}. Similarly, for R data, v_{rh} is used for repeated measurements of the healthy state, and v_{rd}, for the damage state.

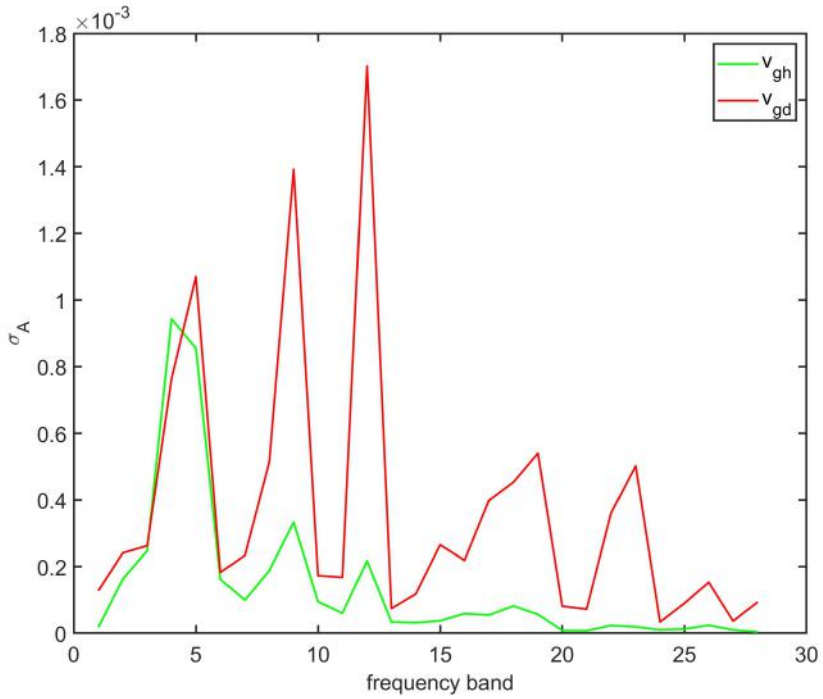

Fig. 5.2 Sensitivity model parameters using σ_A values based on the G in the aluminum plate's frequency sub ranges.

Study of added mass on GFRP plate

In the second research, a study of the composite sample's σ values under an added mass damage scenario is done. The picture of the investigated samples is shown in Fig. 5.4 having magnets on the GFRP plate. The magnet is moved from the location "c" in the center to the side location "s" of the square structure of side of the 50 cm by 50 cm and thickness 0.5 cm which is midpoint of actuator 2 and 3.

The frequency range is separated into subfrequency ranges of the suitable band at a distance of around 70 kHz, same like in previous section. Then, using the healthy and damaged states, σ_A values were determined for each frequency sub-range. The point of

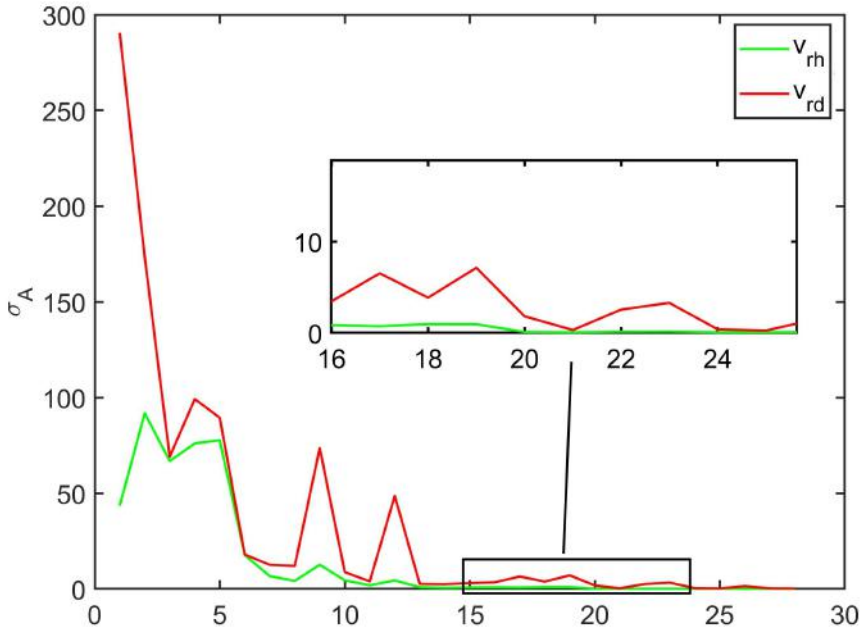

Fig. 5.3 Sensitivity model parameters using σ_A values contingent on the R in the frequency sub ranges of the aluminum plate.

interest was explained by the local maxima in the damaged and healthy sub frequencies. The σ_A subranges plot for the effective frequency range analysis can be given by Fig. 5.5 and Fig. 5.6. In the square layout of the piezo-actuators 1, 2, 3, and 4 on the GFRP plate, $v_{gh}1$ symbol used for repeated measurements of the healthy state, $v_{gd}c$ and $v_{gd}s$ represent simulated mass damage at the center and side 2-3 concerning healthy state using G data. Similarly, for R data, $v_{rh}1$ is used for repeated measurements of the healthy state, $v_{rd}c$, and $v_{rd}s$ for the damage state. The 4^{th} and 9^{th} frequency band shows the local maxima for the σ_A as can be seen from Fig. 5.5 and Fig. 5.6.

5.3 Fusion-based probabilistic methodology

This work introduces the integration of the Gaussian probability density function to more precisely identify damage location and damage severity. Integrating the Gaussian probability density function for the G and R variables in the usable frequency range will aid in deriving reliable information from frequency domain data so that damage detection can be improved through robust decision-making. The technique is beneficial for pinpointing the location of damage and determining the damage severity level. By introducing a damage algorithm and a statistical matching strategy for a chosen frequency range, the scope of data fusion in the EMI technique is expanded to allow for the quantification of damage and undamaged health

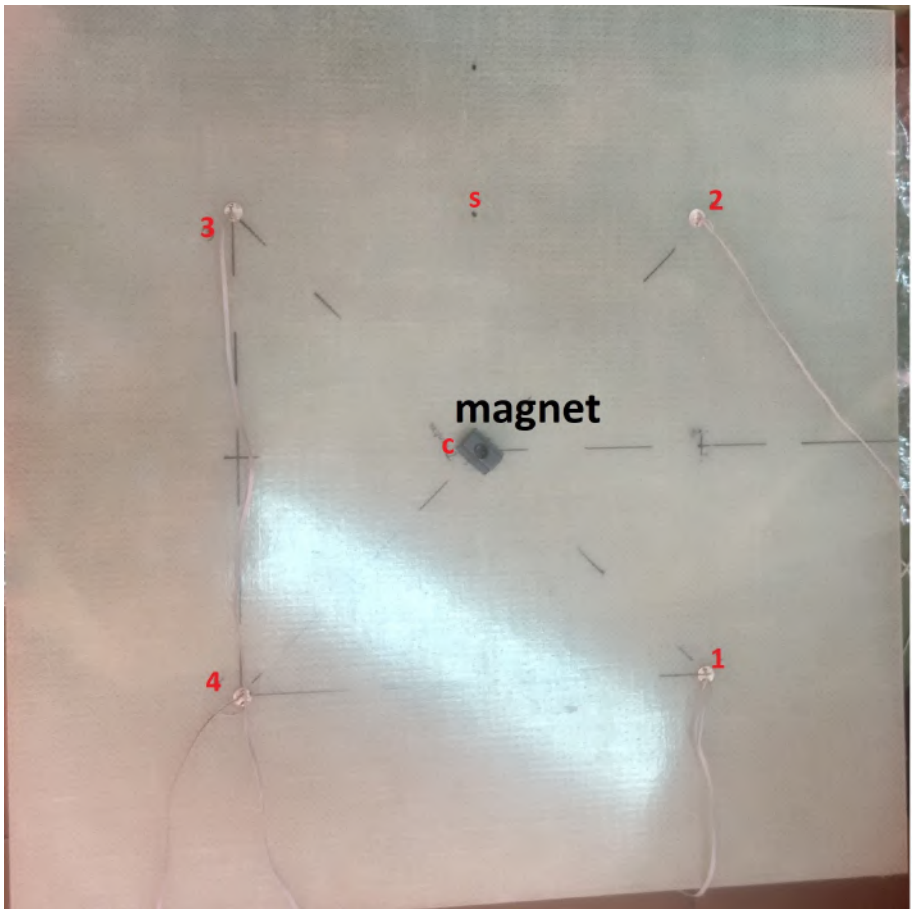

Fig. 5.4 Diagram of composite samples used to test frequency range selection approach for damage detection.

conditions of isotropic material and anisotropic plates. The EMI-based SHM technique is the first to apply a few probability-based data fusion techniques, despite the fact that there has been a lot of work done on data fusion. The Bayesian probability framework, which depends on prior probabilities and model selections and is suitable for assessing structural damage, is studied by the authors [125–127]. However, the major goal of **this** research is to create a more accurate damage identification tool. This methodology expanded the possibilities for damage indices and broadened the study's scope for damage classification and detection via data fusion. With this strategy, data fusion for various EMI factors is flexible. Similar to Chapter 3, this one attempts to gauge the severity of damage by combining data from variables with different natures (G and R) and those with similar natures (Y and G) to create a PCA projection-based damage index.

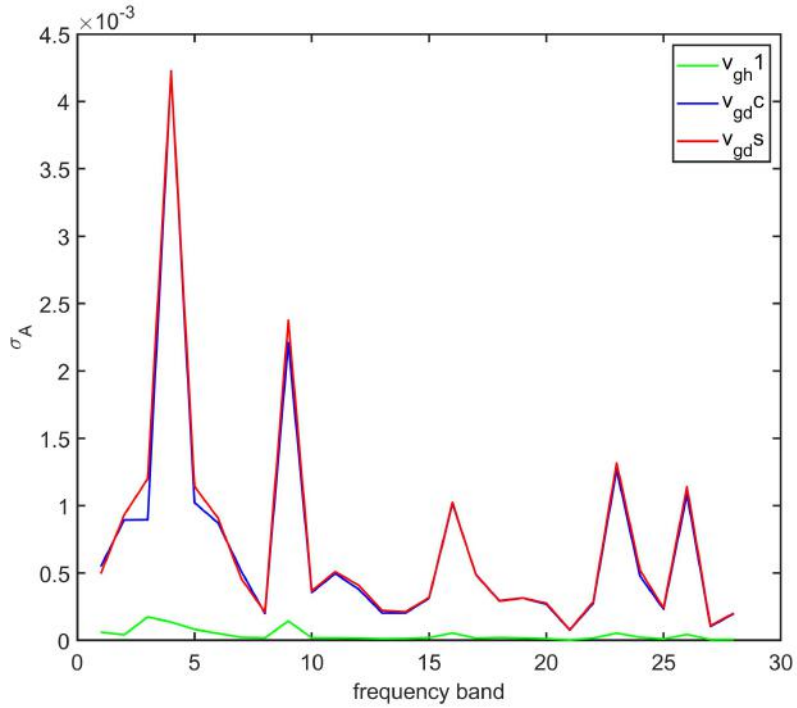

Fig. 5.5 Sensitivity plot of the G data in the frequency sub ranges of the GFRP plate using σ_A values.

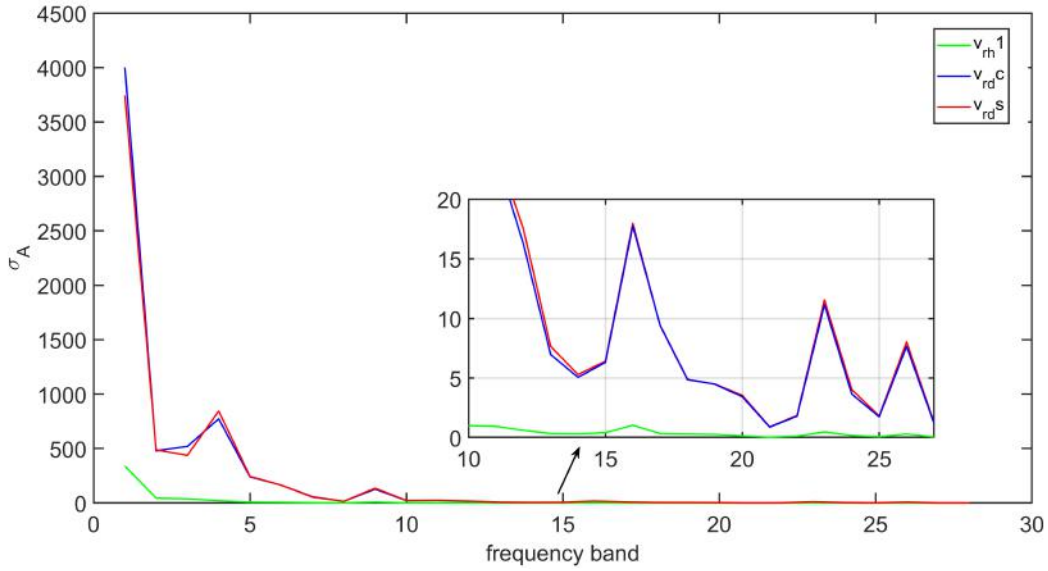

Fig. 5.6 Sensitivity plot of the R in the frequency sub ranges of the GFRP plate using σ_A values.

The work demonstrates the data fusion to achieve a common damage index for the G and R EMI variables. The methodology provides a thorough explanation of the process and uses this set of steps to illustrate it.

- Step 1: Calculation of v_{gd}, and v_{rd} variables from EMI measurements.
- Step 2: Selection of the frequency range using the σ_A values of v_{gd}, v_{gh}, v_{rd}, and v_{rh}.
- Step 3: Calculation of the maximum and minimum limit for the v_{gd}, and v_{rd} variables in the selected frequency range.
- Step 4: Formation of the probability density function (pdf) $p1$ and $p2$ using the mean and the standard deviation of the healthy and damaged state of the structure.
- Step 5: The new C-index damage index is investigated using the effective frequency band.

For each sample, the G and R are experimental EMI measurements. The structural measurements' subscripts "h" and "d" stand for the healthy and damaged states, respectively and hence the healthy state data for conductance and resistance are G_h, and R_h, respectively. The structure's conductance and resistance damage states are represented by the variables G_d, and R_d, respectively. Then a probabilistic way to represent the distribution of the healthy and the damaged state of the variable A is given by Eq. 5.5 [128].

$$p(\frac{A_i}{\sigma_A}, \mu) = \frac{1}{\sigma_A \sqrt{2\pi}} \exp\left(-\frac{1}{2}\left(\frac{A_i - \mu}{\sigma_A}\right)^2\right) \tag{5.5}$$

A Gaussian likelihood function (pdf) for the G and R variables describes the true value of the parameter of interest using Eq. 5.5. The probability of the G and R healthy and damaged data of a particular frequency band lying within deviation range of minimum (min) to maximum (max) can be obtained in numerical value. Eqs 5.6 and 5.7 can be used to get the numeric probability of area difference for these healthy and damage-related variables.

$$p1 = \int_{min}^{max} p(\frac{G_d}{\sigma_{gd}}, \mu_{gd})\, dG_d - \int_{min}^{max} p(\frac{G_h}{\sigma_{gh}}, \mu_{gh})\, dG_h; \tag{5.6}$$

$$p2 = \int_{min}^{max} p(\frac{R_d}{\sigma_{rd}}, \mu_{rd})\, dR_d - \int_{min}^{max} p(\frac{R_h}{\sigma_{rh}}, \mu_{rh})\, dR_h; \tag{5.7}$$

dG_d, dG_h, dR_d and dR_h represent infinitesimal small deviations in the corresponding G and R variables' health status of the structure in Eq.5.6 and 5.7. The mean and standard

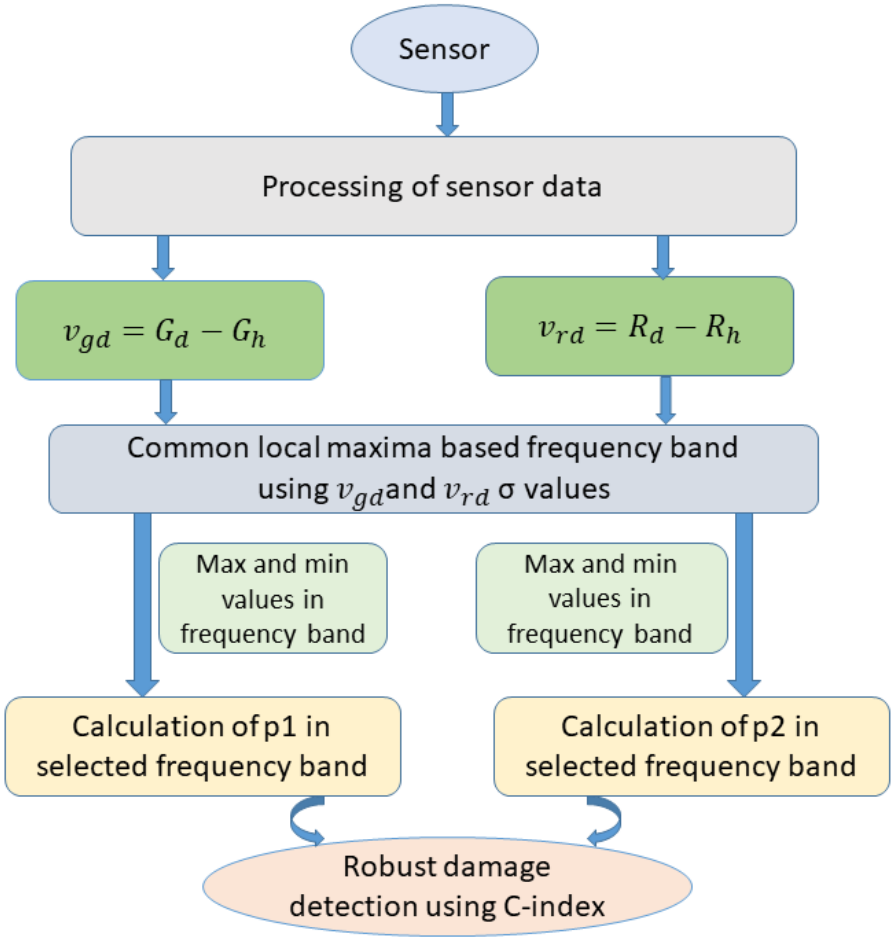

Fig. 5.7 An illustration of the damage detection procedure using the samples' C-index.

deviation of the healthy and damaged state of G and R are μ_{gd}, μ_{gh}, μ_{rd}, μ_{rh}, σ_{gd}, σ_{gh}, σ_{rd} and σ_{rh} respectively.

The fusion of the G and R variable's derived features used two probabilistic estimates based on the Gaussian distribution function. The G and R spectral analysis is viewed as an independent event in this equation, which has two variables. The C-index is a statistical damage index that uses the G and R EMI variables. Eq.5.8 provides the developed mathematical index expression [129, 130]. The method integrates the p1 and p2 values in the effective frequency range after transforming the G and R data using the Gaussian probability density function.

$$C - index = \frac{p1p2}{(p1p2) + (1-p1)(1-p2)} \tag{5.8}$$

Data fusion has been applied at the highest level in the equation above by directly combining the p1 and p2 processed data using Eq.5.8, which serves as the primary statistical index in EMI. The Gaussian probability function is utilized in the equation to estimate G and R EMI variables within a specific frequency range. This methodology has the benefit over others in that it only considers the data between the damaged and healthy states and simultaneously combines the deviation of two variables, G and R. Hence the approach may provide reliable damage detection because it covers all deviated areas between healthy and damaged states. The schematic flow chart diagram of the selected single-frequency band based damage detection procedure is given in Fig. 5.7 for the metal and composite samples.

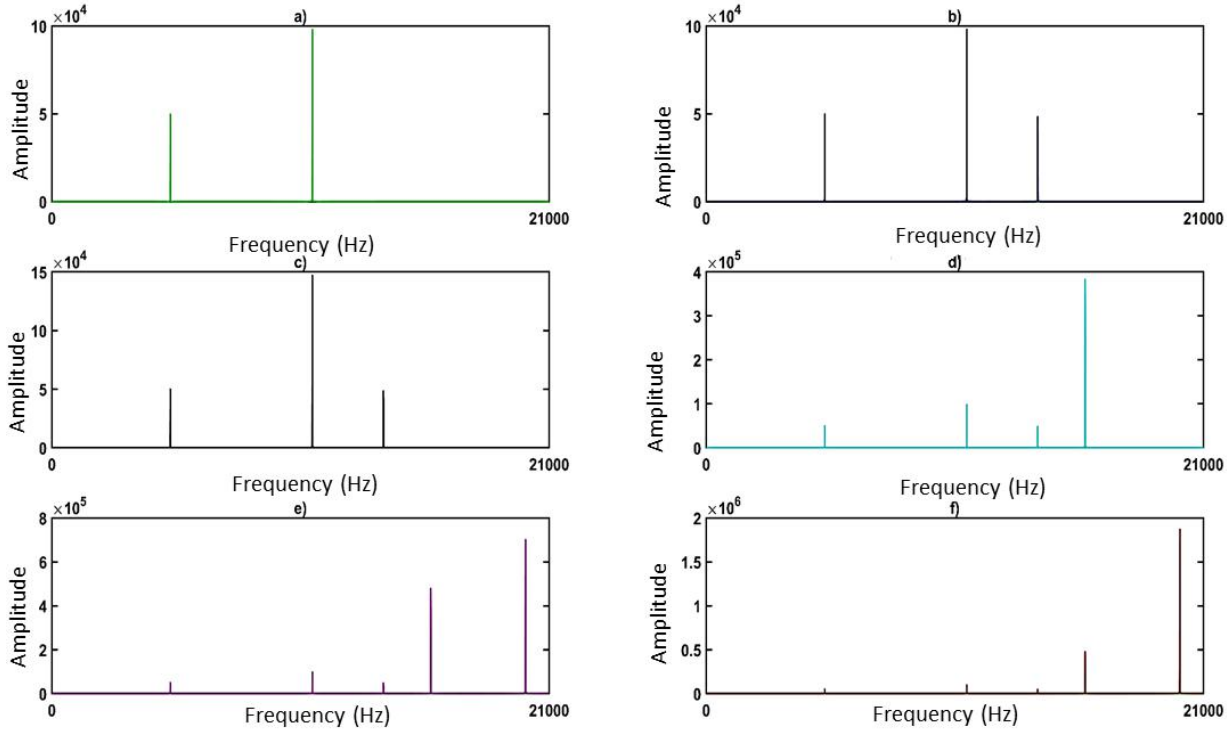

Fig. 5.8 Analytical signal spectra at the following points: a) baseline, b) amplitude increases, c) with the addition of perturbation, d) with peak intensity, e) new perturbation and f) increase in the amplitude of new peak.

5.3.1 C-index sensitivity study using analytical spectra

Using the numerical data generated from the fast Fourier transform (FFT) of the time domain sine function, this section of the thesis illustrates the EMI-based damage detection methodology. The sensitivity of the aforementioned method was examined using this analytical signal, where modifications are made by amplifying already-existing peaks or by

adding new peaks. A horizontal shift is a change in frequency, whereas a vertical shift is an increase or decrease in amplitude. New peaks have been added to the original signals, and some of the existing peaks have had their magnitudes along the frequency axis changed. Fig. 5.8a depicts the analysis's baseline signal, and Fig. 5.8b depicts the frequency axis after a perturbation has been applied. Before a perturbation is added in Fig. 5.8d, the amplitude's size increases in Fig. 5.8c. One additional new peak is added to the preceding signal in Fig. 5.8e, and in Fig. 5.8f, the intensity rises for the same disturbance.

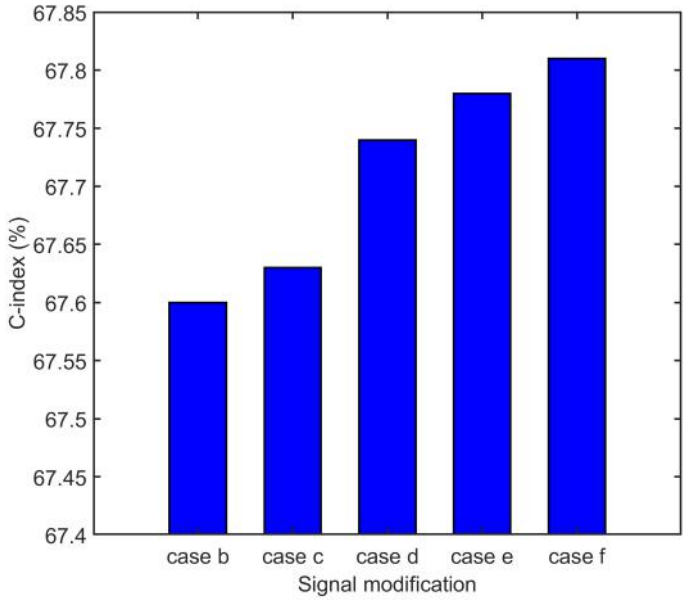

Fig. 5.9 Calculation of the C-index for the analytical spectra.

The C-index of the change in magnitudes of new peaks and introduction of the peaks shown in Fig.5.9. The b & c case study the damage index by a change in the amplitude with respect to healthy state 'a'. The c & d case study the increase in peak intensity and new perturbation together with respect to 'a'. The d & e case, study the increase in number of perturbation only with respect to 'a'. The e & f case, study the increase in peak intensity of new perturbation with respect to 'a'. The findings show that the C-index is a reliable damage index for any damage alterations made to the original signal.

5.3.2 C-index sensitivity study for metal and composites

This section includes an analysis of the damage location and severity for the sensitive sensor using an efficient frequency range and the recommended C-index. The statistical C-index, which is based on a probability density function, is assessed in the appropriate sub-frequency

bands to help identify defects using sensors and gauge the extent of the damage. Small and large aluminum plate, and GFRP composite structure experimental data were collected in the 1kHz–2MHz frequency range. There may be multiple peaks for such a high frequency, some of which will match the inherent frequency of the plate. Since 1 volt of stimulation is insufficient to excite all of the plate's modes due to the size of this aluminum and GFRP plate.

C-index study for small aluminum plate

The frequency sub-bands 9^{th}, 12^{th}, 19^{th}, 23^{rd} used to estimate C-index and RMSD index for the small aluminum plate as discussed in the earlier section and displayed in Fig.5.2 and Fig.5.3. Eqs. 1.4, and 5.8 are used to determine the RMSD index and C-index respectively. The C-index, however, performs better in the higher frequency ranges. All local maxima frequency sub-bands of the broad frequency range have undergone investigation.

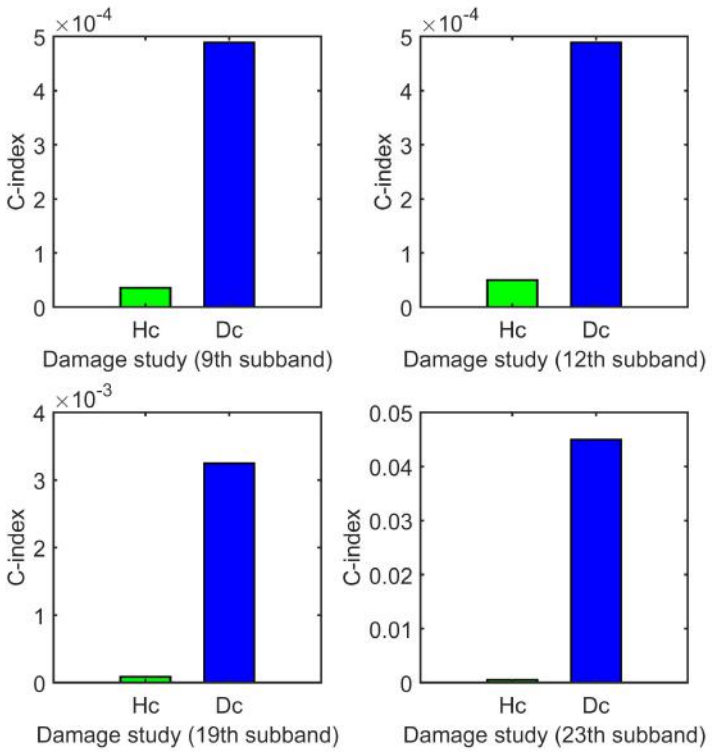

Fig. 5.10 C-index for the healthy and damaged aluminum plate in the frequency sub-bands: a) 9^{th} , b) 12^{th} , c) 19^{th}, and d) 23^{rd} respectively.

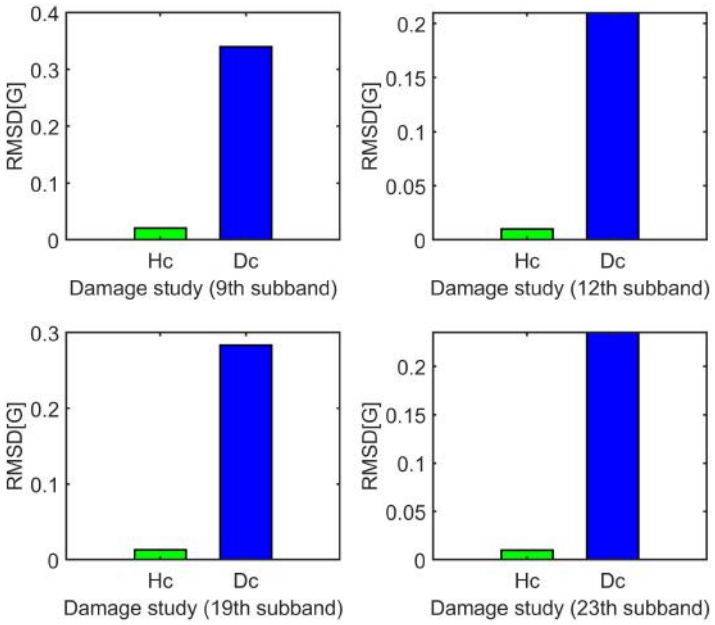

Fig. 5.11 RMSD index for the healthy and damaged aluminum plate in the following frequency sub-bands: a) 9^{th} , b) 12^{th} , c) 19^{th}, and d) 23^{rd} respectively.

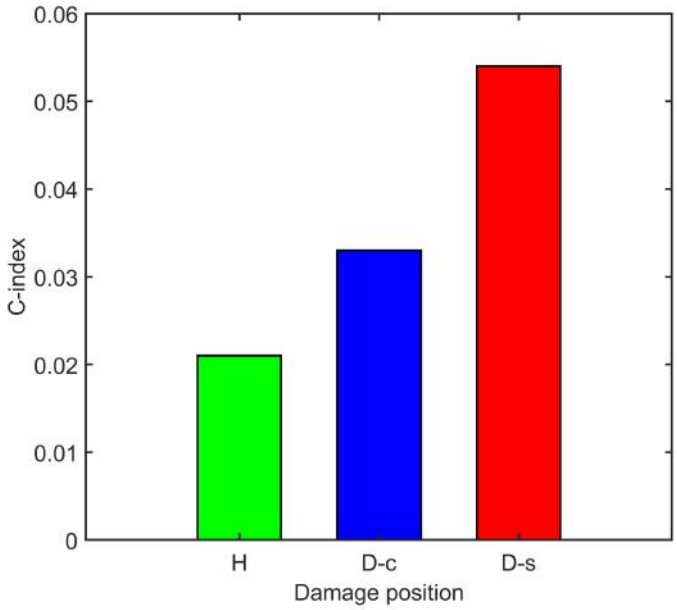

Fig. 5.12 C-index of the GFRP plate's structures in the effective 9^{th} frequency sub band.

C-index study for GFRP plate

The C-index performance analysis has been done in the 9^{th} frequency subband which has shown a well seperated increasing trend for σ_A parameters as the mass is moved from the

centre of the square structure to the midpoint of the side 2-3 of the piezo-actuators in the GFRP plate. This method shows sensitivity for lighter damage than traditional RMSD methods because it uses pdf transformations of the raw data and fuses two variables as shown in Fig. 5.12. However, in the same frequency subband, the RMSD index of G and R signatures do not show any sensitivity as shown in the Fig. 5.13.

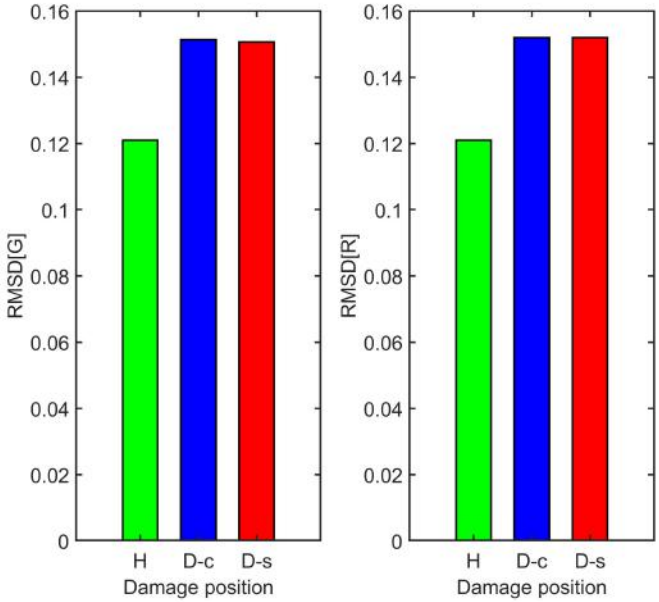

Fig. 5.13 RMSD index in effective 9^{th} frequency sub band of the GFRP plate.

Damage severity study of metallic structure

The EMI experimental study was performed on a thin square aluminum plate with an attached piezo-actuators network as shown in Fig. 3.10. The locations of piezo-actuators in the network are a result of different studies with an optimization approach for guided wave-based damage detection as described in Chapter 3 [131]. To assess the degree of damage, the sensor P1, which is set at a distance of 22.36 cm from the hole "D-a," is employed only. This study examines the sensitivity of EMI responses to two different sizes of drilled holes in an aluminum plate: a 5 mm hole and a larger, 10 mm hole. As illustrated in Fig. 3.10 on the plate, the hole was made using a drilling operation and then it was extended up to 10 mm. The plate has the following measurements: 100 x 100 x 0.1 cm^3 and the temperature of the room was kept constant at 23°C in the above experiment.

According to research done in Chapter 3, the piezo-actuator P1 demonstrated the maximum sensitivity to the damage caused by the hole made on the aluminum plate. To illustrate

the development of the algorithm, the frequency domain analysis of the EMI G and R spectra for the healthy and damaged states of the aluminum plate for P1 is performed. The algorithm for calculating the damage index in the effective frequency range is being developed with a primary focus on the hole 'D-a' in Fig. 3.16. Fig. 5.14 illustrates the G spectra of piezo-actuator P1 in both its healthy and damaged states. An efficient frequency approach based on σ values was used to choose the optimal frequency range (530-600 kHz). The model for damage detection and classification is illustrated using this range. For the 5mm and 10mm drilled holes, the piezo actuator P1's RMSD index is displayed in Fig. 5.15. The threshold limit established for the P1 for damage detection is known from the other repeated measurements in the healthy condition. The index is generated from the two measurements in each case of the features G and R. In order to determine the degree of the damage in the large aluminum structure, an RMSD index was computed using Eq. 1.6. From Fig. 5.15, it is clear that for the 5mm and 10mm holes, the RMSD index does not show an upward trend.

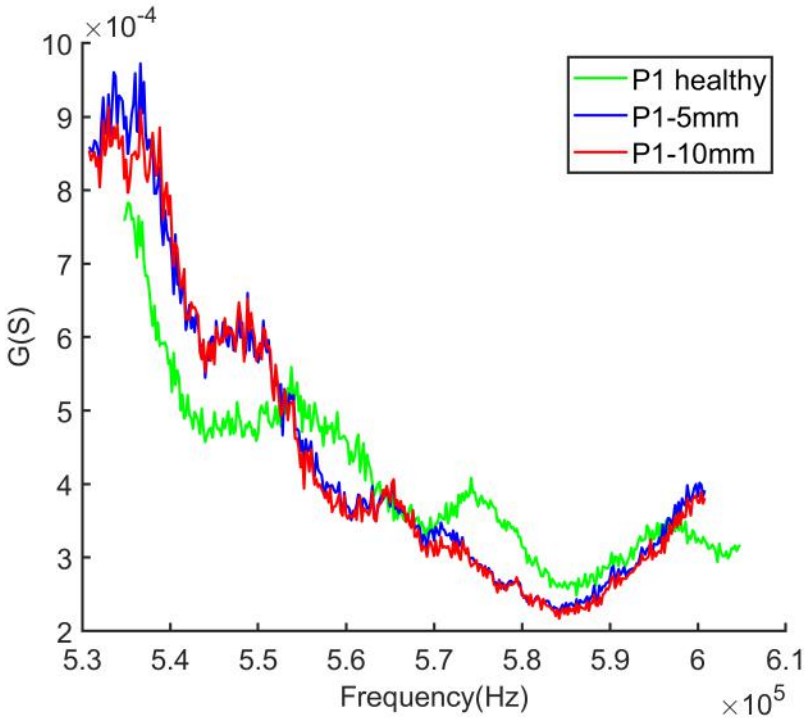

Fig. 5.14 The sensor P1's G spectrum plot for holes measuring 5 and 10 millimeters.

Fig. 5.16, Fig. 5.17 and Fig. 5.18 displays the pdf plot of two repeated measurements of the healthy state in relation to various damage severity cases. According to table 5.1, the bell-shaped width range utilizing the minimum (A) and maximum (B) of G and R increases with the degree of damage. The standard deviation values for the P1 healthy and damaged states are also shown in Table 5.1.

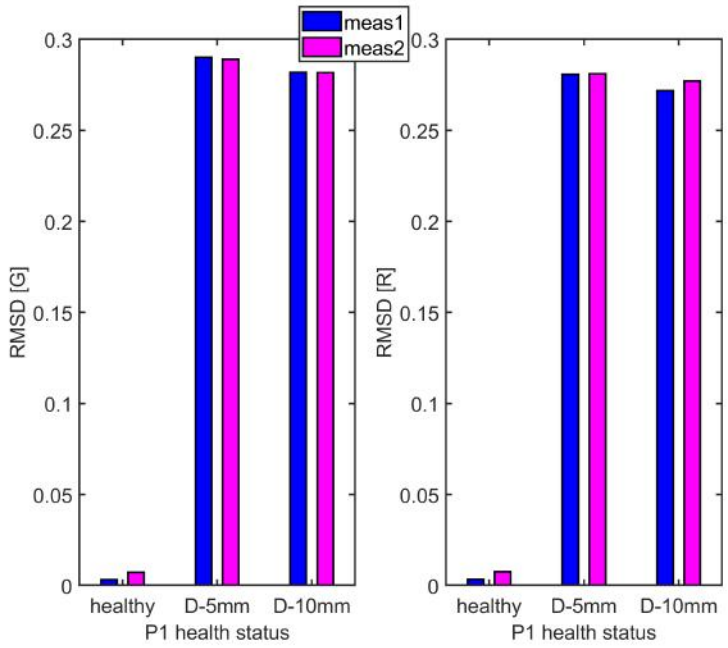

Fig. 5.15 a) G and b) R sensor network RMSD damage indices for 5 mm and 10 mm holes drilled in a large aluminum plate.

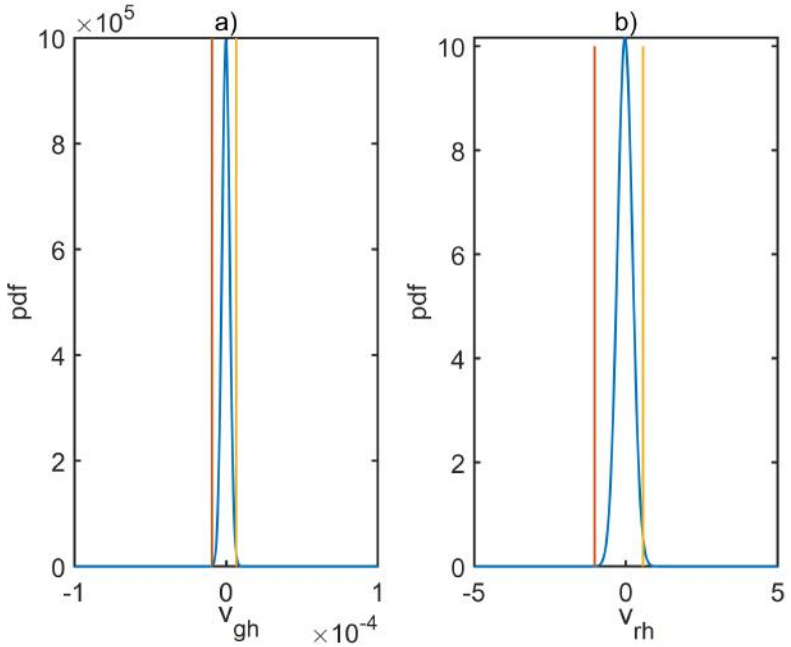

Fig. 5.16 The pdf curve of healthy state's a) v_{gh}, and b) v_{rh} variables.

Due to the maximal variations in the EMI response following structure degradation, the width of A to B values (indicated by vertical lines) in the pdf plot also grows. The likelihood

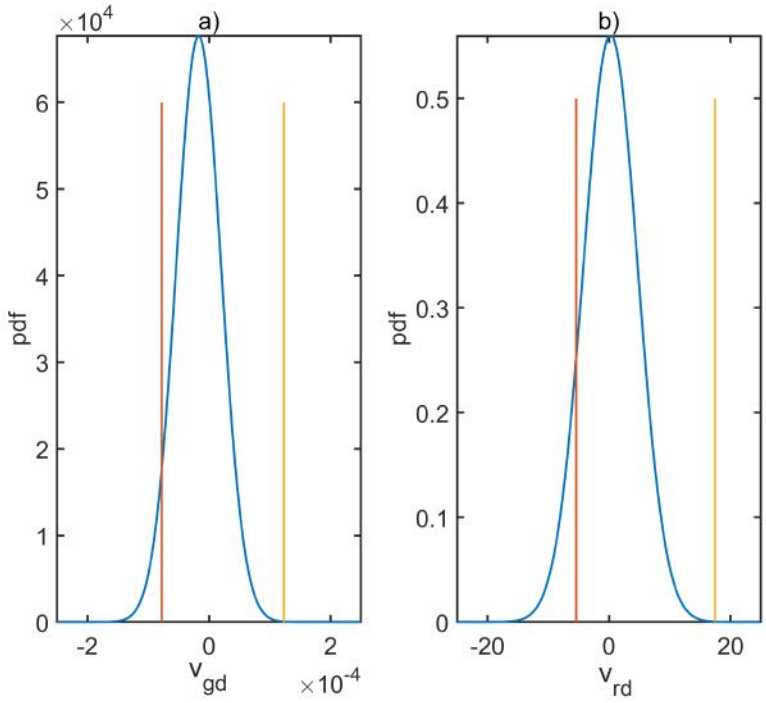

Fig. 5.17 The pdf curve of a) v_{gd}, and b) v_{rd} variables for the 5mm damage state.

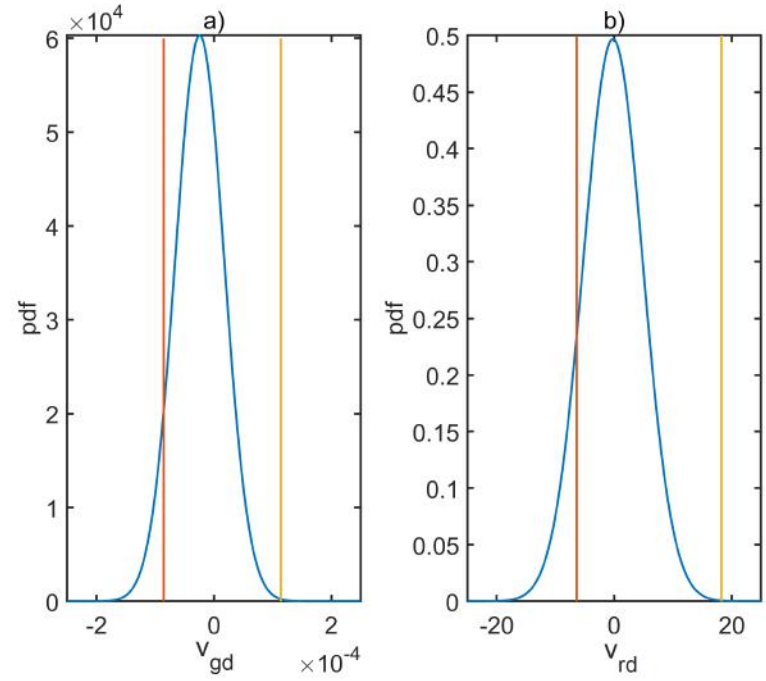

Fig. 5.18 The pdf curve of a) v_{gd}, and b) v_{rd} variables for the 10 mm damage state.

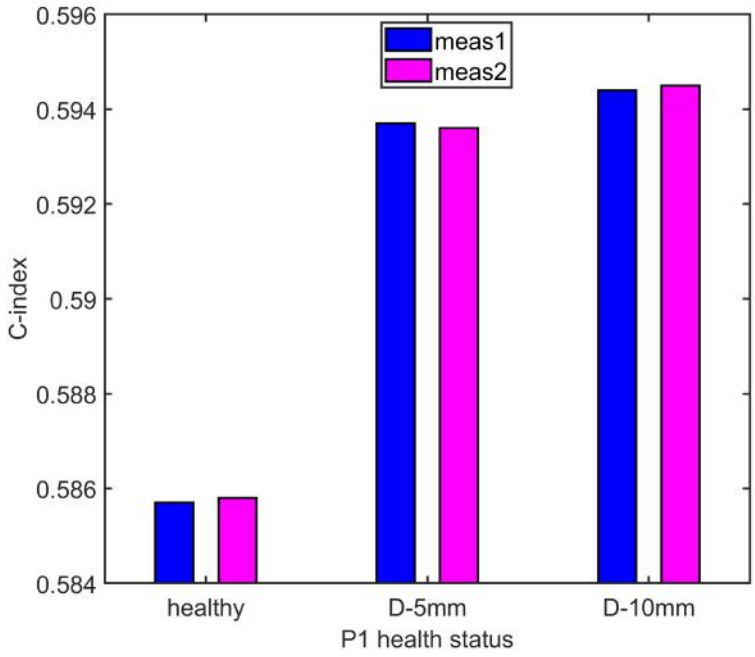

Fig. 5.19 C-index of piezo P1 for the damage of 5 mm and 10 mm drilled holes in the large aluminum plate.

Table 5.1 Summary of P1 healthy and damaged state statistically.

	Healthy state repeated measurement		5 mm-hole		10 mm-hole	
	G(S)	R(Ω)	G(S)	R(Ω)	G(S)	R(Ω)
σ	0.12×10^{-5}	0.12	3.7×10^{-5}	4.47	4.17×10^{-5}	5.05
A	-0.39×10^{-5}	-0.436	-7.79×10^{-5}	-5.39	-8.6×10^{-5}	-6.38
B	3.09×10^{-5}	0.4	1.23×10^{-4}	17.45	1.14×10^{-4}	18.27

of a bell-shaped curve is higher if the two curves (Gh and Gd or Rh and Rd) share the same perturbation or horizontal shift. However, there is less chance of identifying the same place within the cell if there is curvature fluctuation. The width of the A to B values in the pdf also grows as it contained the maximum changes in the spectrum after damage in the structure. For the 10 mm hole, the breadth range in the pdf of the G and R variables is greater than for the 5 mm hole. It is also obvious that the combined effort of the G and R variables is what causes the C-index for the 5 mm hole and 10 mm hole damage. Since the spectrum typically has several data points above and below to represent the healthy condition and damaged state, it can be challenging to determine which region is crucial for comparison. However, by utilizing this technique, we are able to identify the p1 and p2's dominant effects. Eq. 5.8 is used to determine the C-index performance for the P1 in each scenario, and the results are

displayed in Fig. 5.19. It is evident from the figure that the degree of damage for the C-index of P1 in the large aluminum plate is on an increasing trend.

For the most sensitive piezo actuator P1, the effective C-index incorporating G and R variables was compared to conventional RMSD. For the variables G and R damage severity assessment, the C-index has demonstrated an increasing tendency for 5 mm and 10 mm diameter holes than the classic RMSD index.

Study of GFRP composite plate

The EMI planned calibration experiments were performed on a square thick GFRP composite plate using a square network consisting of four sensors used to measure the signatures at the piezoelectric transducer terminals. The damage was introduced by an impact at the energy of 30 J with a projectile with a spherical end. The GFRP plate of dimension 50 cm x 50 cm x 3 cm made of 8 layers of woven GFRP. Moreover, during the manufacturing stage of the sample another damage was simulated by introducing a thin Teflon patch (10 mm x 10 mm) between 2nd and 3rd layer of the composite just in the area where later piezo actuator no. 1 was positioned as discussed in Fig. 3.2 of chapter 3. The point ‘g’, ‘h’, and ‘k’ in Fig. 5.20 marks the introduced damage positions.

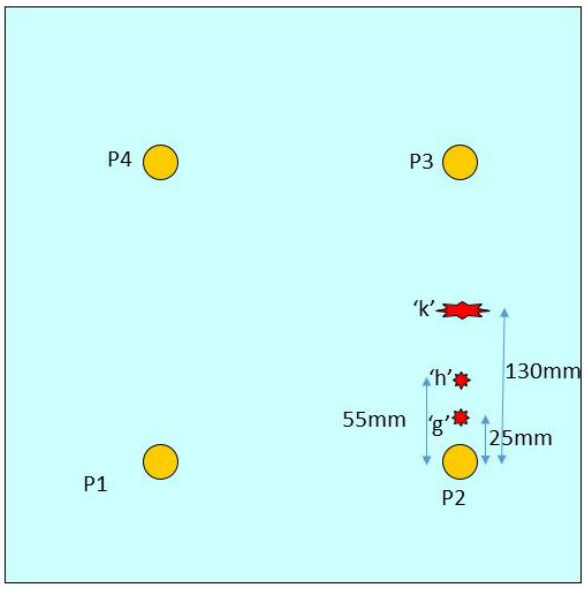

Fig. 5.20 GFRP plate with impact damage shown in diagram.

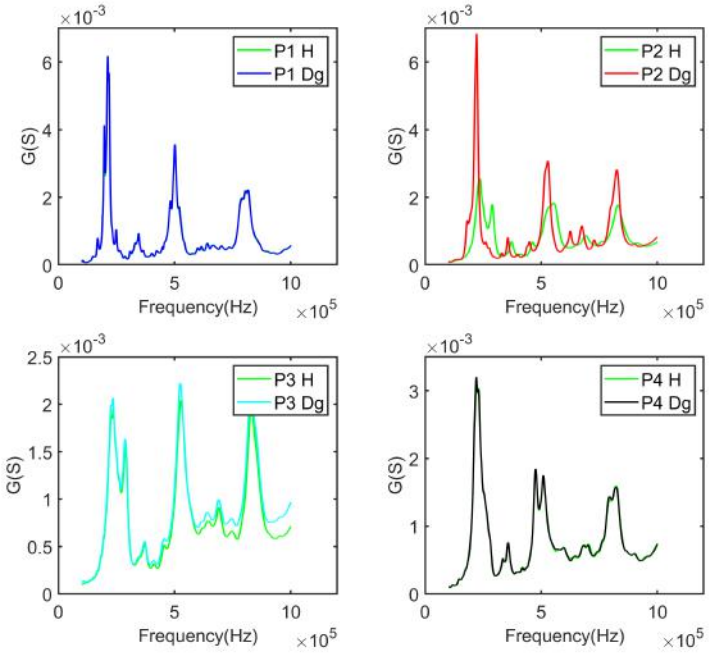

Fig. 5.21 The sensor P1, P2, P3, and P4's G spectrum displayed on a GFRP plate.

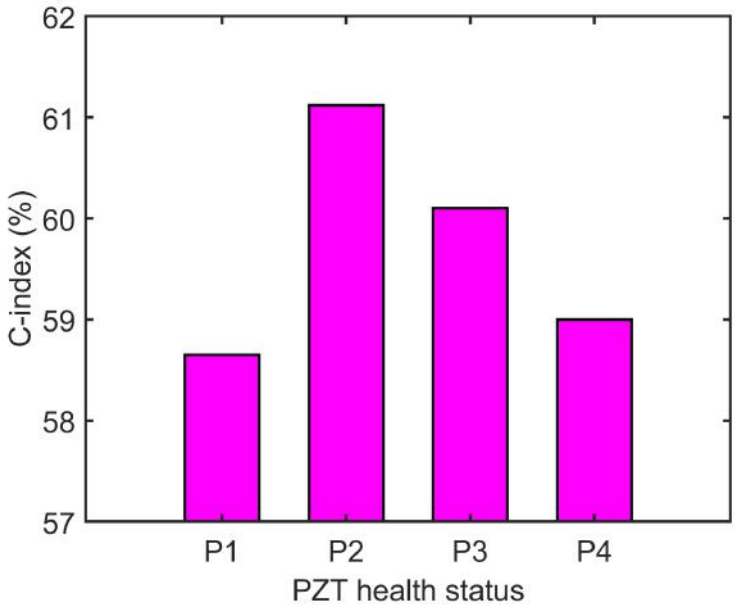

Fig. 5.22 The sensor network's C-index following the impact at composite plate point "g".

Study of impact damage location using sensor network on a composite GFRP plate

This part explains the damage sensitivity for P2 in a frame of sensor network contribution. The conductance plot for P1, P2, P3 and P4 are shown in Fig. 5.21 after impact at a position of

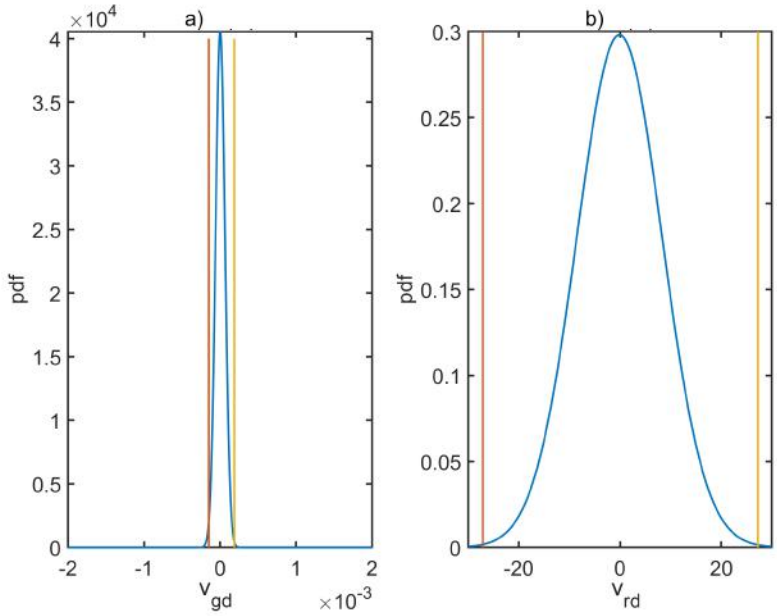

Fig. 5.23 Variables a) v_{gd} and b) v_{rd} pdf distribution diagram for P1 following the impact of damage "g".

'g'. The C-index for the all piezo-actuator was calculated in the frequency range of 170-250 kHz, which is an effective frequency range as obtained using σ values. The piezo-actuator P1, P2, P3 and P4 individual behaviour has shown for the variables R and G variables through the combined C-index in Fig. 5.22. The high sensitivity for the P2 is due to damage impact close to the piezo-actuator. The second highest sensitivity is shown by the P3, due to the second nearest to the impact damage.

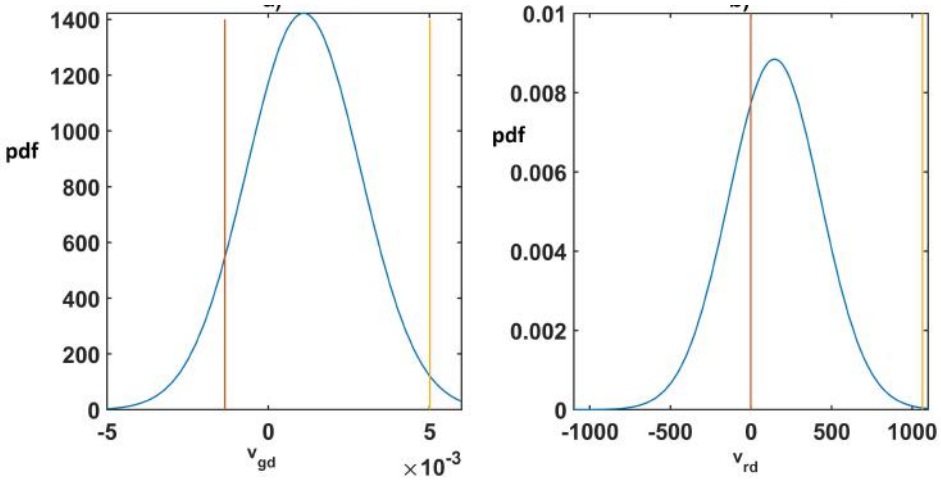

Fig. 5.24 Variables a) v_{gd} and b) v_{rd} pdf distribution diagram for P2 following the impact of damage "g".

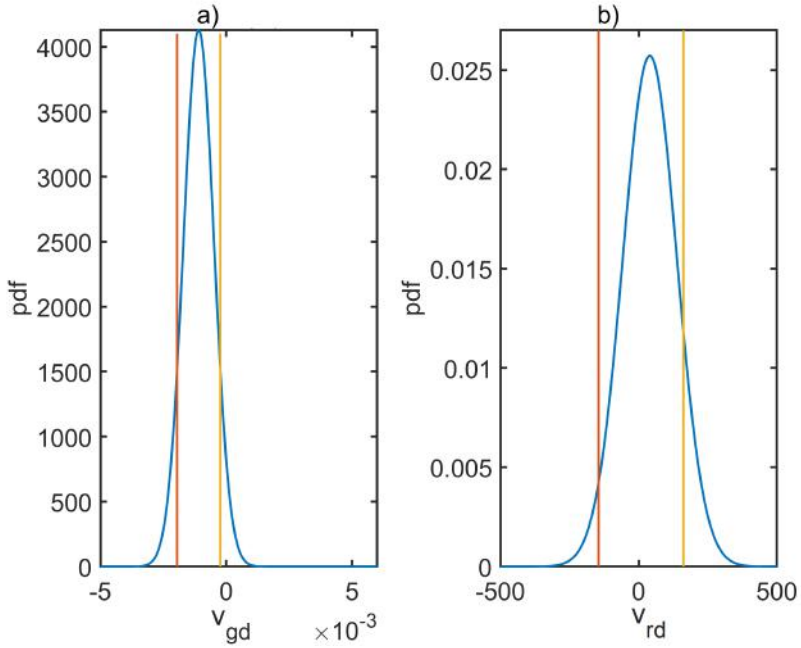

Fig. 5.25 Variables a) v_{gd} and b) v_{rd} pdf distribution diagram for P3 following the impact of damage "g".

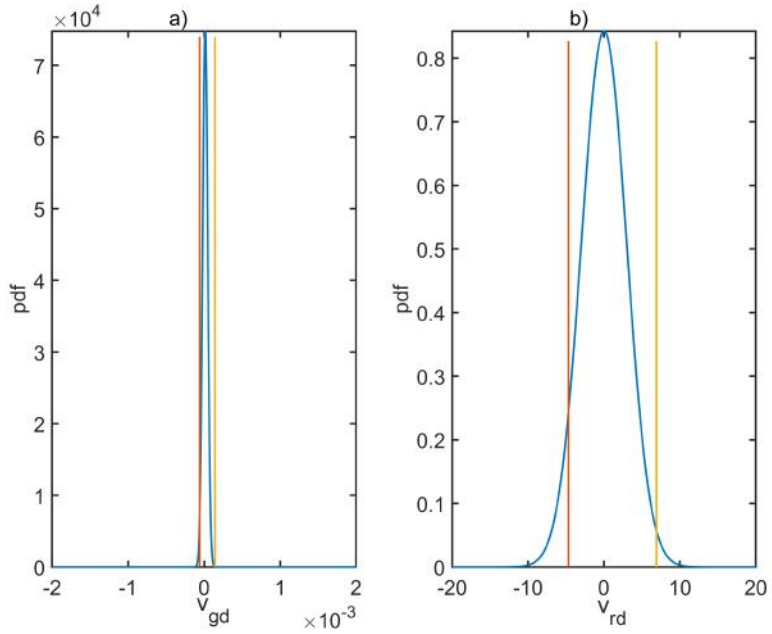

Fig. 5.26 Variables a) v_{gd} and b) v_{rd} pdf distribution diagram for P4 following the impact of damage "g".

The pdf plot of P1, P2, P3 and P4 are shown in Fig. 5.23, Fig. 5.24, Fig. 5.25, and Fig. 5.26 respectively for the impact damage location ‘g’. The bell-shaped pdf response gets

flattened for the P2, which is nearest to the damaged location. The pdf demonstrates the highest deviation of P2 and lowest of P1 out of A and B limits. However, C-index for the P1 is minimum and cover a higher range than P4 for the G and R variables in the minimum and the maximum deviation range. The dominating effect of the p1 and p2 values is higher for the P1 even though the standard deviation value is greater for the P1 compared to P4 as shown in table 5.2. This shows that the sensitivity of this method is limited to some extent.

Table 5.2 Standard deviation and width data for the sensor network after impact at location 'g'.

	P1		P2		P3		P4	
	G(S)	R(Ω)	G(S)	R(Ω)	G(S)	R(Ω)	G(S)	R(Ω)
σ	6.18×10^{-5}	8.4	140×10^{-5}	270.1	60.7×10^{-5}	97	3.35×10^{-5}	2.98
A	-1.5×10^{-4}	-27.1	-0.0013×10^{-5}	-1.67	-0.002	-145.1	-5.81×10^{-5}	-4.66
B	1.9×10^{-4}	27.3	0.005	1063	-2.3×10^{-4}	161.6	1.41×10^{-4}	-6.93

Study of impact damage severity on composite GFRP plate

In this case, the piezo-actuator P2 was used to examine the structure's health following each impact from the damage. According to Fig. 5.20, the impact location in the composite structure is shifting from 'k' to 'g'. The frequency spectrum plot for all piezo-actuator is given in Fig. 5.27. The closest impact to the P2 allows the biggest data fluctuation, as seen in Fig. 5.27. The P2 was used to show damage location detection in the 170-250 kHz frequency band using the Gaussian distribution function. The P2 is examined using a C-index approach under various damage impact conditions ('g', 'h', and 'k'). However, the index value is lowest for the repeated measurement and highest for the closest hit, as seen in the Fig. 5.28.

Table 5.3 Standard deviation and width data for P2 after impact at 'g','h','k' damaged cases.

	Healthy state repeated measurement		impact at 'g'		impact at 'h'		impact at 'k'	
	G(S)	R(Ω)	G(S)	R(Ω)	G(S)	R(Ω)	G(S)	R(Ω)
σ	0.58×10^{-5}	0.2728	140×10^{-5}	270.1	3.86×10^{-5}	2.9	1.46×10^{-5}	1.22
A	-02.33×10^{-5}	-1.65	-0.0013	-1.67	-1.59×10^{-5}	2.24	-1.1×10^{-5}	-2.0
B	-6.25×10^{-7}	-0.43	0.005	1063	1.33×10^{-4}	11.8	4.14×10^{-5}	3.4

From Fig. 5.29, Fig. 5.24, Fig. 5.30 and Fig. 5.31, as the position of the impact damage moves farther from the P2, we can see that the bell-shaped curves of the G and R are becoming less flat. The mean, standard deviation, A and B values are indicated in table 5.3 for examining the degree or location of damage in calculated frequency range. The majority of the P2's variance is covered by the healthy state pdf curve in the A and B limits. As a result, it accounts for the majority of deviation in the bell-shaped curve, and the likelihood of

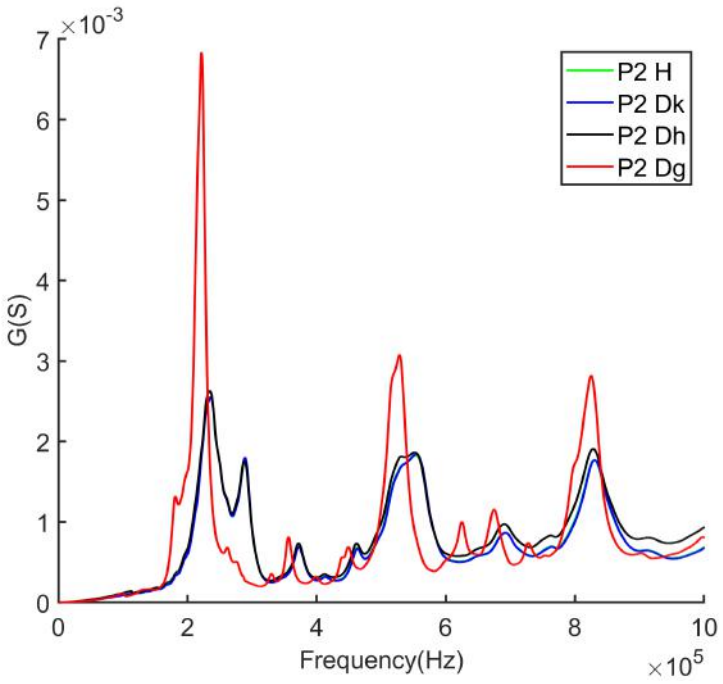

Fig. 5.27 The G spectrum plot of the sensor P2 after each impact on the GFRP plate.

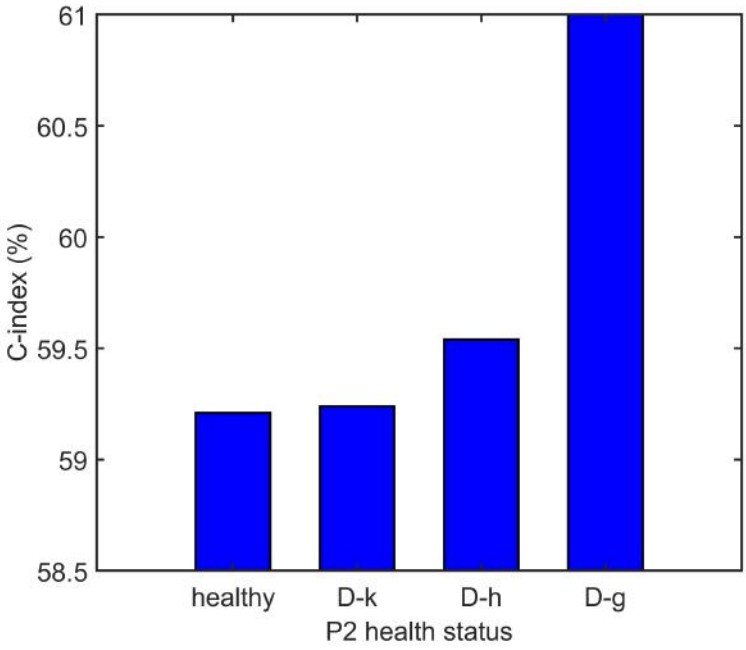

Fig. 5.28 Sensor P2, C-index contribution after each damage impact on the composite plate.

discovering these deviations at the maximum and minimum ranges of the deviation is very high. According to Fig. 5.30 and Fig. 5.24, the damage impact site 'g' demonstrates a higher

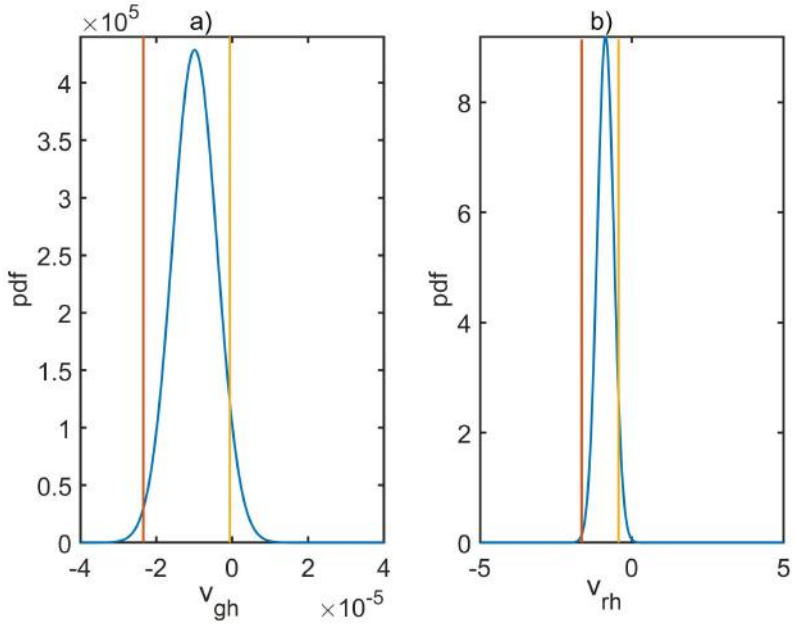

Fig. 5.29 The pdf distribution of the a) v_{gh} and b) v_{rh} variables for the P2 repeated measurements in a healthy state.

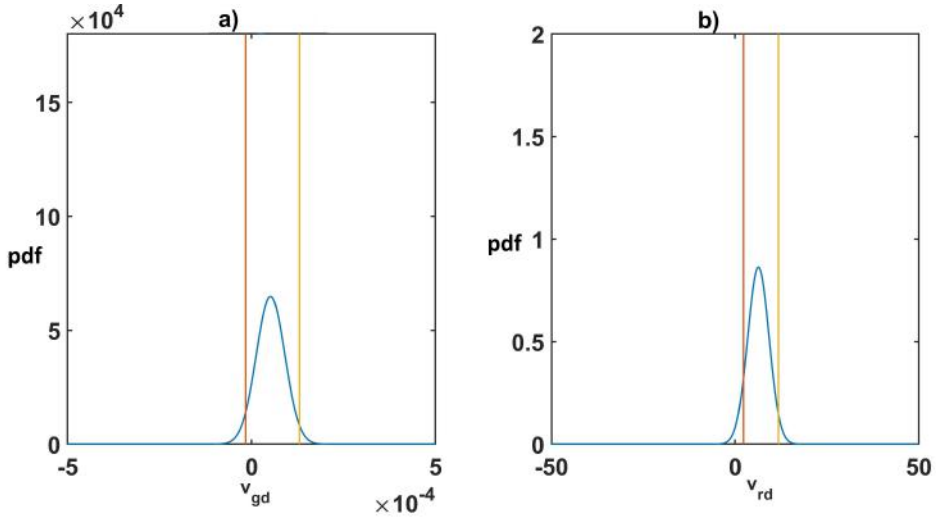

Fig. 5.30 The pdf distribution of the a) v_{gd} and b) v_{rd} variables for P2 following the impact of damage "h".

deviation than impact place ’h’ out of A and B limits. Due to the comparable nature of the G and R spectra in Fig. 5.29 and Fig. 5.31, pdf for the position "k" is essentially identical to repeated healthy state measurements.

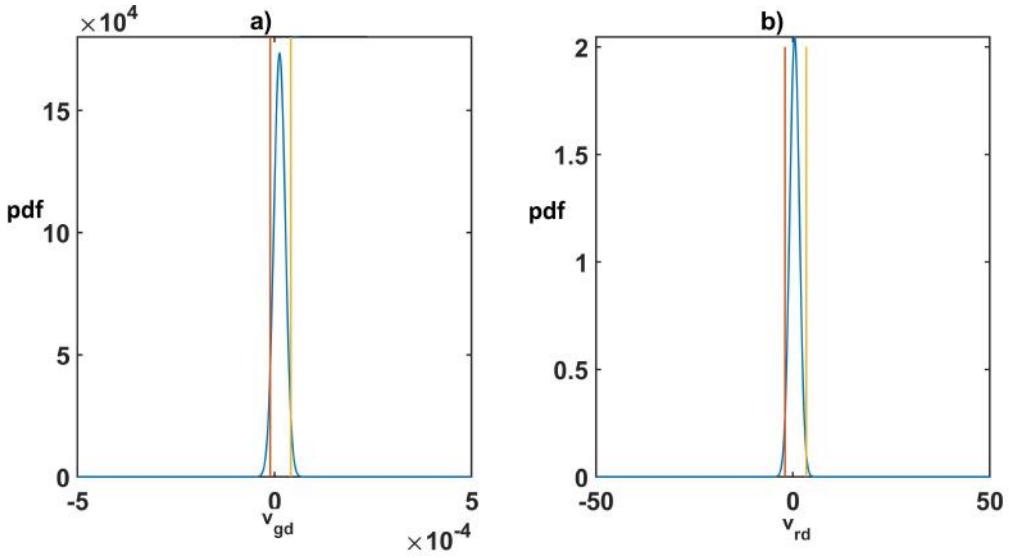

Fig. 5.31 The pdf distribution of the a) v_{gd} and b) v_{rd} for P2 following the impact of damage "k".

Chapter 6

Conclusions and Future work

The thesis summarizes the data-driven approach to improve the performance of damage detection and classification. The unified approach considers many factors like data fusion of EMI variables and sensor data fusion for the sensor network. Further, a novel standard deviation-based approach is discussed for the frequency range selection. Multi-damage detection and an inverse model were proposed. The major contribution with recommended future works is described in this chapter.

6.1 Research conclusions

Firstly, thesis successfully demonstrates the advantage of the parallel combination of the EMI-based damage detection. This methodology enhanced the scope of study from individual connections of the actuators to fused connections based damage detection to reduce the time taken during the measurement. This work investigate damage sensitivity of mass and crack for measurement time consumption reduction using the proposed connection. This method shows sensitivity for mass detection in varied temperature conditions. However, it should noted that the individual connections are more sensitive to the environment conditions mass was within the sensitivity range of both transducers. All connections p1, p2, p12p, and p12s detected the big mass (50 gram) in the both locations. The p12p successfully detected the small mass in the varying temperature condition irrespective of the healthy baseline measurement temperature. The p12p connections has also been detected the small crack created in the steel beam. This paper successfully demonstrates the advantage of the parallel combination of the EMI-based damage detection using RMSD and MAPD and have less influence of the temperature variation on measurements. Finally, this approach allows us time consumption reduction using the proposed connection for mass detection in varied

temperature conditions. The following advantage, parallel connections hold in compared to the individual connections.

1. Faster measurement.
2. Less sensitivity to the temperature variation in compared to the other individual and combined connections and always able to detect the damage.
3. Robust damage detection sensitivity for the small and big simulated mass as well crack in the steel beam.

The improvement of SHM performance in low weight structures was the main emphasis of the thesis. The performance of damage detection and damage severity assessment can be improved using a data-driven strategy based on the combination of the G and R parameters data fusion derived from the EMI measurements. The most common damage indices used to identify anomalies in a structure using the EMI approach are the RMSD, RMSDk, and MAPD indices. These indices, developed using F, are more precise in identifying the degree of damage. For two different structures, specifically a GFRP beam with introduced delamination and a GFRP plate with introduced impact damage, the performance of the parameter fused F is compared with that of R and G. The research was conducted using a frequency range of 1 kHz to 100 kHz to make structural sample comparisons. The outcomes show that the fused F parameter is, in fact, more reliable for categorizing the degree of damage. It can be seen that the sensitivity is increased by combining the G and R factors. This might be accounted by the smoother F spectrum that was produced by multiplying the G and R spectra. Furthermore, compared to present approaches, which concentrate on a narrow frequency range where the selected parameter (G or R) is more sensitive, the F spectra can identify damage over a wide frequency range. The F parameter's wider frequency range for sensitivity makes application simpler.

Further, regardless of whether a wide or small frequency range is chosen, a robust identification method based on integrated data fusion is presented for estimating structural damage, and the chosen frequency contains the resonant frequency range based on a process of trial and error. The identification of many damages at various locations in a wide frequency range was effectively accomplished in this work by applying data fusion at the sensor level by a common baseline model of sensor network. The suggested solution demonstrates an integrated strategy employing PCA and SOM as a more reliable way for damage localisation. The SOM was employed for the variable level data fusion in the EMI technique employing the four sensor data |Z|, |Y|, R and G. The robust method incorporates data fusion-based SOM classification for SHM, statistical PCA tools-based damage classification, and PCA-based

RMSD index. In the choice to identify damage, the PCA concatenates the data fusion technique based on variance contribution and machine learning SOM. The Q-statistics (Q index) and Hotelling's T^2 statistic are used in the SOM investigations to classify the damage. Irrespective to the trial-and-error based damage detection strategy, the method exhibits robust damage sensitivity to the specified resonance frequency 180-250 kHz and large frequency range (17-600 kHz) that contains the resonant frequency range. The following conclusion was reached utilizing sensor network-based damage detection and the combination of sensor-level and variable-level data.

- The comparison of the PCA-based RMSD index and the conventional RMSD technique for damage identification. In comparison to the conventional RMSD approach, the PCA-based data fusion shows the potential for damage identification.
- The methodology developed in this work are successfully tested and validated by drilling a hole that is 5 mm in diameter, increasing it to 8 mm, and eventually to 10 mm. The fusion of variables |Z| and R provides superior data quality than variables |Y| and G, supporting the calculation of the fusion-based DI index.
- The use of data variables |Z|, |Y|, R and G in EMI approach increases potential through the application of data fusion. Over the Q index of the fused variables, the SOM of the T^2 index has demonstrated superior performance.

The performance assessment is not limited to damage severity but also proposed data fusion for the sensor network based damage imaging. The study made a comparison to a strategy put forward by Zhu et al. [13], which was regarded as pioneering for the localisation of damage using linear weight of DI utilizing the EMI methodology. The comparative discussion aims to emphasize a modified probability weight function-based damage imaging strategy for large sensing radius steps/intervals. In comparison to small 'r' intervals, the approach has explored the behavior of big steps in 'r' values on damage imaging. Because large intervals require less computation and processing, they take less time. The relative efficacy of DCMI, F data, and modified normalized data (ND) has also been investigated using big interval. The DCMI technique has the biggest Euclidian distance between the true location of damage and expected damage, making it less suitable for the large interval steps of the sensing radius region. The nascent method of fused data F variables and ND has effectively demonstrated the best effectiveness on GFRP composite plate with impact damage. The proposed approach extended to detect and localize the two and three damages T1, T2, and T1, T2, T3 simultaneously in the 3D printed ABS structure. Further, a new technique based on inverse formulation for damage localization using EMI impedance signature has

been proposed. An analytical model is first established to determine the dependence of the DI on the distance and angle. The analytical model is then used to compute the DI of all the sensors under difference damage scenarios and used as a database for damage localization. The experimental EMI signature obtained from the host structure is used to calculate the DIs. These DIs are compared to the DI generated from the analytical model. A value of higher relative error is eliminated by observing model and measurement errors. The proposed method is applied to the analytical models using the combination of exponential and cosine fit which yields better damage localization due to the lower modelling errors. The method is applied for real impact damage scenario and the proposed method works really well for simulated and real damage scenarios.

Lastly, the study extends the data fusion based on a standard deviation-based frequency range selection approach. The Gaussian probability density function of two-variable used in data fusion-based damage detection in the EMI technique. This maximizes the known likelihood distribution for the given G and R experimental data. The likelihood function relates the extent to which the G and R EMI variable probability is subject to change by utilizing the available information about the problem. A novel Gaussian integral equation was used to find the C-index for the G and R together in quantifying the location and severity of damages. The work calculates the C-index, a robust damage identification statistical fusion tool in damage classification of EMI-based structural health monitoring. This C-index equation provides higher accuracy for the fusion of two variables with a reasonable estimate for the two variables G and R. The novel approach using maximum likelihood covered area under healthy and damage state curve for the selected frequency range and showed improvement for damage detection capability in comparison to the traditional RMSD approach. This work demonstrates the theoretically effective frequency range selection for damage detection. The methodology studied many kinds of structures (small and big aluminum plates with drilled holes, and composite plates with different types of damage) with damages. In the first case, the aluminum plate with drilled hole, the second case the composite plate with added mass. The third case of different damage severity and the fourth case of impact damages moving toward P2 were successfully detected. The method has an advantage over the other approach because it only covers the area enclosed between the damaged and healthy state in the selected frequency band and fuses two variables G and R simultaneously. This approach successfully compared the standard RMSD approach with the new damage index for damage detection evaluation. The discussed results show sensitivity towards the theoretical model for a considerable amount of experimental aluminum and composite GFRP data. The implemented modified algorithm was used for localization of the damage employing the suitable effective frequency range selection based on σ values. The

method shows better sensitivity for the lighter damage case of movement of magnetic mass and enlargement of the hole. However, for the larger hole damage on the aluminum plate method sensitivity increases in the higher frequency ranges. **Hence, it is proved that the thesis provides robust data-driven data-fusion based approaches to enhance damage detection and localization for metal, composites, and 3D printed polymer structures by proving the following:**

- **The data fusion techniques are enhancing performance compared to the conventional approach for damage identification.**
- **Sensor network-based damage localization accurately predicts single and multi-damage locations.**
- **A data-driven theoretical effective frequency range selection is possible that enhances the performance of data fusion-based damage detection and damage severity quantification.**

6.2 Major Contributions

This thesis comprehensively discusses a detailed analysis of EMI data fusion in light structures in order to enhance damage quantification utilizing DI.

The benefit of data fusion-based parallel combination in damage detection is centered on reducing measurement time and an easier robust technique while investigating the damage sensitivity in a constrained temperature fluctuating environment.

In this thesis, the variable fusion level (F signatures) and sensor level (sensor network) data fusion approaches are illustrated, along with a discussion of how they might be used to enhance the performance of damage detection using PCA and SOM.

For the first time, a robust damage identification approach based on integrated data fusion was established, for an EMI application employing the PCA-based Q index and the T^2 index.

Structural multi-damage detection is based on linear damage imaging techniques in a 3D-printed ABS structure. Additionally, a novel method for damage localisation using the EMI impedance signature based on inverse formulation has been put forth.

For the purpose of choosing the most efficient frequency ranges for damage detection, a novel theoretical approach based on standard deviation is employed.

Probabilistic integral based data fusion approach using C-index which covers the area difference of the health of the structures, so it is an effective data-driven approach for damage identification irrespective of the type of damage in the structure.

6.3 Future work recommendation

This thesis comprehensively discusses the application of data-driven data fusion based EMI SHM methods. Based on the experiences and results obtained in this research, the following suggestions can be made for further work.

The sensitivity of the fused, F parameter to complicated geometries-based metallic, composite structure are being investigated. Furthermore, the investigation must analyze environmental elements such as temperature change.

The impact of temperature variation must be highlighted in structural multi-damage identification. Studying the effect of temperature on correctly identifying damage and misinterpretations of damage is necessary. Additionally, the effect has to compensate for precisely detect damage in metal and composite materials.

The inverse technique-based detection and localization of various defects in the structure are indicated as a subject of additional research in the varying temperature conditions. In addition, the issue of the optimal placement of sensors, will also be examined in the future.

EMI can work with the other sensing method, it can offer useful information about the condition of a structure. In order to provide a more complete health assessment of a material, future research may investigate how to combine EMI with other sensing methods, such as ultrasound.

References

[1] S. S. Kessler, Piezoelectric-based in-situ damage detection of composite materials for structural health monitoring systems, Ph.D. thesis, Massachusetts Institute of Technology (2002).

[2] D. Balageas, C.-P. Fritzen, A. Guemes, Structural Health Monitoring - Google Books, 2006.

[3] D. J. Inman, C. R. Farrar, V. Lopes, V. Steffen, Damage Prognosis, John Wiley & Sons, Ltd, Chichester, UK, 2005. doi:10.1002/0470869097.

[4] M. D. Dc, National Transportation Safety Board Aircraft Accident Report, Ntsb (1990) 129.

[5] M. Mousavi, A. H. Gandomi, Deep learning for structural health monitoring under environmental and operational variations, in: Nondestructive Characterization and Monitoring of Advanced Materials, Aerospace, Civil Infrastructure, and Transportation XV, Vol. 11592, SPIE, 2021, pp. 100–107.

[6] H. Cui, B. Li, L. B. Zhou, W. Liu, Damage detection in thick plate structures based on ultrasonic sh wave, Smart Materials and Structures 31 (9) (2022) 095018.

[7] P. Packo, P. Kijanka, M. J. Leamy, Spectral analysis of guided wave propagation in discretized domains under local interactions, Proceedings of the Institution of Mechanical Engineers, Part C: Journal of Mechanical Engineering Science 234 (3) (2020) 746–769.

[8] X. Fan, Electromechanical Impedance-based Techniques for Structural Health Monitoring (June) (2018).

[9] P. Kołakowski, Structural health monitoring–a review with the emphasis on low-frequency methods, Engineering Transactions 55 (3) (2007) 239–275.

[10] M. Heesch, M. Dziendzikowski, K. Mendrok, Z. Dworakowski, Diagnostic-quality guided wave signals synthesized using generative adversarial neural networks, Sensors 22 (10) (2022) 3848.

[11] M. Mitra, S. Gopalakrishnan, Guided wave based structural health monitoring: A review, Smart Materials and Structures 25 (5) (2016) 053001.

[12] R. Lu, Y. Shen, B. Zhang, W. Xu, Nonlinear electro-mechanical impedance spectroscopy for fatigue crack monitoring, Mechanical Systems and Signal Processing 184 (2023) 109749.

[13] M. A. Fakih, S. Mustapha, J. Tarraf, G. Ayoub, R. Hamade, Detection and assessment of flaws in friction stir welded joints using ultrasonic guided waves: experimental and finite element analysis, Mechanical Systems and Signal Processing 101 (2018) 516–534.

[14] S. Mustapha, L. Ye, D. Wang, Y. Lu, Debonding detection in composite sandwich structures based on guided waves, AIAA journal 50 (8) (2012) 1697–1706.

[15] A. Alippi, M. Germano, A. Bettucci, F. Farrelly, G. Muzio, Traversal time of acoustic plate waves through a tunneling section, Physical Review E 57 (5) (1998) R4907.

[16] C. Kralovec, M. Schagerl, Review of structural health monitoring methods regarding a multi-sensor approach for damage assessment of metal and composite structures, Sensors 20 (3) (2020) 826.

[17] H. Hoshyarmanesh, M. Ghodsi, M. Kim, H. H. Cho, H.-H. Park, Temperature effects on electromechanical response of deposited piezoelectric sensors used in structural health monitoring of aerospace structures, Sensors 19 (12) (2019) 2805.

[18] V. B. Sharma, K. Singh, R. Gupta, A. Joshi, R. Dubey, V. Gupta, S. Bharadwaj, M. I. Zafar, S. Bajpai, M. A. Khan, et al., Review of structural health monitoring techniques in pipeline and wind turbine industries, Applied System Innovation 4 (3) (2021) 59.

[19] J. A. Mehr, E. J. Alvarez, A. Ning, Unsteady aerodynamic analysis of wind harvesting aircraft, in: AIAA Aviation 2020 Forum, 2020, p. 2761.

[20] M. A. Saadeghvaziri, R. Hadidi, Cause and control of transverse cracking in concrete bridge decks (2002).

[21] C. Soh, Y. Yang, S. Bhalla, Smart Materials in Structural Health Monitoring, Control and Biomechanics - Google Kitaplar, 2012.

[22] C. Liang, F. P. Sun, C. A. Rogers, Coupled electro-mechanical analysis of adaptive material systems - determination of the actuator power consumption and system energy transfer, Journal of Intelligent Material Systems and Structures 8 (4) (1997) 335–343. doi:10.1177/1045389X9700800406.

[23] L. Zhou, S.-X. Chen, Y.-Q. Ni, al, M. Marchi, F. Guimarães Baptista, P. Roberto de Aguiar, C. Liang, F. Sun, C. A. Rogers, Electro-mechanical impedance modeling of active material systems, Smart Materials and Structures 5 (2) (1996) 171. doi:10.1088/0964-1726/5/2/006.

[24] S. Zhou, C. Liang, C. A. Rogers, Integration and Design of Piezoceramic Elements in Intelligent Structures:, Journal of Intelligent Material Systems and Structures 8 (4) (2016) 363–373. doi:10.1177/1045389X9700800409.

[25] V. Giurgiutiu, A. N. Zagrai, Characterization of Piezoelectric Wafer Active Sensors:, Journal of Intelligent Material Systems and Structures 11 (12) (2016) 959–976. doi:10.1106/A1HU-23JD-M5AU-ENGW.

[26] S. Bhalla, C. K. Soh, Structural health monitoring by piezo-impedance transducers. i: Modeling, Journal of Aerospace Engineering 17 (4) (2004) 154–165.

[27] S. Bhalla, C. K. Soh, Structural Health Monitoring by Piezo–Impedance Transducers. II: Applications, Journal of Aerospace Engineering 17 (4) (2004) 166–175. doi:10.1061/(asce)0893-1321(2004)17:4(166).

[28] V. G. M. Annamdas, C. K. Soh, Three-Dimensional Electromechanical Impedance Model. I: Formulation of Directional Sum Impedance, Journal of Aerospace Engineering 20 (1) (2007) 53–62. doi:10.1061/(asce)0893-1321(2007)20:1(53).

[29] J. Zhu, X. Qing, X. Liu, Y. Wang, Electromechanical impedance-based damage localization with novel signatures extraction methodology and modified probability-weighted algorithm, Mechanical Systems and Signal Processing 146 (2021) 107001. doi:10.1016/J.YMSSP.2020.107001.

[30] J. Gadomski, P. Pyrzanowski, Experimental investigation of fatigue destruction of cfrp using the electrical resistance change method, Measurement 87 (2016) 236–245.

[31] J. A. Fairweather, K. C. Craig, Incorporating finite element techniques to simplify the impedance modeling of active structures, Smart Structures and Materials 1998: Mathematics and Control in Smart Structures 3323 (1998) 602–613. doi:10.1117/12.316339.

[32] A. S. Naidu, C. K. Soh, K. V. Pagalthivarthi, Bayesian Network for E/M Impedance-Based Damage Identification, Journal of Computing in Civil Engineering 20 (4) (2006) 227–236. doi:10.1061/(ASCE)0887-3801(2006)20:4(227).

[33] A. S. Naidu, C. K. Soh, Identifying damage location with admittance signatures of smart piezo-transducers, Journal of Intelligent Material Systems and Structures 15 (8) (2004) 627–642. doi:10.1177/1045389X04043269.

[34] Y. Xia, H. Hao, J. M. Brownjohn, P. Q. Xia, Damage identification of structures with uncertain frequency and mode shape data, Earthquake Engineering & Structural Dynamics 31 (5) (2002) 1053–1066. doi:10.1002/EQE.137.

[35] Y. Yang, J. Xu, C. K. Soh, Generic Impedance-Based Model for Structure-Piezoceramic Interacting System, Journal of Aerospace Engineering 18 (2) (2005) 93–101. doi:10.1061/(ASCE)0893-1321(2005)18:2(93).

[36] J. Xu, Parameter identification and damage detection using evolutionary programming, Ph.D. thesis, Nanyang Technological University (2005).

[37] Y. Yang, Y. Y. Lim, C. K. Soh, Practical issues related to the application of the electromechanical impedance technique in the structural health monitoring of civil structures: I. Experiment, Smart Materials and Structures 17 (3) (2008) 035008. doi:10.1088/0964-1726/17/3/035008.

[38] Y. Zhang, F. Xu, J. Chen, C. Wu, D. Wen, Electromechanical Impedance Response of a Cracked Timoshenko Beam, Sensors 11 (7) (2011) 7285–7301. doi:10.3390/S110707285.

[39] Y. Y. Lim, C. K. Soh, Towards more accurate numerical modeling of impedance based high frequency harmonic vibration, Smart Materials and Structures 23 (3) (2014) 035017. doi:10.1088/0964-1726/23/3/035017.

[40] Y. Y. Lim, W. Y. H. Liew, C. K. Soh, A Parametric Study on Admittance Signatures of a PZT Transducer Under Free Vibration, Mechanics of Advanced Materials and Structures, 22 (11) (2015) 877–884. doi:10.1080/15376494.2013.864437.

[41] Q. Shuai, K. Zhou, S. Zhou, J. Tang, Fault identification using piezoelectric impedance measurement and model-based intelligent inference with pre-screening, Smart Materials and Structures 26 (4) (2017) 045007. doi:10.1088/1361-665X/AA5D41.

[42] A. A. Ezzat, J. Tang, Y. Ding, A model-based calibration approach for structural fault diagnosis using piezoelectric impedance measurements and a finite element model:, Structural Health Monitoring 19 (6) (2020) 1839–1855. doi:10.1177/1475921719901168.

[43] D. Ai, H. Zhu, H. Luo, C. Wang, Mechanical impedance based embedded piezoelectric transducer for reinforced concrete structural impact damage detection: A comparative study, Construction and Building Materials 165 (2018) 472–483. doi:10.1016/J.CONBUILDMAT.2018.01.039.

[44] J. Zhu, Y. Wang, X. Qing, Modified electromechanical impedance-based disbond monitoring for honeycomb sandwich composite structure, Composite Structures 217 (2019) 175–185. doi:10.1016/J.COMPSTRUCT.2019.03.033.

[45] M. I. Albakri, P. A. Tarazaga, Electromechanical impedance–based damage characterization using spectral element method:, Journal of Intelligent Material Systems and Structures 28 (1) (2016) 63–77. doi:10.1177/1045389X16642534.

[46] J. Esteban, Modeling of the sensing region of a piezoelectric actuator/sensor, Ph.D. thesis (1996).

[47] S. Ritdumrongkul, M. Abe, Y. Fujino, T. Miyashita, Quantitative health monitoring of bolted joints using a piezoceramic actuator–sensor, Smart Materials and Structures 13 (1) (2003) 20. doi:10.1088/0964-1726/13/1/003.

[48] P. Fiborek, P. H. Malinowski, P. Kudela, T. Wandowski, W. M. Ostachowicz, Time-domain spectral element method for modelling of the electromechanical impedance of disbonded composites, Journal of Intelligent Material Systems and Structures 29 (16) (2018) 3214–3221.

[49] R. T. Wu, M. R. Jahanshahi, Data fusion approaches for structural health monitoring and system identification: Past, present, and future:, Structural health monitoring 19 (2) (2018) 552–586. doi:10.1177/1475921718798769.

[50] Y. Zhang, F. Xu, J. Chen, C. Wu, D. Wen, Electromechanical impedance response of a cracked timoshenko beam, Sensors 11 (7) (2011) 7285–7301. doi:10.3390/s110707285.
URL https://www.mdpi.com/1424-8220/11/7/7285

[51] V. G. M. Annamdas, C. K. Soh, Application of electromechanical impedance technique for engineering structures: Review and future issues (nov 2010). doi:10.1177/1045389X09352816.

[52] T. C. Huynh, N. L. Dang, J. T. Kim, Advances and challenges in impedance-based structural health monitoring, Structural Monitoring and Maintenance 4 (4) (2017) 301–329. doi:10.12989/smm.2017.4.4.301.

[53] V. Giurgiutiu, C. A. Rogers, <title>Recent advancements in the electromechanical (E/M) impedance method for structural health monitoring and NDE</title>, in: Smart Structures and Materials 1998: Smart Structures and Integrated Systems, Vol. 3329, 1998, pp. 536–547. doi:10.1117/12.316923.

[54] S. Na, H. K. Lee, Resonant frequency range utilized electro-mechanical impedance method for damage detection performance enhancement on composite structures, Composite Structures 94 (8) (2012) 2383–2389. doi:10.1016/j.compstruct.2012.02.022.

[55] X. Fan, J. Li, H. Hao, Review of piezoelectric impedance based structural health monitoring: Physics-based and data-driven methods:, Advances in Structural Engineering 24 (16) (2021) 3609–3626. doi:10.1177/13694332211038444.

[56] K. K. Tseng, A. S. Naidu, Non-parametric damage detection and characterization using smart piezoceramic material, Smart Materials and Structures 11 (3) (2002) 317.

[57] D. de Souza Rabelo, J. D. Hobeck, D. J. Inman, R. M. Finzi Neto, V. Steffen, Real-time structural health monitoring of fatigue crack on aluminum beam using an impedance-based portable device:, Journal of Intelligent Material Systems and Structures (20) 3152–3162. doi:10.1177/1045389X17705213.

[58] P. Liu, W. Wang, Y. Chen, X. Feng, L. Miao, Concrete damage diagnosis using electromechanical impedance technique, Construction and Building Materials 136 (2017) 450–455. doi:10.1016/j.conbuildmat.2016.12.173.

[59] M. Rosiek, A. Martowicz, T. Uhl, Electromechanical impedance based shm system for aviation applications, in: Key Engineering Materials, Vol. 518, Trans Tech Publ, 2012, pp. 127–136.

[60] A. Martowicz, A. Sendecki, M. Salamon, M. Rosiek, T. Uhl, Application of electromechanical impedance-based shm for damage detection in bolted pipeline connection, Nondestructive Testing and Evaluation 31 (1) (2016) 17–44.

[61] O. Cherrier, P. Selva, V. Pommier-Budinger, F. Lachaud, J. Morlier, Damage localization map using electromechanical impedance spectrums and inverse distance weighting interpolation: Experimental validation on thin composite structures:, Structural Health Monitoring 12 (4) (2013) 311–324. doi:10.1177/1475921713493343.

[62] W. S. Na, J. Baek, A Review of the Piezoelectric Electromechanical Impedance Based Structural Health Monitoring Technique for Engineering Structures, Sensors 18 (5) (2018) 1307. doi:10.3390/S18051307.

[63] X. Wang, J. Tang, Damage identification using piezoelectric impedance approach and spectral element method, Journal of Intelligent Material Systems and Structures 20 (8) (2009) 907–921. doi:10.1177/1045389X08099659.

[64] X. Fan, J. Li, H. Hao, Piezoelectric impedance based damage detection in truss bridges based on time frequency ARMA model, Smart Structures and Systems 18 (3) (2016) 501–523. doi:10.12989/sss.2016.18.3.501.

[65] X. Fan, J. Li, H. Hao, S. Ma, Identification of Minor Structural Damage Based on Electromechanical Impedance Sensitivity and Sparse Regularization, Journal of Aerospace Engineering 31 (5) (2018) 04018061. doi:10.1061/(ASCE)AS.1943-5525.0000892.

[66] T. Wandowski, S. Opoka, P. Malinowski, W. Ostachowicz, The performance of three electromechanical impedance damage indicators on structural element with bolted joints, in: Proc. of NDT in Aerospace symposium, The e-Journal of Nondestructive Testing, Vol. 20, 2015.

[67] P. Selva, O. Cherrier, V. Budinger, F. Lachaud, J. Morlier, Smart monitoring of aeronautical composites plates based on electromechanical impedance measurements and artificial neural networks, Engineering Structures 56 (2013) 794–804. doi:10.1016/J.ENGSTRUCT.2013.05.025.

[68] P. Nazarko, L. Ziemiański, Application of artificial neural networks in the damage identification of structural elements, Computer Assisted Methods in Engineering and Science 18 (3) (2017) 175–189.

[69] H. Fekrmandi, M. Unal, S. Rojas Neva, I. N. Tansel, D. McDaniel, A novel approach for classification of loads on plate structures using artificial neural networks, Measurement 82 (2016) 37–45. doi:10.1016/J.MEASUREMENT.2015.12.027.

[70] S. Na, H. K. Lee, Neural network approach for damaged area location prediction of a composite plate using electromechanical impedance technique, Composites Science and Technology 88 (2013) 62–68. doi:10.1016/J.COMPSCITECH.2013.08.019.

[71] M. A. de Oliveira, D. J. Inman, Performance analysis of simplified Fuzzy ARTMAP and Probabilistic Neural Networks for identifying structural damage growth, Applied Soft Computing 52 (2017) 53–63. doi:10.1016/J.ASOC.2016.12.020.

[72] M. Djemana, M. Hrairi, Y. Al Jeroudi, Using Electromechanical Impedance and Extreme Learning Machine to Detect and Locate Damage in Structures, Journal of Nondestructive Evaluation 36 (2) (2017) 1–10. doi:10.1007/S10921-017-0417-5/FIGURES/7.

[73] U. Meher, S. K. Mishra, M. R. Sunny, Impedance-based looseness detection of bolted joints using artificial neural network: An experimental study, Structural Control and Health Monitoring 29 (10) (2022) e3049.

[74] S. Park, J. J. Lee, C. B. Yun, D. J. Inman, Electro-Mechanical Impedance-Based Wireless Structural Health Monitoring using PCA-Data Compression and k-means Clustering Algorithms:, Journal of intelligent material systems and structures 19 (4) (2007) 509–520. doi:10.1177/1045389X07077400.

[75] S. J. Qin, Statistical process monitoring: basics and beyond, Journal of Chemometrics 17 (8-9) (2003) 480–502. doi:10.1002/CEM.800.

[76] L. E. Mujica, J. Rodellar, A. Fernández, A. Güemes, Q-statistic and T2-statistic PCA-based measures for damage assessment in structures:, Structural Health Monitoring 10 (5) (2010) 539–553. doi:10.1177/1475921710388972.

[77] M. A. de Oliveira, A. V. Monteiro, J. V. Filho, A New Structural Health Monitoring Strategy Based on PZT Sensors and Convolutional Neural Network, Sensors 18 (9) (2018) 2955. doi:10.3390/S18092955.

[78] S. W. F. de Rezende, J. d. R. V. de Moura, R. M. F. Neto, C. A. Gallo, V. Steffen, Convolutional neural network and impedance-based shm applied to damage detection, Engineering Research Express 2 (3) (2020) 035031.

[79] O. Alazzawi, D. Wang, Deep convolution neural network for damage identifications based on time-domain pzt impedance technique, Journal of Mechanical Science and Technology 35 (5) (2021) 1809–1819.

[80] L. Zhou, S. X. Chen, Y. Q. Ni, A. W. H. Choy, EMI-GCN: a hybrid model for real-time monitoring of multiple bolt looseness using electromechanical impedance and graph convolutional networks, Smart Materials and Structures 30 (3) (2021) 035032. doi:10.1088/1361-665X/ABE292.

[81] R. Perera, L. Torres, A. Ruiz, C. Barris, M. Baena, An EMI-Based Clustering for Structural Health Monitoring of NSM FRP Strengthening Systems, Sensors 19 (17) (2019) 3775. doi:10.3390/S19173775.

[82] P. O. Junior, S. Conte, D. M. D'Addona, P. Aguiar, F. Bapstista, An improved impedance-based damage classification using Self-Organizing Maps, Procedia CIRP 88 (2020) 330–334. doi:10.1016/J.PROCIR.2020.05.057.

[83] E. Sevillano, R. Sun, A. Gil, R. Perera, Interfacial crack-induced debonding identification in FRP-strengthened RC beams from PZT signatures using hierarchical clustering analysis, Composites Part B: Engineering 87 (2016) 322–335. doi:10.1016/J.COMPOSITESB.2015.09.006.

[84] L. V. Palomino, V. Steffen, R. M. Finzi, Fuzzy cluster analysis methods applied to impedance based structural health monitoring for damage classification, Conference Proceedings of the Society for Experimental Mechanics Series 6 (2012) 205–212. doi:10.1007/978-1-4614-2419-2_18/FIGURES/8.

[85] S. Ručevskis, T. Rogala, A. Katunin, Monitoring of damage in composite structures using an optimized sensor network: A data-driven experimental approach, Sensors 23 (4) (2023) 2290.

[86] C. Zuo, X. Feng, Y. Zhang, L. Lu, J. Zhou, Crack detection in pipelines using multiple electromechanical impedance sensors, Smart Materials and Structures 26 (10) (2017) 104004. doi:10.1088/1361-665X/AA7EF3.

[87] J. Hou, Z. Li, Q. Zhang, Ł. Jankowski, H. Zhang, Local mass addition and data fusion for structural damage identification using approximate models, International Journal of Structural Stability and Dynamics 20 (11) (2020) 2050124.

[88] X. Zhao, M. Li, G. Song, J. Xu, Hierarchical ensemble-based data fusion for structural health monitoring, Smart Materials and Structures 19 (4) (2010) 045009. doi:10.1088/0964-1726/19/4/045009.

[89] J. J. Rodríguez, L. I. Kuncheva, C. J. Alonso, Rotation forest: A New classifier ensemble method, IEEE Transactions on Pattern Analysis and Machine Intelligence 28 (10) (2006) 1619–1630. doi:10.1109/TPAMI.2006.211.

[90] F.-C. Chen, M. R. Jahanshahi, Nb-cnn: Deep learning-based crack detection using convolutional neural network and naïve bayes data fusion, IEEE Transactions on Industrial Electronics 65 (5) (2017) 4392–4400.

[91] F. G. Baptista, J. V. Filho, Optimal frequency range selection for PZT transducers in impedance-based SHM systems, IEEE Sensors Journal 10 (8) (2010) 1297–1303. doi:10.1109/JSEN.2010.2044037.

[92] D. M. Peairs, P. A. Tarazaga, D. J. Inman, Frequency Range Selection for Impedance-Based Structural Health Monitoring, Journal of Vibration and Acoustics 129 (6) (2007) 701–709. doi:10.1115/1.2775506.

[93] S. Adhikari, S. Bhalla, Modified Dual Piezo Configuration for Improved Structural Health Monitoring Using Electro-Mechanical Impedance (EMI) Technique, Experimental Techniques 43 (1) (2019) 25–40. doi:10.1007/S40799-018-0249-Y/FIGURES/17.

[94] D. Chen, L. Huo, G. Song, Emi based multi-bolt looseness detection using series/parallel multi-sensing technique, Smart Struct. Syst 25 (2020) 423–432.

[95] B. Kalyanasundaram, J. S. Thiyagarajan, Piezoelectric sensor-based damage progression in concrete through serial/ parallel multi-sensing technique Magneto-Rheological Elastomer based Smart Seismic and Vibration Isolators View project PZT based smart sensing View projectdoi:10.1177/1475921719845153.

[96] C. Bharathi Priya, T. Jothi Saravanan, K. Balamonica, N. Gopalakrishnan, A. R. M. Rao, EMI based monitoring of early-age characteristics of concrete and comparison of serial/parallel multi-sensing technique, Construction and Building Materials 191 (2018) 1268–1284. doi:10.1016/J.CONBUILDMAT.2018.10.079.

[97] K. Krishnamurthy, F. Lalande, C. A. Rogers, Effects of temperature on the electrical impedance of piezoelectric sensors, in: I. Chopra (Ed.), Proceedings of SPIE - The International Society for Optical Engineering, Vol. 2717, SPIE, 1996, pp. 302–310. doi:10.1117/12.239033.

[98] G. Park, K. Kabeya, H. H. Cudney, D. J. Inman, Impedance-Based Structural Health Monitoring for Temperature Varying Applications, JSME International Journal Series A Solid Mechanics and Material Engineering 42 (2) (1999) 249–258. doi:10.1299/JSMEA.42.249.

[99] T. Wandowski, P. H. Malinowski, W. M. Ostachowicz, Temperature and damage influence on electromechanical impedance method used for carbon fibre–reinforced polymer panels:, Journal of Intelligent Material Systems and Structures 28 (6) (2016) 782–798. doi:10.1177/1045389X16657423.

[100] F. P. Sun, Z. A. Chaudhry, C. A. Rogers, M. Majmundar, C. Liang, Automated real-time structure health monitoring via signature pattern recognition, https://doi.org/10.1117/12.208261 2443 (1995) 236–247. doi:10.1117/12.208261.

[101] J. Kim, B. L. Grisso, J. K. Kim, D. S. Ha, D. J. Inman, Electrical modeling of piezoelectric ceramics for analysis and evaluation of sensory systems, in: 2008 IEEE Sensors Applications Symposium, IEEE, 2008, pp. 122–127.

[102] K. S. Van Dyke, The piezo-electric resonator and its equivalent network, Proceedings of the Institute of Radio Engineers 16 (6) (1928) 742–764.

[103] W. H. Press, S. A. Teukolsky, Savitzky-Golay Smoothing Filters, Citation: Computers in Physics 4 (1990) 669. doi:10.1063/1.4822961.

[104] L. Skarbek, T. Wandowski, S. Opoka, P. Malinowski, W. Ostachowicz, Electromechanical impedance technique and scanning vibrometry for structure characterization, in: Proceedings of the 6th European Workshop - Structural Health Monitoring 2012, EWSHM 2012, Vol. 1, 2012, pp. 179–185.

[105] B. V. Dasarathy, Sensor fusion potential exploitation-innovative architectures and illustrative applications, Proceedings of the IEEE 85 (1) (1997) 24–38. doi:10.1109/5.554206.

[106] R. C. Luo, C. C. Yih, K. L. Su, Multisensor fusion and integration: Approaches, applications, and future research directions, IEEE Sensors Journal 2 (2) (2002) 107–119. doi:10.1109/JSEN.2002.1000251.

[107] F. Castanedo, A review of data fusion techniques, The Scientific World Journal 2013 (2013). doi:10.1155/2013/704504.

[108] V. G. M. Annamdas, C. K. Soh, Load monitoring using a calibrated piezo diaphragm based impedance strain sensor and wireless sensor network in real time, Smart Materials and Structures 26 (4) (2017) 045036. doi:10.1088/1361-665X/aa5f40.

[109] R. Perera, A. Pérez, M. García-Diéguez, J. L. Zapico-Valle, Active wireless system for structural health monitoring applications, Sensors 17 (12) (2017) 2880. doi:10.3390/s17122880.

[110] F. G. Baptista, D. E. Budoya, V. A. de Almeida, J. A. C. Ulson, An Experimental Study on the Effect of Temperature on Piezoelectric Sensors for Impedance-Based Structural Health Monitoring, Sensors 14 (1) (2014) 1208–1227. doi:10.3390/S140101208.

[111] S. Na, H. K. Lee, Resonant frequency range utilized electro-mechanical impedance method for damage detection performance enhancement on composite structures, Composite Structures 94 (8) (2012) 2383–2389. doi:10.1016/J.COMPSTRUCT.2012.02.022.

[112] I. T. Jolliffe, PRINCIPAL COMPONENT ANALYSIS: A BEGINNER'S GUIDE I. Introduction and application (1990). doi:10.1002/j.1477-8696.1990.tb05558.x.

[113] T. Kohonen, Others, MATLAB implementations and applications of the self-organizing map, Unigrafia Oy, Helsinki, Finland 2 (2014).

[114] P. Stefanovič, O. Kurasova, Visual analysis of self-organizing maps, Nonlinear analysis : modelling and control 16 (4) (2011) 488–504. doi:10.15388/NA.16.4.14091.

[115] J. Vesanto, J. Himberg, E. Alhoniemi, J. Parhankangas, SOM Toolbox for Matlab 5 Libella Oy Espoo 2000 SOM Toolbox for Matlab 5 (2000).

[116] Z. Wu, K. Liu, Y. Wang, Y. Zheng, Validation and evaluation of damage identification using probability-based diagnostic imaging on a stiffened composite panel:, Journal of Intelligent Material Systems and Structures 26 (16) (2014) 2181–2195. doi:10.1177/1045389X14549873.

[117] J. Zhu, X. Qing, X. Liu, Y. Wang, Electromechanical impedance-based damage localization with novel signatures extraction methodology and modified probability-weighted algorithm, Mechanical Systems and Signal Processing 146 (jan 2020). doi:10.1016/J.YMSSP.2020.107001.

[118] C. Kralovec, M. Schagerl, M. Mayr, Localization of damages by model-based evaluation of electro-mechanical impedance measurements.

[119] R. Soman, S. K. Singh, T. Wandowski, P. Malinowski, Development of robust metric based on cumulative electrical power for electromechanical impedance based structural health monitoring, Smart Materials and Structures 29 (11) (2020) 115047.

[120] G. Park, H. Sohn, C. R. Farrar, D. J. Inman, Overview of piezoelectric impedance-based health monitoring and path forward, Shock and Vibration Digest 35 (6) (2003) 451–463. doi:10.1177/05831024030356001.

[121] L. Sienkiewicz, M. Ronkowski, G. Kostro, R. Ryndzionek, J.-F. Rouchon, Identification of the mechanical properties of the skin by electromechanical impedance analysis of resonant piezoelectric actuator, in: IECON 2013-39th Annual Conference of the IEEE Industrial Electronics Society, IEEE, 2013, pp. 3940–3945.

[122] W. S. Na, History data free piezoelectric based non-destructive testing technique for debonding detection of composite structures, Composite Structures 226 (2019) 111225. doi:10.1016/J.COMPSTRUCT.2019.111225.

[123] T. Wandowski, P. H. Malinowski, W. M. Ostachowicz, Delamination detection in CFRP panels using EMI method with temperature compensation, Composite Structures 151 (2016) 99–107. doi:10.1016/J.COMPSTRUCT.2016.02.056.

[124] B. Wang, Y. Sun, Y. Li, C. Zhang, Debonding Damage Detection in CFRP Plate-Strengthened Steel Beam Using Electromechanical Impedance Technique, Sensors 2019, Vol. 19, Page 2296 19 (10) (2019) 2296. doi:10.3390/S19102296.

[125] R. T. Wu, M. R. Jahanshahi, Data fusion approaches for structural health monitoring and system identification: Past, present, and future:, Structural Health Monitoring 19 (2) (2018) 552–586. doi:10.1177/1475921718798769.

[126] X. Gros, Perspectives of NDT data fusion, NDT Data Fusion 180 (1997).

[127] B. Khaleghi, A. Khamis, F. Karray, N. Razavi, S. Multisensor, Data fusion: A review of the state-of-the-art, Informat Fusion (2011).

[128] J. Manyika, H. Durrant-Whyte, Data fusion and sensor management: a decentralized information-theoretic approach, Prentice Hall PTR, 1995.

[129] T. R. Andriamahefa, Integer Occupancy Grids : a probabilistic multi-sensor fusion framework for embedded perception (2018) 1–185.

[130] J. O. Berger, Statistical Decision Theory and Bayesian Analysis - James O. Berger - Google Books, 2013.

[131] R. Soman, P. Kudela, K. Balasubramaniam, S. K. Singh, P. Malinowski, Sensors 2019 19 (8) (apr). doi:10.3390/S19081856.